

Alma Mater Studiorum – Università di Bologna

DOTTORATO DI RICERCA IN

CHIMICA

Ciclo XXXI

**Settore Concorsuale: 03/C2**

**Settore Scientifico Disciplinare: CHIM/04**

**Synthesis gas production by  
combined Steam and Dry Reforming  
of clean biogas**

**Presentata da:** Nicola Schiaroli

**Coordinatore Dottorato**

**Prof. Aldo Roda**

**Supervisore**

**Prof. Angelo Vaccari**

**Co-supervisore**

**Dott. Carlo Lucarelli**

**Esame finale anno 2019**

## **Key words**

Clean biogas

Dry Reforming

Combined Steam/Dry Reforming

Water Gas Shift

Synthesis gas

Hydrogen

Ni, Rh, Cu

## Abstract

Ni-based catalyst promoted with Rh or Cu were prepared from hydrotalcite-like precursors by two different synthesis methods (co-precipitation and via surfactant-assisted-templating route) and employed in Dry Reforming (DR) and combined Steam/Dry Reforming (S/DR) of clean biogas (CB, an equimolar mixture of CH<sub>4</sub> and CO<sub>2</sub>) to produce a synthesis gas suitable for Fischer-Tropsch or methanol synthesis. The catalyst before and after reaction were deeply characterized by porosimetric analyses, XRD, Raman, TG, H<sub>2</sub>-TPR, CO<sub>2</sub>-TPD, TEM and SEM techniques. The DR results showed that the addition of a small amount of Rh increased the CO<sub>2</sub> conversion and significantly decreased the carbon formation. The addition of steam to the reactant feed to perform the combined S/DR reaction promoted the catalyst activity further improving its resistance to carbon deposition. XRD and TPR analyses showed that increasing the amount of Mg in the catalytic formulation, it was possible to improve the active phase stability through the formation of MgO-NiO solid solution by calcination. The extensive formation of a Ni-Rh alloy on the catalyst surface, increased the catalyst reducibility improving the dispersion of the active sites and avoided sintering phenomena during reaction. Although the substitution of Rh with Cu to form the Ni-Cu alloy did not increase the catalyst performances, a further improvement was obtained by enhancing the textural and morphological properties of the catalyst using a surfactant in the synthesis, allowing to decrease the Rh content in the catalyst formulation. The feasibility of the H<sub>2</sub> production from CB, integrating the process with a Water Gas Shift unit (S/DR-WGS) was also investigated. Using a Medium Temperature Shift (MTS) reactor and a Zr-promoted Cu/Zn/Al catalyst, good H<sub>2</sub> yields were obtained, producing a H<sub>2</sub>-rich syngas suitable for many downstream applications.

## **Abbreviations**

NG – Natural Gas

CB – Clean Biogas

SR – Steam Reforming

DR – Dry Reforming

S/DR – Steam/Dry Reforming

WGS – Water Gas Shift

HTS – High Temperature Shift

MTS – Medium Temperature Shift

LTS – Low Temperature Shift

FT – Fischer Tropsch

Ht – Hydrotalcite-type

S/CH<sub>4</sub> – Steam to Methane molar ratio

S/DG – Steam to Dry Gas molar ratio

XRD – X-ray powder Diffraction

TPR – Temperature Programmed Reduction

TPD – Temperature Programmed Desorption

TEM – Transmission Electron Microscope

SEM – Scanning Electron Microscope

WHSV – Weight Hourly Space Velocity

# Summary

Aim of the work .....	1
1. Introduction.....	2
1.1 Natural gas .....	2
1.2 Biogas .....	5
1.2.1 The biochemical process .....	6
1.2.2 Landfills .....	6
1.2.3 Wastewater treatment plants.....	7
1.2.4 Biogas plant from wastes .....	7
1.2.5 Upgrading and purification technologies .....	8
1.2.6 Production and trends.....	12
1.2.7 Utilisations.....	13
1.3 Reforming processes.....	15
1.3.1 Steam Reforming .....	16
1.3.2 Dry Reforming.....	18
1.3.3 Partial oxidation (POX) and catalytic partial oxidation (CPOX).....	22
1.3.4 Autothermal reforming (ATR) .....	23
1.3.5 Steam/Dry Reforming .....	24
1.3.6 Tri-reforming (TMR) .....	27
1.4 Syngas applications .....	27
1.4.1 Methanol synthesis.....	28
1.4.2 Fischer-Tropsch synthesis (FT).....	30
1.5 Catalysis .....	32
1.5.1 Deactivation processes .....	32
1.5.2 Heterogeneous catalysts for reforming reactions .....	36
References.....	39

2. Experimental section .....	45
2.1 Catalysts preparation.....	45
2.1.1 Synthesis by co-precipitation of hydrotalcite-type precursors .....	45
2.1.2 Synthesis by co-precipitation via surfactant-assisted-templating route .....	48
2.2 Characterization methods.....	48
2.2.1 X-Ray diffraction analyses .....	48
2.2.2 Temperature programmed reduction/desorption analyses (TPR/D).....	49
2.2.3 BET surface area and BJH pore analyses.....	49
2.2.4 Raman Spectroscopy .....	50
2.2.5 Transmission Electron Microscopy (TEM).....	50
2.2.6 Scanning Electron Microscopy (SEM) .....	50
2.2.7 Thermogravimetric Analyses (TGA) .....	50
2.3 Catalytic performance .....	51
2.3.1 Catalyst shape .....	51
2.3.2 Reduction step .....	51
2.3.3 Lab-scale plant.....	52
2.3.4 Activity tests .....	54
2.3.5 Data elaboration.....	56
References.....	56
3. Results and discussion .....	57
3.1.1 Dry Reforming of clean biogas (CB).....	57
3.1.2 Preliminary conclusions .....	71
3.2.1 Addition of steam: Steam/Dry Reforming reaction (S/DR).....	72
3.2.2 Preliminary conclusions .....	78
3.3.1 Influence of the support composition .....	79
3.3.2 Preliminary conclusions .....	88
3.4.1 Influence of Rh content.....	89

3.4.2 Preliminary conclusions .....	96
3.5.1 Substitution of Rhodium with Copper .....	97
3.5.2 Preliminary conclusions .....	107
3.6.1 Ni-based catalysts obtained <i>via</i> surfactant-assisted-templating route .....	108
3.6.2 Preliminary conclusions .....	119
3.7.1 Increase of the H <sub>2</sub> production from clean biogas by the water gas shift (WGS) reaction.....	120
3.7.2 Preliminary conclusions .....	128
References.....	129
4. Conclusions.....	130



## **Aim of the work**

The steam reforming (SR) of natural gas plays a crucial role in the production of syngas ( $\text{CO} + \text{H}_2$ ) and hydrogen, whose are widely used in the industries to produce building blocks, fuels and energy. The depletion of fossil fuels together with the environmental problems associated to the utilisation of these sources, have prompted in the last decades to the study of new and renewable fuels. One of the main candidates to replace the natural gas is the biogas that, after its purification, is a mixture of methane and carbon dioxide. Although the removal of the  $\text{CO}_2$  to obtain biomethane, that can be directly introduced in energy network, is a feasible way to exploit the clean biogas (CB), a full valorisation of its composition is more desirable from both economic and environmental point of view. In this context, the utilization of the CB in the SR process appears to be an attractive option, but the  $\text{CO}_2$  stream is hardly converted in the conditions in which the industrial process is carried out (high content of steam in the feed) decreasing the productivity of the plant. From this point of view, the Dry Reforming (DR) can represent an attractive reaction to produce syngas from the CB, although the many drawbacks of this process such as high reaction temperatures and fast coke formation are limiting its commercialization. Another interesting option is represented by the combined Steam/Dry Reforming (S/DR) reaction, in which the addition of a limited amount of steam to the DR process can mild the reaction conditions and limit the phenomena that lead to the catalyst deactivation.

With this premise, the present PhD work aims at developing a process able to valorise the CB to produce synthesis gas suitable for many downstream applications such as Fischer-Tropsch and Methanol synthesis or  $\text{H}_2$  production, acting on the catalytic formulation and optimizing the reaction conditions that can affect the feasibility of the process. The study is realized by deeply investigating the catalytic activity of different Ni-based catalysts, with the aim to suppress the deactivation phenomena typical of the reforming reactions by tuning the catalyst properties and evaluating the effect of a small amount of Rh or Cu on the catalytic performances

# 1. Introduction

Concerns about depletion of fossil fuels, energy demand and emission of greenhouse gases (GHG) have prompted renewable energy studies. Biogas up-grading and utilisation is a topic of increasing interest and its utilisation as a natural gas substitute has gained a significant attention in recent years. Biogas is generated from waste biomass via anaerobic digestion or landfills. It is regarded as a renewable source with almost neutral CO<sub>2</sub> production, and has the potential to achieve sustainable production of automotive fuels, H<sub>2</sub> and chemicals. After its purification from undesired impurities like H<sub>2</sub>S, NH<sub>3</sub> and siloxanes, biogas can be converted to syngas (a mixture of mainly H<sub>2</sub> and CO) through catalytic reforming reactions.

Although some of these processes for the natural gas conversion are widely commercialized and established worldwide, significant developments and improvements in these technologies are needed to fully valorise the biogas content, minimize the energy consumption and adjust the desired H<sub>2</sub>/CO ratio in syngas for further applications. In this context, the catalyst properties, its design and resistance to deactivation in these challenging reactions is a key point to improve the reforming processes and to obtain useful products from CO<sub>2</sub>-rich streams.

## 1.1 Natural gas

Natural gas (NG) is a gaseous hydrocarbon mixture that is formed under the earth surface. This fossil fuel can be found in oil fields, natural gas fields and coal beds. In its pure state, it is colourless and odourless, it is a combustible gas, and it gives off a significant amount of energy when burned out [1]. NG is a very safe source of energy when transported, stored and used. It is considered as a clean fuel when compared with other fossil fuels like coal and crude oil. The NG is mainly composed by (v/v) methane (96.00 %), ethane (2.00 %) and propane (0.60 %) and it is originated by one or more of three main processes:

-The thermogenic process occurs in sedimentary basins and the natural gas is formed thanks to the slow decomposition of the organic matter under the influence of temperature and pressure that increase with the depth.

-The biogenic process involves the action of living organisms (methanogenic bacteria) that decompose organic materials present in the sediments and in the early part of their burial forming the NG.

-In the abiogenic process the starting material is the volcanic gases. Methane is formed by the reduction of carbon dioxide during magma cooling, commonly in hydrothermal synthesis during water-rock interaction.

A gas reservoir is a naturally occurring storage area made of permeable and porous rocks (like sandstone) surrounded by impermeable materials. Like oil, natural gas migrates and accumulates in traps. Oil accumulations contain more recoverable energy than gas accumulations of similar size, even though the recovery of gas is a more efficient process than the recovery of oil. NG can be the primary target of either deep or shallow drilling because large gas accumulations form above the oil window as a result of biogenic processes and thermal gas occurs throughout and below the oil window. The vertical potential available for gas generation exceeds that of oil in most sedimentary basins. About a quarter of the known major gas fields are related to a shallow biogenic origin, but most major gas fields are located at intermediate or deeper levels where higher temperatures and older reservoirs exist. The two different classifications of the NG come from its origin:

- The conventional gas occurs in deep reservoirs that can be associated to the crude oil (associated gas) or not (non-associated gas). The associated gas is generally richer in higher molecular weight paraffins, while the non-associated NG typically does not contain hydrocarbons that are higher-boiling than methane. It also may contain non-hydrocarbon gases, such as carbon dioxide and hydrogen sulphide.
- The unconventional gas refers to a part of the gas resource base that has traditionally been considered difficult or costly to produce. It accumulates in geological environments that differ from conventional petroleum traps. It lays in “tight” (i.e. relatively impermeable) sandstones, in joints fractures or adsorbed into the matrix of shales and coal seams. In addition, large amounts of this gas are locked into methane hydrates in cold polar and undersea regions or dissolved/entrained in hot geopressured formation waters [2,3].

According to the *World Oil and Gas Review* by Eni [4], in the year 2016 world gas reserves increased by 0.9 % thanks to the United States, Nigeria and Iraq. At the same time the world gas demand recorded a robust growth (+2.0 %) mainly due to its increasing request in Europe (+5.4 %) and Asia-Pacific area (+5.1 %) led by a strong demand in China (+8.6 %). The global proven gas reserves in 2017 (Fig. 1.1) rose slightly by 0.4

trillion cubic metres (tcm) and this is sufficient to meet 52.6 years of global production at 2017 levels [5].

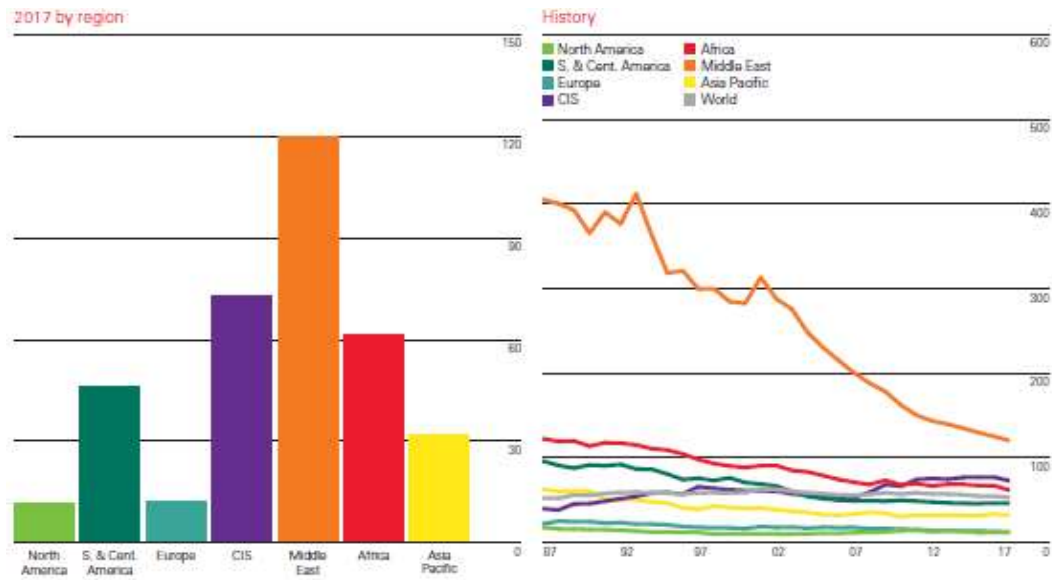


Figure 1.1. Natural gas reserves to production (R/P) ratios by region in 2017 (on the left) and an historical view (on the right) [5]

NG can be brought on the market covering long distances with different technologies: high pressure/capacity pipelines, liquefaction and re-gasification of natural gas (LNG), electric power generation and wire transportation, and finally NG conversion into transportable liquid hydrocarbons, the so-called *Gas-to-Liquids* (GtL). GtL is the process of NG conversion into transportable liquids through an intermediate step of NG conversion in syngas, followed by the production of oxygenated compounds (methanol and dimethylether) or Fischer-Tropsch synthesis to obtain middle distillates (kerosene, diesel and jet fuels, waxes, etc.) [6].

## 1.2 Biogas

Biogas (BG) is produced by the anaerobic digestion of a large variety of biological wastes and could be the main candidate to fully replace/integrate the NG in the next future. It contains three main components, which are methane ( $\text{CH}_4$ ), carbon dioxide ( $\text{CO}_2$ ) and nitrogen ( $\text{N}_2$ ). Other trace species are present as well, like hydrogen sulphide ( $\text{H}_2\text{S}$ ), hydrogen ( $\text{H}_2$ ), ammonia ( $\text{NH}_3$ ), oxygen ( $\text{O}_2$ ) and carbon monoxide ( $\text{CO}$ ). Moreover, BG is generally saturated with water, dust particles, siloxanes, aromatic and halogenated compounds [7].

BG is produced in different environments such as landfills, sewage sludge and biowaste digesters, and depending on the type of waste source, its composition can vary. BG can be used in several ways, either raw or upgraded. After its cooling and cleaning from at least  $\text{H}_2\text{S}$  to a minimum target of  $< 100$  ppm to prevent from the damages in the downstream plants, it can be utilized for various purposes (Fig.1.2):

- Production of heat and/or steam (the lowest value chain utilization)
- Electricity production with combined heat and power production (CHP)
- Industrial energy source for heat, steam and/or electricity and cooling
- Upgraded and utilization as vehicle fuel [8]
- Production of chemicals through syngas production
- Upgrading and injection in the natural gas grids as biomethane

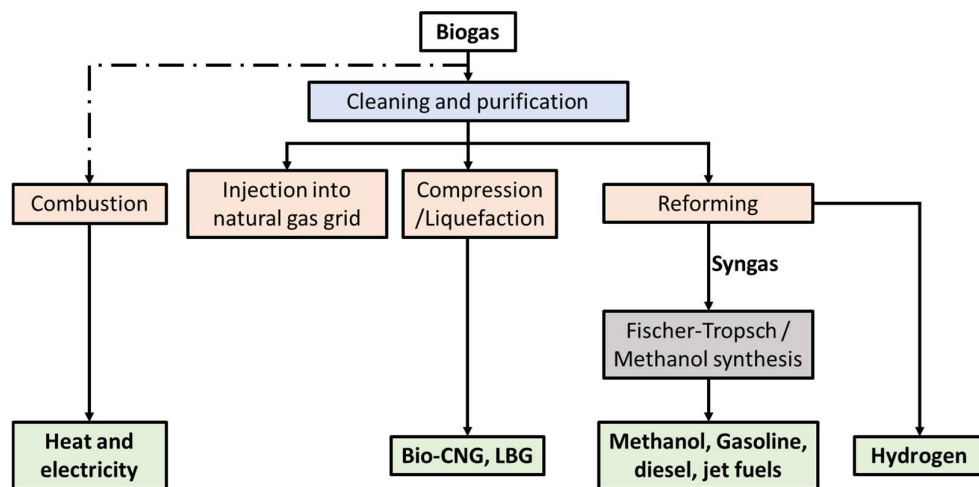


Figure 1.2. Route-map of biogas cleaning and conversion to different products

### 1.2.1 The biochemical process

Methane fermentation is a complex process, which can be divided up in four phases: hydrolysis, acidogenesis, acetogenesis/dehydrogenation and methanation (Fig 1.3) [9].

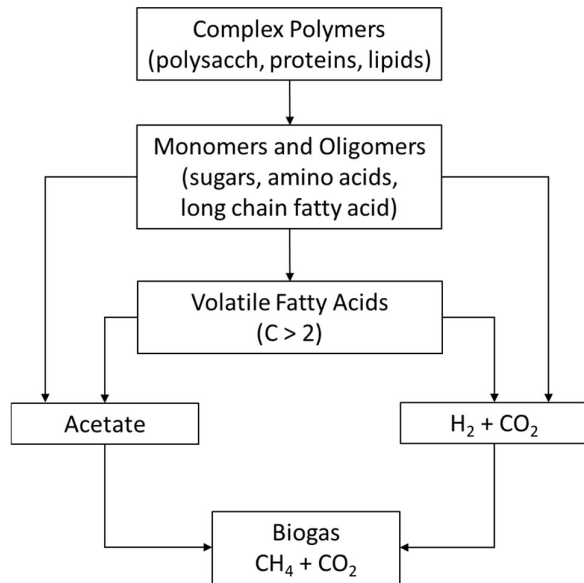


Figure 1.3. The stages of the methane fermentation process [9].

Every degradation step is carried out by different microorganisms. Hydrolysing and fermenting microorganisms are responsible for the initial attack on polymers and monomers and produce mainly acetate and hydrogen with varying amounts of volatile fatty acids. Most of these bacteria are anaerobes such as *Bacteriocides*, *Clostridia*, *Bifidobacteria*, *Streptococci* and *Enterobacteriaceae*. After that, the higher volatile fatty acids (VFA) are converted into acetate and hydrogen

by hydrogen-producing acetogenic bacteria like *Acetobacterium woodii* and *Clostridium aceticum*. At the end of the degradation chain, two groups of methanogenic bacteria produce CH<sub>4</sub> from acetate or H<sub>2</sub> and CO<sub>2</sub>. The *Methanosarcina barkeri*, *Metanonococcus mazei*, and *Methanotrix soehngenii* are strictly anaerobes and require lower redox potential for growth than most other anaerobic bacteria.

A balanced anaerobic digestion process demands that in both stages the rates of degradation have to be equal in size. If the first step runs too fast, the acid concentration rises, and the pH drops below 7.0 inhibiting the methanogenic bacteria. If the second phase runs too fast, methane production is limited by the hydrolysis stage. Methane formation takes place within a small pH interval, from about 6.5 to 8.5, with the best conditions between 7.0 and 8.0. The pH value increases by ammonia accumulation during degradation of proteins, while the accumulation of VFA decreases the pH value [10].

### 1.2.2 Landfills

Landfill BG content is generally (v/v): CH<sub>4</sub> 45-55 %, CO<sub>2</sub> 30-40 % and N<sub>2</sub> 5-15 % [11] and it is produced from degradable materials typically under non-optimised conditions.

From this point of view the main factors to be considered are the waste characteristics, landfill conditions, landfill age and climatic conditions. Even though the separation of recyclable materials has been implemented in many countries, especially the older landfills are extremely heterogenous in their material composition [12]. This means that the production and composition is affected by different filling schemes that can vary both spatially and temporally in the landfills, with some different materials placed in different part of it. Furthermore, landfill wastes also may have a high sulphur compound concentration, which then appears as sulphur compounds in the outlet gas through sulphate reduction and other mechanisms. Conditions such as temperature, pH, moisture, gas permeability and daily landfill cover may vary greatly inside the landfill body as well, affecting the BG composition and the concentration of the different contaminants.

### **1.2.3 Wastewater treatment plants**

Anaerobic digestion of sewage sludge has been applied at wastewater treatment plants (WWTP) for decades. These wastes are characterized by a high content of organic compounds that are the cause of their putrescence. The process is divided in different steps. Primary sludge contains most of the solid discharged in the sewage system and recovered in primary sedimentation. Secondary sludge is mainly microbial biomass which is generated in the biological aerobic treatment of the wastewater [13,14].

Characteristics of sewage sludge differ somewhat in different countries and areas due to water consumption and local industry. The wastewaters typically contain organic compounds and nutrients namely nitrogen and phosphorous compounds as well as different amounts of various metals from households and from industry. BG from this plant contains 55-65 % (v/v) of methane and 35-44 % (v/v) of carbon dioxide [15].

### **1.2.4 Biogas plant from wastes**

The anaerobic process is applicable for a wide range of materials including municipal, agricultural, animal and industrial wastes, and plant residues. In this case, the BG contains (v/v) 60-70 % of methane and 30-40% of carbon dioxide, [15,16] and it can be generated in centralised plants, which receive several different streams or in more specialised plants, which use mainly single substrates. This kind of plants have the general goal to convert the organic residues in BG and to another product made by the digested substrate, called digestate that can be further used as a fertilizer in agriculture. Digestate can as well be

further refined into concentrated fertilizers, fibre products and clean water, all suitable for recycling.

The mixing of different biomass substrates (co-digestion) increases the BG yield and mitigates the greenhouse gases (GHG) emissions [17]. After the mixing of the different biomasses, the digestion process takes place in the plant at mesophilic (35-45 °C) or thermophilic (45-60 °C) temperature conditions for 12-25 days. It is important to keep a constant temperature because its fluctuations can affect the BG production negatively [18]. The digested biomass is transferred to the storage tanks, which are usually covered with a gas proof membrane for the recovery of the remaining BG production. The remaining materials can be then transported back to the farms and used as fertilizers.

### **1.2.5 Upgrading and purification technologies**

Before its use, BG needs to be upgraded in most of the cases. The technologies currently developed and available at the industrial scale include adsorption, absorption (physical or chemical), membrane and cryogenic separation. With these techniques, it is possible to reduce the high concentrations of contaminants such as H<sub>2</sub>O, H<sub>2</sub>S, siloxanes and eventually CO<sub>2</sub>.

#### **Pressure Swing Adsorption (PSA)**

In this process, a solid sorbent able to remove the contaminants from the gas stream is used. By a proper choice of adsorbent, the PSA can remove CO<sub>2</sub>, H<sub>2</sub>S, moisture and other impurities either selectively or simultaneously. Molecular sieve materials such as zeolites and activated carbon are commonly used. In these solids, the tunable pore size is responsible for an easy penetration of the targeted contaminants [19,20]. The gas-solid adsorption takes place under elevated pressure until the saturation of the sorbent. Later, the pressure is reduced to desorb the contaminants [21,22]. The process is negatively affected by impurities in the raw BG, but high methane concentrations can be achieved (95-99 % v/v). However, PSA needs an extensive process control and requires high investment and operational costs [23].

#### **Absorption**

The solubility of the gaseous component in a solvent is the limiting step of this process. Raw BG meets a counter-flow of liquid in a packed column. The targeted contaminants should be more soluble in liquid than the other gases. The gas that leaves the column has

a low concentration of contaminants while the liquid leaving the packed bed has an increased concentration of BG impurities [24].

### High pressure water scrubbing (HPSW)

It is the most common and well-established technology used to remove  $\text{CO}_2$ ,  $\text{NH}_3$  and  $\text{H}_2\text{S}$  from BG since these gases are more soluble in  $\text{H}_2\text{O}$  than  $\text{CH}_4$ . In figure 1.4 the scheme of the process is shown. The operating pressure is 10 bar in a raw BG up-flow stream with the water fed counter-currently [25,26].

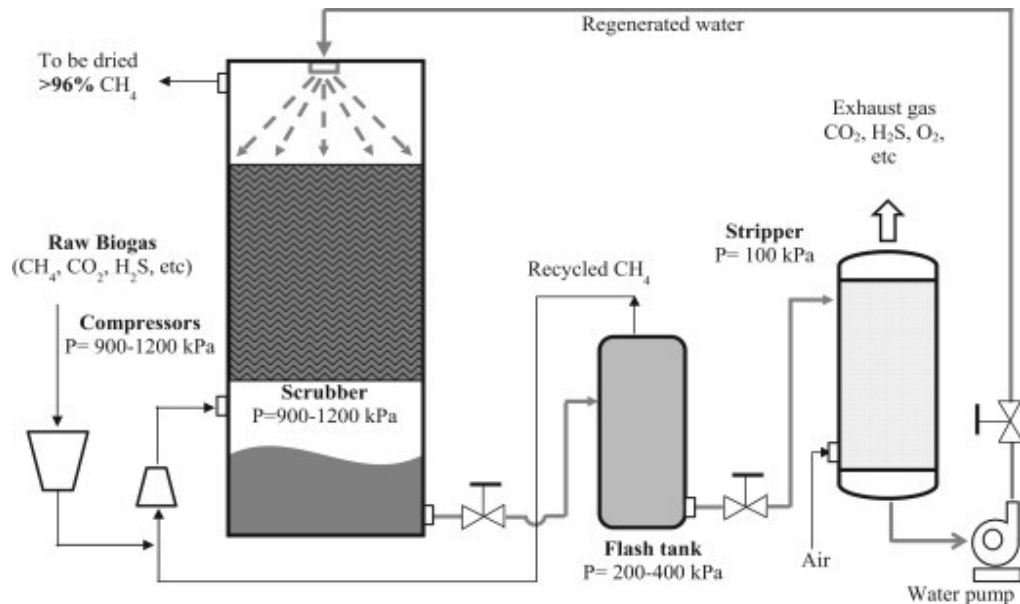


Figure 1.4. Schematic diagram of pressurized water scrubbing [26].

The process can also be used to remove  $\text{H}_2\text{S}$  selectively because of its higher solubility in water than  $\text{CO}_2$  [27]. The used water is then regenerated by stripping with air and re-used when the  $\text{H}_2\text{S}$  concentration level is low. The clean BG produced is saturated with vapor, so a drying process is required for final upgrading [28]. Although no special chemicals are required for this process, it has high investment and operational costs, with a high energy consumption during water regeneration operations [29]. The process can also run with some selected organic solvent (Organic Physical Scrubbing, OPS), with the aim to increase the contaminant solubility in the liquid. In this case also  $\text{H}_2\text{O}$ ,  $\text{O}_2$ ,  $\text{N}_2$  and halogenated hydrocarbons can be removed. Although the process has an improved efficiency in comparison to HPSW, the cost of the organic solvents and energy required for its regeneration are significantly higher [30].

### Chemical scrubbing process (CSP)

This process involves reversible reaction between adsorbed substances and solvent. To remove acid gases like  $\text{CO}_2$  and  $\text{H}_2\text{S}$ , amines like diethanolamine (DEA), monoethanolamine (MEA) and methyldiethanolamine (MDEA) are generally used [31]. In a typical amine scrubber system, the first step is the  $\text{CO}_2$  adsorption from the raw BG followed by a stripping stage, in which carbon dioxide is separated from the waste amine solution by heating the system under reduced pressure.

The raw BG enters in the adsorber from the bottom and the amine solution is supplied to the top of the column to realize a counter flow contact. The adsorption usually takes place at 40-65 °C at a pressure of 1-2 bar [32]. The bottom part of the stripper column is equipped with a reboiler at 120-150 °C where amine solution is boiled. The reboiler provides the heat of reaction for the release of  $\text{CO}_2$  from the waste amine solution and regenerates the amine solution. If  $\text{H}_2\text{S}$  is present in the raw BG, it will be adsorbed and a higher temperature for the regeneration process is needed. The main downside of this technology is the requirement to treat waste chemicals, corrosion and contaminants build-up which makes the process more complex [33].

### Membrane separation (MS)

The technology is based on the different permeability of the gases when specific conditions are applied. The membrane (Fig. 1.5) acts as a permeable barrier that allows specific compounds to pass through differently, depending on the applied driving force such as the difference in concentration, pressure, temperature, and electric charges of the different species [34].

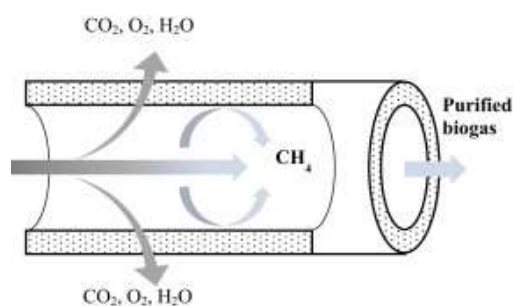


Figure 1.5. Schematic diagram of membrane permeation [26].

The membrane gas separation could be more beneficial if the gas flow is low (higher contact time) and the content of the targeted specie to be removed is high. It is a cheap

process including low operating and capital costs, low energy demand and a simple setup [35].

Most of the commercialized membranes are polymer-made, with an excellent mechanical strength, easy fabrication, high selectivity in terms of permeation and low costs [36], but they can suffer of plasticisation phenomena with the operating pressure, that can reduce the strength and the performance of the membranes [37]. Inorganic membranes are more advantageous compared to the conventional polymeric ones as they offer more mechanical strength, thermal stability and resistance against chemicals.

The most common materials used are zeolites, activated carbons, silica, carbon nanotubes (CNT) and metal-organic frameworks (MOF) [38]. The fabrication of these types of membranes is a stringent process and requires continuous monitoring due to their fragile structure. Moreover, the rigid porous materials like carbon molecular sieves and zeolites have difficulties in forming continuous and defect-free membranes for practical applications notwithstanding their superior gas separation properties [39].

The pre-removal of H<sub>2</sub>S, water, oil droplets and aerosols are necessary steps also with this technology because they can negatively affect the membrane performance.

### **Cryogenic separation (CS)**

In the cryogenic separation the contaminants are liquefied under specific pressure and temperature conditions. The process operates under a very low temperature (-170 °C) and high pressure (80 bar). The differences in the boiling point of the gases allow the purification of the raw BG stream. These harsh operating conditions are maintained using a series of compressors and heat exchangers [40] that obviously raise the capital and operation costs of this high energy demanding process.

CS can be useful if the goal is to produce liquified biomethane (LBM) and liquid natural gas (LNG) but also in this case, it is better to pre-separate H<sub>2</sub>O and H<sub>2</sub>S to avoid plugging of equipment due to the freezing of existing water in the raw BG [41].

### **Separation of trace components**

The removal of sulphur and halogenated compounds, siloxanes, water, ammonia and VOC's is a crucial step to avoid serious damages of pipelines and equipments by corrosion, together with the reduction of the commercial benefit of BG usage. The removal of H<sub>2</sub>O is performed through condensation and adsorption by silica gel, activated carbon and aluminium oxide. H<sub>2</sub>S is removed with several pre-treatments such as the use

of ZnO and Fe-based sorbents, air stripping and recovery, and adsorption on activated carbons [42]. Siloxanes are not decomposed during the anaerobic digestion and they are generally removed using activated carbons, molecular sieves and polymer pellets [43].

### 1.2.6 Production and trends

BG production and upgrading plants are spread all around the world together with the demand of higher quality biomethane to be used as a vehicle fuel or for injection in the NG grid. The small domestic scale digesters provide fuel for cooking and lighting in developing countries while large scale, farm-based and commercial electricity and heat BG plants are rising faster and faster in the developed countries. In India, in the year 2014, there were about 4.75 million farm-size BG plants, in comparison to a potential to build about 12 million BG plants, which could generate more than 10 billion m<sup>3</sup> BG/year [44]. Now many industrial processes produce BG, driven by strong water-quality standards that limit the release of effluents into waterways [45]. Large volumes of wastes are available in Africa, but BG production is still less developed than in other regions. For these reasons the African “Biogas for Better Life” initiative aims at providing two million household BG digesters by 2020 to substitute traditional cooking fuels (wood fuel and charcoal) and provide clean energy for cooking for 10 million Africans [46].

Largest BG productions occur in the United States, where it is based predominantly on the collection of landfill gas, and in Europe, where the production is more focused on the anaerobic digestion of agricultural wastes, animal manures and recovered food wastes. Figure 1.6 shows an overview of the evolution of global installed electricity BG plants capacity in recent years.

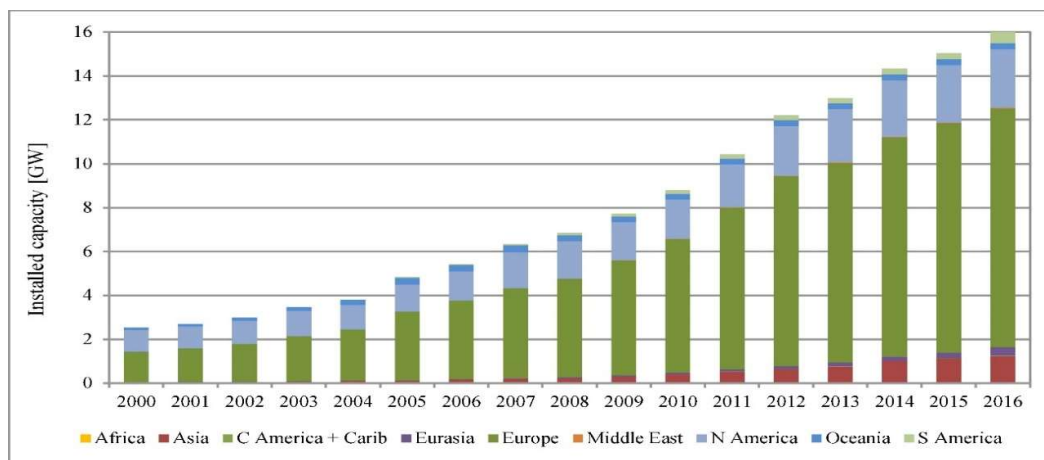


Figure 1.6. Capacity of electricity biogas plants installed globally in recent years [47].

The leading countries in Europe in the BG production are Germany, UK, Italy, Czech Republic and France, with Germany that cover about the 50 % of the total production. In the year 2015, the total BG production in EU reached 654 PJ of primary energy or more than 18 billion m<sup>3</sup> natural gas equivalent when the BG produced in the year 2000 was 92 PJ. In this context, while the contribution of landfill gas recovery to BG production has been almost constant over the last decade, the major contribution to this growth came from anaerobic digestion plants and to a lower extent as sewage gas from wastewater treatment [47].

### **1.2.7 Utilisations**

#### **Production of heat and steam**

As discussed before, this is the most common use of BG in the developing countries. Industrially, BG can also be used as a fuel in the boiler for the steam production. In this case, low quality BG can even be used with a pressure around 8-25 mbar and for a H<sub>2</sub>S level below 1000 ppm [26,48].

#### **Electricity production**

In the next future, a part of the global electricity demand is expected to be generated from BG through the combined heat and power production (CHP) [49]. Internal combustion engines, gas turbines, micro-turbines, stirling engines have been successfully generating electricity using BG [50]. For this application the water present in the raw BG have to be condensed and the H<sub>2</sub>S concentration need to be lower than 250 ppm to avoid corrosion of boiler and gas engine. The main problem of this type of BG valorisation lies in its low calorific value [51].

#### **Injection in natural gas grid**

BG can be used as a substitute of NG and after its purification can be injected into the existing NG grids. Different standards of purification are required depending on the country to avoid the corrosion of the equipments [52].

#### **Biogas to bio-compressed natural gas (bio-CNG) conversion**

After the BG upgrading to obtain bio-methane with > 97 % (v/v) CH<sub>4</sub>, the gas can be compressed at 20-25 MPa, reducing its storage volume with high energy and pressure [53]. This compressed gas has the same properties in terms of engine performance, gas

consumption and efficiency than the regular NG when it is used as vehicle fuel in the transportation market, with no significant difference in the CO<sub>2</sub> emission level [54].

### **Syngas and/or hydrogen production**

The reforming of BG using supported catalysts is an interesting method to produce hydrogen or syngas (H<sub>2</sub> + CO) for further applications. The use of BG instead of natural gas reduces the CO<sub>2</sub> emissions [55] using the already established reforming technologies. The most common catalysts used for the process are Ni-based and thus the BG should be cleaned up from H<sub>2</sub>S that is a poison for this type of catalysts. The syngas produced from the reforming of the clean BG can be used for other downstream applications such as methanol and/or Fischer-Tropsch synthesis or it can be further upgraded through a water gas shift reactor to enhance the H<sub>2</sub> yield.

If the H<sub>2</sub> produced is used in the field of the hydrogen-base polymeric fuel cells (PEMFC's) to produce electricity, the CO content of the outlet stream should be below 50 ppm to avoid the poisoning of the internal Pt-based catalysts [56]. This type of fuel cell works at low operating temperature and allows rapid start-up, it is smaller and lighter than the other fuel cells, and it is ideal in the cases where size and mobility are key parameters for the application. In recent years some of the major drawbacks such as lifetime of the fuel cell and cost of the power generated are being resolved, but further cost improvements are necessary to compete with more mature internal combustion technologies [57].

Another type of very promising fuel cell is the solid oxide fuel cell (SOFC). SOFC's are versatile with a high electrical efficiency of 55 %. This technology works at high temperatures and, for this reason, it can be effectively combined with other new energy technologies such as micro turbines, to enable the development of electricity generation products with  $\approx 70$  % efficiency [58]. SOFCs are made from commonly available ceramic materials, have no moving parts or corrosive liquid electrolytes and they require low maintenance. They are heavier than PEMFCs and thus are more suitable for stationary power generation, furthermore showing a higher tolerance to CO levels, expanding the possibilities of using an interconnected system for methane or BG reforming processes [59].

### 1.3 Reforming processes

The NG/BG reforming processes can be accomplished by means of an exothermic or endothermic reaction depending on the chemical process selected. The main reforming reactions are:

- 1- Steam Reforming (SR)
- 2- Dry Reforming (DR)
- 3- Partial Oxidation (POX and CPOX)
- 4- Auto Thermal Reforming (ATR)
- 5- Steam/Dry Reforming (S/DR)
- 6- Tri-Reforming (TMR)

While SR and POX are not indicated to be utilised for the clean BG valorisation, the other processes can be applied to produce syngas from CO<sub>2</sub>-rich stream (BG and some types of NG). The top 4 processes are already established and widely employed by industry while the last two reforming methods (combined reforming) are innovations to minimize the emissions and the energy consumption, improving the yield of the process. The choice of the reforming reaction determines the composition of the syngas produced especially in terms of H<sub>2</sub>/CO ratio. This parameter is important because different end products require different syngas ratios. Figure 1.7 shows the routes used to produce chemicals from methane/BG via syngas upgrades.

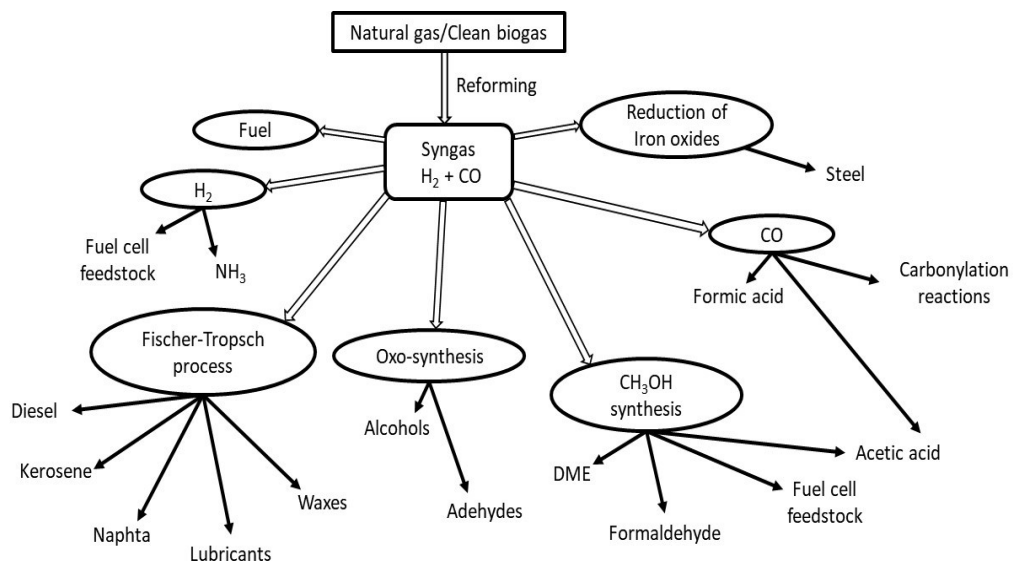
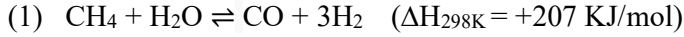


Figure 1.7. Routes for chemicals production from syngas.

### 1.3.1 Steam Reforming

The dominant process that has been in use for decades to produce hydrogen and/or syngas is the Steam Reforming (SR) of NG:



It is a catalytic process that involves a reaction between steam and NG (or other light hydrocarbons). The first industrial application of SR was in the year 1930, thus the technology is mature and used to produce almost the totality of the hydrogen (in the form of syngas) for the chemical industry [60], accounted in the year 2012 for 95 % of H<sub>2</sub> production in the U.S. [61].

SR is highly endothermic, gives a syngas with a H<sub>2</sub>/CO ratio > 3, and the process is divided in multiple steps. In the modern SR units, an adiabatic pre-reformer is located before the primary reformer to minimize the risk of sulphur poisoning in the main reformer [62]. The SR is typically carried out at 20-40 bar and at 800-1000 °C, using high steam to methane ratio (S/CH<sub>4</sub> ≈ 3 v/v) and a Ni-based catalyst placed in multiple fixed-bed tubular reactors.

The required heat to reach these temperatures is typically provided through burning of additional NG and/or from using the available energy in the separated exhaust steam through combustion or simple heat exchange. The design of the SR process is in part dictated by these constraints. The composition at the equilibrium out of the reformer is shown in figure. 1.8 as a function of the outlet temperature (26 bar and S/CH<sub>4</sub> ratio of 2.5).

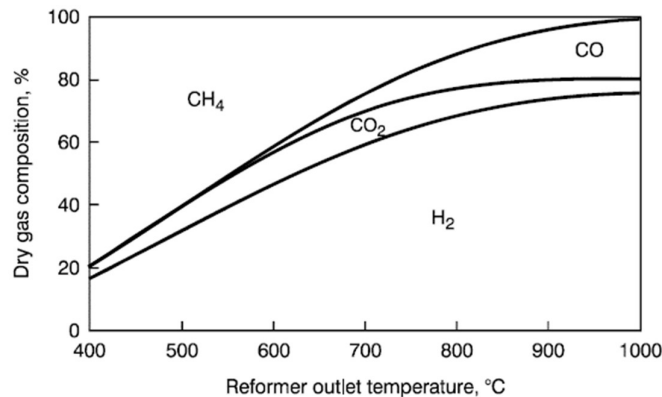


Figure 1.8. Equilibrium composition out of a steam reformer working at 26 bar and with a S/CH<sub>4</sub> ratio of 2.5 [63].

In industry, the SR reactions are typically carried out in a heated furnace. An example of a tubular reformer is shown in figure 1.9. The capacity is around 300,000 Nm<sup>3</sup>/h and it consists of a box-type radiant section including the burners and a convection section to recover the waste heat of the flue gas leaving the radiant section. The catalyst is loaded in super alloy reforming tubes placed along the furnaces. Typical tubes have a length of 10-13 m and an outer diameter of 10-15 cm.

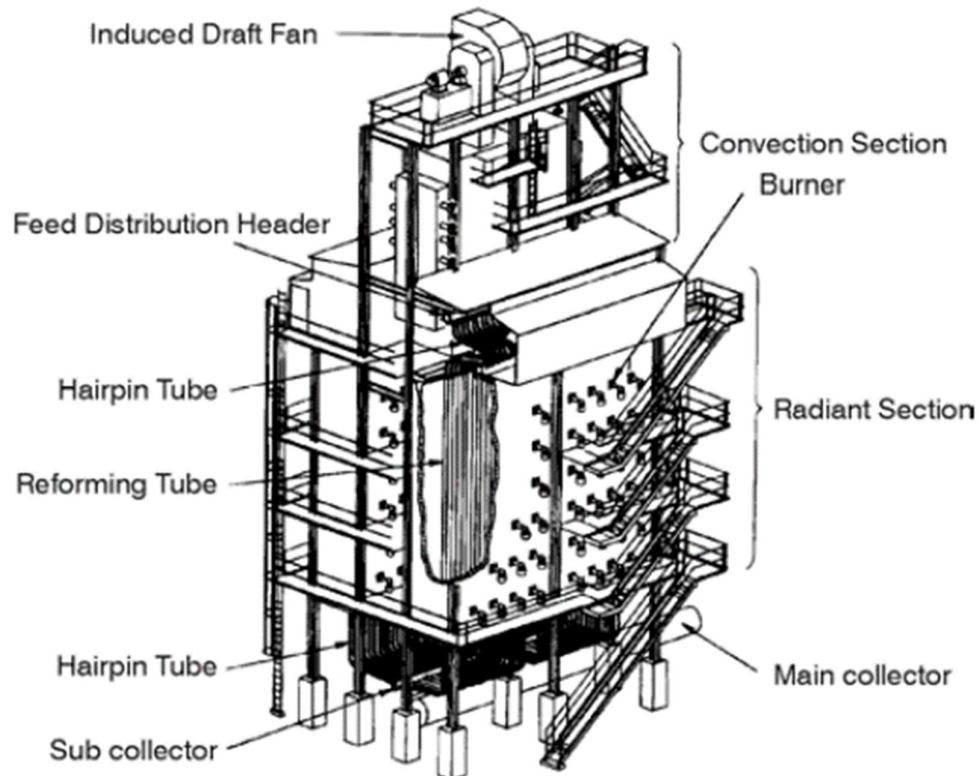


Figure 1.9. H. Topsøe A/S reformer with burners placed on side walls [63].

The catalyst activity is strictly related to the Ni<sup>0</sup> surface area and the shape of the pellets is optimised to minimize the pressure drop without negatively affecting the activity. Thus, pellets with large external diameter, like rings or cylinders with several holes, are preferred [63]. If the production of pure hydrogen is the aim of the process, the syngas exiting in the reformer (typical dry basis composition (v/v): H<sub>2</sub> 76 %, CH<sub>4</sub> 13 %, CO 12 % and CO<sub>2</sub> 10 %), is passed through a Water Gas Shift (WGS) reactor that increases the hydrogen yield converting the CO present in the syngas [64,65]:



The WGS reaction is reversible and the increase of temperature gives rise to the decrease of the reaction equilibrium constant. Low temperature conditions favour the CO

conversion, but the reaction proceeds slowly. A schematic illustration of a SR plant for hydrogen production is shown in figure 1.10.

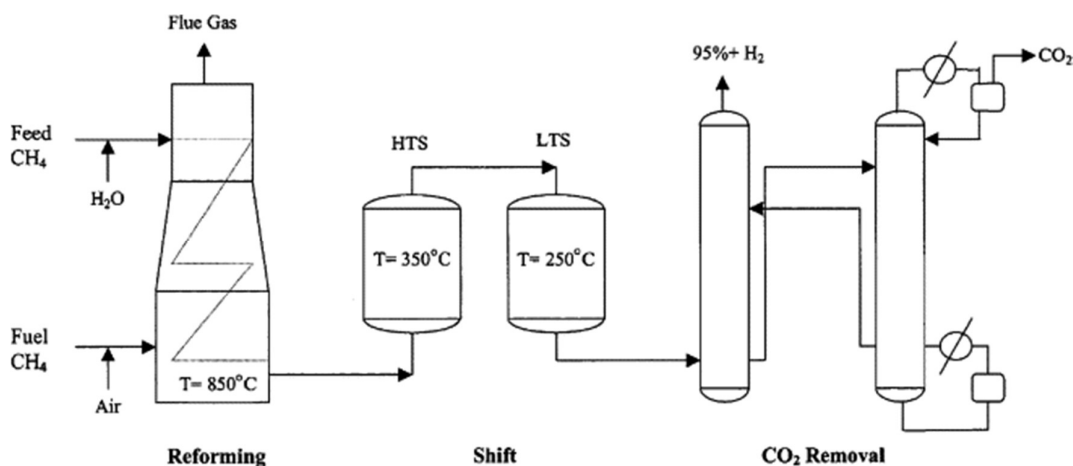


Figure 1.10. Flowsheet of a steam reforming process for hydrogen production [65].

As indicated, due to equilibrium constraints, the WGS process is performed in two reactors:

-High Temperature Shift (HTS): this stage operates between 310 °C and 450 °C at 25-35 bar using a catalyst made of magnetite with the addition of chromium oxide to improve the thermal stability [66] or the new generation of Cr-free Cu/ZnO/Al<sub>2</sub>O<sub>3</sub> catalysts [67,68].

-Low Temperature Shift (LTS): it occurs within a temperature range between 150 °C and 350 °C. Cu-based catalysts are employed because the conventional Fe-based catalysts are not active enough. CO concentrations of 0.1-0.3 % in the outlet gas can be reached [60].

The last step of the SR process is the separation of hydrogen from the CO<sub>2</sub>-containing syngas at the exit of the WGS reactor, generally realized using a Pressure Swing Adsorption unit that is also capable of producing high and stream H<sub>2</sub> purity > 99 %.

### 1.3.2 Dry Reforming

The dry reforming of methane (DR) was investigated as early as 1888. Fischer-Tropsch thoroughly studied the DR reaction over Ni and CO catalysts in the year 1928. Rostrup-Nielsen first tried to study extensively the catalysts for the reforming of hydrocarbons in the year 1964, particularly an intimate mixture of oxides of Mg, Al and Ni [69]. DR is a chemical process that consists in converting methane and carbon dioxide, identified as the world's most abundant greenhouse gases, to syngas (H<sub>2</sub>/CO ≈ 1). As a result, this

process has the potential to fully valorise the clean BG content and to mitigate the environmental challenges associated with GHG emissions [70]. The reaction governing DR is:



The reaction is extremely endothermic, favoured at low pressure as dictated by the stoichiometry, and requires high operating temperatures in the range of 800-1000 °C to achieve the desirable conversion values. Figure 1.11 shows the composition at the thermodynamic equilibrium as a function of temperature for the DR reforming process.

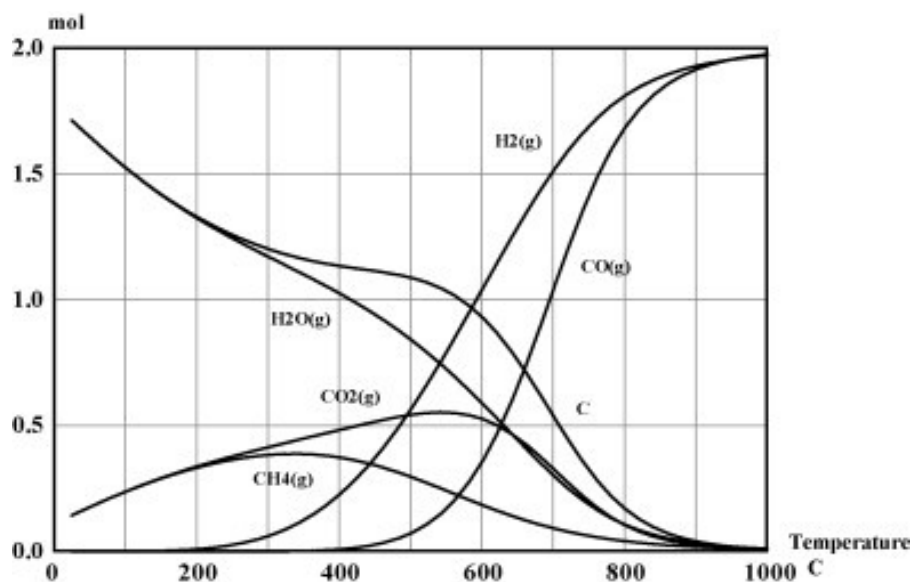


Figure 1.11. Product composition of DR of methane as a function of temperature at the thermodynamic equilibrium calculated by HSC Chemistry® [71].

The syngas produced by DR with a  $\text{H}_2/\text{CO}$  ratio of 1 can be used for the synthesis of long chain hydrocarbons or oxygenated chemicals such as acetic acid, dimethyl ether and oxoalcohols [72,73]. Despite its considerable environmental potentials, DR is not considered as an industrial mature process [74]. The major obstacle preventing from the commercialization of DR is that, in the harsh reaction conditions, coke formation and sintering quickly deactivate conventional reforming catalysts [75,76]. Although DR is mainly governed by the reaction between  $\text{CH}_4$  and  $\text{CO}_2$ , several side reactions can also occur during the process (Table 1.1).

Table 1.1 Possible reactions in the dry reforming of methane [77].

Reaction	$\Delta H_{298\text{ K}}$ (KJ/mol)	$K_{\text{eq}}$ at 573 K	$K_{\text{eq}}$ at 1373 K
(3) $\text{CH}_4 + \text{CO}_2 \rightleftharpoons 2\text{CO} + 2\text{H}_2$	247.0	-20	13
(4) $\text{CO}_2 + \text{H}_2 \rightleftharpoons \text{CO} + \text{H}_2\text{O}$	41.0	-5	2
(5) $2\text{CH}_4 + \text{CO}_2 \rightleftharpoons \text{C}_2\text{H}_6 + \text{CO} + \text{H}_2\text{O}$	106.0	-19	-5
(6) $2\text{CH}_4 + 2\text{CO}_2 \rightleftharpoons \text{C}_2\text{H}_4 + 2\text{CO} + 2\text{H}_2\text{O}$	284.0	-36	0
(7) $\text{C}_2\text{H}_6 \rightleftharpoons \text{C}_2\text{H}_4 + 2\text{H}_2$	136.0	-14	4
(8) $\text{CO} + 2\text{H}_2 \rightleftharpoons \text{CH}_3\text{OH}$	-90.6	-10	-20
(9) $\text{CO}_2 + 3\text{H}_2 \rightleftharpoons \text{CH}_3\text{OH} + \text{H}_2\text{O}$	-49.1	-12	-20
(10) $\text{CH}_4 \rightleftharpoons \text{C} + 2\text{H}_2$	74.9	-6	5
(11) $2\text{CO} \rightleftharpoons \text{C} + \text{CO}_2$	-172.4	15	-7
(12) $\text{CO}_2 + 2\text{H}_2 \rightleftharpoons \text{C} + 2\text{H}_2\text{O}$	-90.0	8	-5
(13) $\text{H}_2 + \text{CO} \rightleftharpoons \text{H}_2\text{O} + \text{C}$	-131.3	12	-6
(14) $\text{CH}_3\text{OCH}_3 + \text{CO}_2 \rightleftharpoons 3\text{CO} + 3\text{H}_2$	258.4	10	40
(15) $3\text{H}_2\text{O} + \text{CH}_3\text{OCH}_3 \rightleftharpoons 2\text{CO}_2 + 6\text{H}_2$	136.0	20	37
(16) $\text{CH}_3\text{OCH}_3 + \text{H}_2\text{O} \rightleftharpoons 2\text{CO} + 4\text{H}_2$	204.8	14	37
(17) $2\text{CH}_3\text{OH} \rightleftharpoons \text{CH}_3\text{OCH}_3 + \text{H}_2\text{O}$	-37.0	3	-1
(18) $\text{CO}_2 + 4\text{H}_2 \rightleftharpoons \text{CH}_4 + 2\text{H}_2\text{O}$	-165.0	14	-10
(19) $\text{CO} + 3\text{H}_2 \rightleftharpoons \text{CH}_4 + \text{H}_2\text{O}$	-206.2	14	-11

The main reaction of DR reforming (reaction 3) is thermodynamically favoured at  $T > 727\text{ }^\circ\text{C}$ . The methane decomposition (reaction 10), the Boudouard reaction (reaction 11), the hydrogenation of  $\text{CO}_2$  (reaction 12), together with the hydrogenation of CO (reaction 13) are the four reactions responsible for coke formation during DR. While the methane cracking (reaction 10) is favoured at high temperatures, the other three are favoured at  $T < 527\text{ }^\circ\text{C}$ . Another reaction that usually takes place is the Reverse Water Gas Shift (RWGS) (reaction 4), that leads to  $\text{H}_2/\text{CO}$  ratio lower than the unit, making the produced syngas more difficult to upgrade in further processes. [77,78] Wang *et al.* [79] reported that the RWGS and Boudouard reaction will not occur at temperatures exceeding  $820\text{ }^\circ\text{C}$ , and that the Boudouard reaction and methane decomposition will be mostly responsible for the formation of coke at temperatures ranging from  $557$  to  $700\text{ }^\circ\text{C}$ . Only few studies have dealt with the experimental application on industrial-scale DR. Mortensen *et al.* (H.

Topsøe A/S) [80] reported that the use of traditional Ni catalysts at industrial scale of DR up to 133,000 Nm<sup>3</sup>/h required to co-feed large amounts of steam to eliminate severe coke formations.

### Reaction mechanism

The mechanism of DR can be summarized in four steps as shown in figure 1.12.

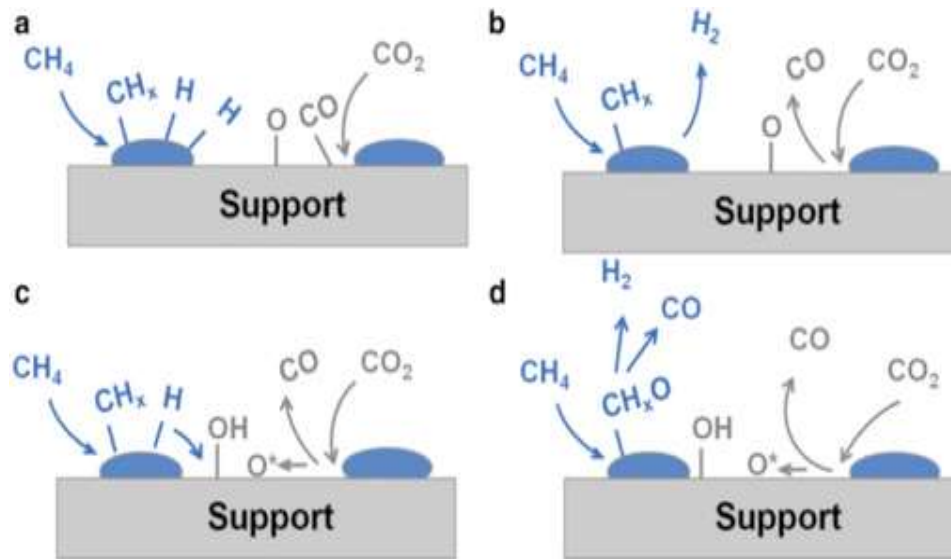


Figure 1.12 Reaction steps for the DR of methane: (a) Dissociative adsorption of CO<sub>2</sub>, (b) Fast desorption of CO and H<sub>2</sub>, (c) Formation of surface hydroxyls and oxygen spillover, (d) Formation of CO and H<sub>2</sub> [74]

#### - Dissociative adsorption of CH<sub>4</sub>

The dissociation of methane on the catalyst is generally considered to be the rate determining step. Each partially dissociated CH<sub>x</sub> species adsorbs on a site which completes its tetravalency. CH<sub>3</sub> adsorbs on top of metal atoms while CH<sub>2</sub> adsorbs as a bridge between two metal atoms. Step sites are more active than close-packed surfaces.

#### - Dissociative adsorption of CO<sub>2</sub>

It may occur in three ways: C-only coordination, C and O coordination, or O-only coordination, with both oxygen atoms bonding with the metal surface. The latter two coordination geometries are more favourable towards dry reforming. This step is generally considered fast with the CO<sub>2</sub> that tends to be adsorbed on the metal-support interface.

- Hydroxyl groups formation

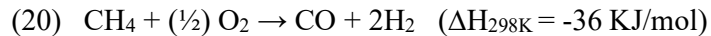
Little work has been done on the surface reaction mechanism for DR. However, it is well known that the WGs reaction is at quasi-equilibrium, meaning that the surface reactions related to it are quite fast. The models predict H<sub>2</sub> migration from the active metal particle to the support, where it forms hydroxyl groups at a temperature below 800 °C.

- Intermediates oxidation and desorption

The CH<sub>x</sub> bonded to the support (S-CH<sub>x</sub>) reacts with the surface oxygen on the metal particle to form S-CH<sub>x</sub>O groups or S-CO, which are precursors to CO formation. Another pathway considers the adsorbed CO<sub>2</sub> to form carbonates that are reduced to CO by carbon on the metal. Just as other reaction like SR, there is no clear consensus about the details of the reaction mechanism on the catalyst surface. However, in many cases, the formation and/or decomposition of formates S-CH<sub>x</sub>O to CO and H<sub>2</sub> is considered the rate determining step, especially considering that the desorption of CO and H<sub>2</sub> is fast [74].

### **1.3.3 Partial oxidation (POX) and catalytic partial oxidation (CPOX)**

The reaction takes place when a sub-stoichiometric fuel-air mixture is partially combusted in a high temperature reformer:



The reaction is exothermic and, thus considered as less energy demanding than steam or dry reforming processes. On the other hand, flowing pure oxygen can be an expensive and dangerous operation, since CH<sub>4</sub> and O<sub>2</sub> can cause an explosion if the process is not conducted properly [81]. The POX reactor is composed of two zones. The flame is placed in the first zone where fuel, oxygen and, possibly, low amounts of steam react together, while the second zone consists in a heat exchanger that recovers the excess of heat after reaction. The air-to fuel ratio and the reaction temperature (1200- 1500 °C) drive the syngas production and composition [82].

In the CPOX process, the use of a catalyst decreases the reaction temperature to 800 – 900 °C [83] and CH<sub>4</sub> is converted with oxygen or air over transition metal supported catalysts (Pt, Rh, Ir, Pd, Ni, Co) into syngas in a single step [84-87]. CPOX can be used only if the sulphur content of the inlet stream is limited to a few ppm. Higher sulphur

contents can poison the active phase of the catalyst and a non-catalytic process should be used for such fuels.

### 1.3.4 Autothermal reforming (ATR)

ATR is a combined combustion and catalytic process that has been used to produce hydrogen and CO-rich syngas for decades. The reaction takes place in an adiabatic reactor that consists of a burner, a combustion chamber and a catalyst fixed bed, contained in a refractory lined pressure shell (Fig.1.13). This particular process was designed to save energy, because the thermal energy required is generated in the partial oxidation of methane. As this process consumes the thermal energy that it produces, it is called autothermal.

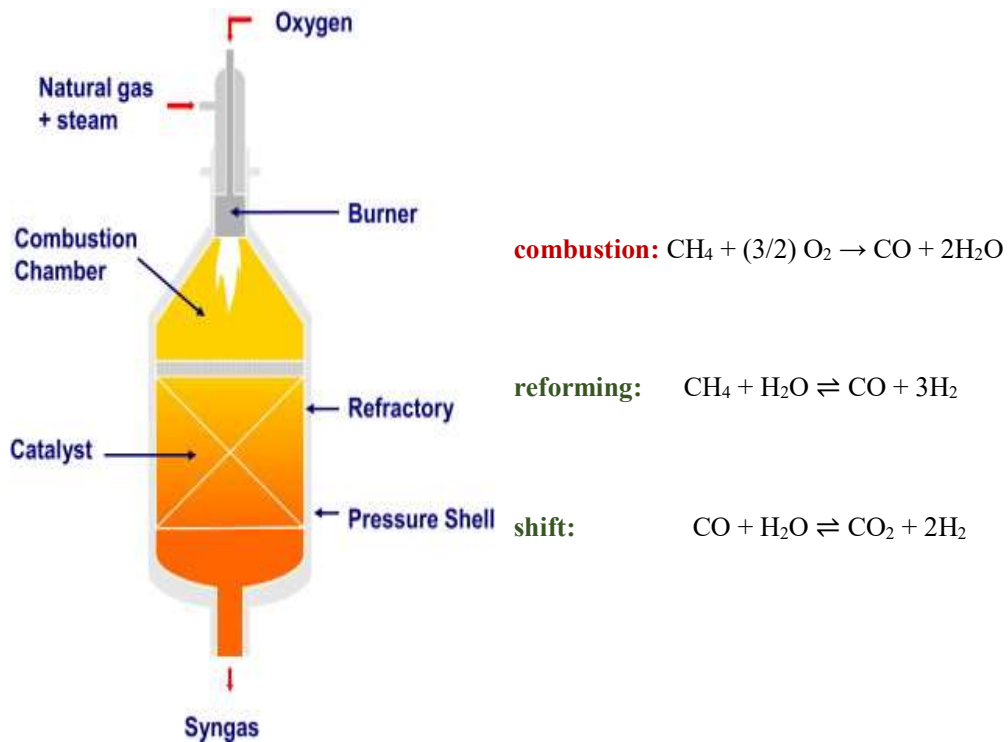


Figure 1.13. Illustration of an ATR reactor [83] and simplified reactions in the combustion chamber, on the right.

A mixture of fuel and steam is partially converted by a pressurized combustion chamber. For the production of a CO-rich syngas as feedstock for FT or methanol synthesis, operations at low values of S/C (around 0.6) are beneficial and demonstrated at pilot and industrial scales [88]. The temperature of the process is around 1100 – 1300 °C near the catalyst bed, reaching 2500 °C in the flame core. This zone can be assumed as a single reaction of CH<sub>4</sub> to CO and H<sub>2</sub>O with an O<sub>2</sub>/CH<sub>4</sub> ratio of the chosen stoichiometry, while in the catalytic zone the final conversion through heterogenous reaction of hydrocarbons

takes place (SR and WGS) to produce syngas with different  $H_2/CO$  ratios, depending on the operating conditions.

This technology is also used by H. Topsøe A/S in the two-step reforming of natural gas to produce methanol [89]; the configuration of the plant is shown in figure 1.14. From the combination of SR and ATR, it is possible to adjust the syngas composition to obtain the suitable composition ( $H_2/CO$  ratio  $\approx 2$ ). In this case the secondary reformer (ATR) requires that the first SR reactor operates with a significant leakage of unconverted methane.

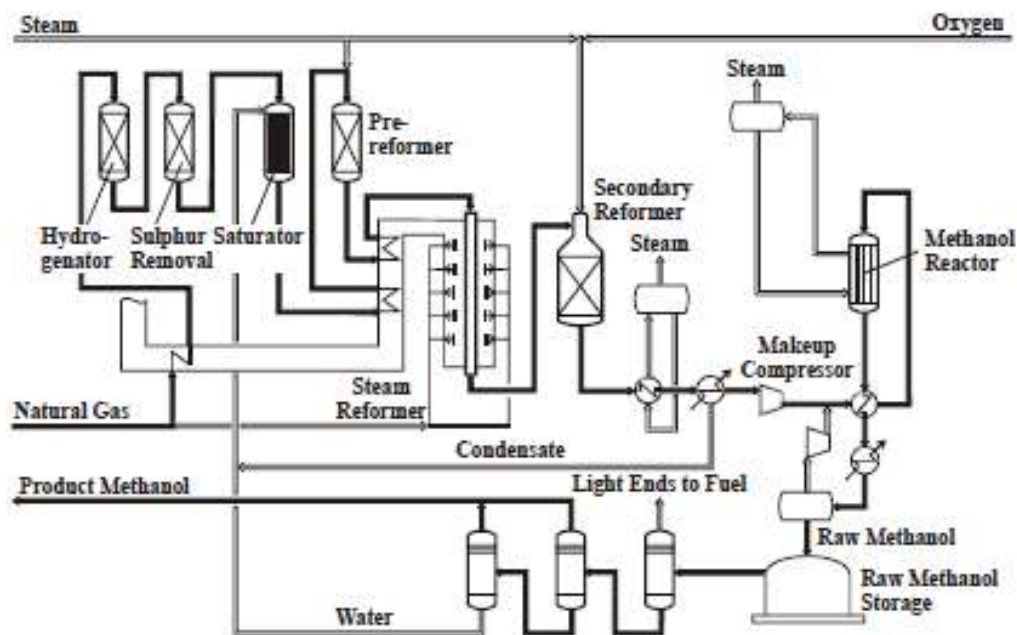


Figure 1.14 Methanol production by two-step reforming; simplified process flow diagram [89].

Only 35-45 % of reforming reaction takes place in the tubular reformer, the rest in the oxygen-fired reformer. To obtain these working conditions, the steam reformer must operate at low S/C ratios, low temperature and high pressures (low  $CH_4$  conversion conditions). The reformer tube weight is reduced by 75-80 % if compared to one-step SR, but the risk of coke formation along the tubes and on the catalytic bed is higher.

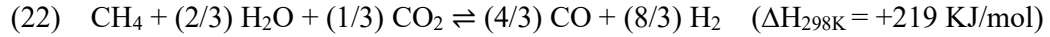
### 1.3.5 Steam/Dry Reforming

The S/DR of  $CO_2$ -rich gas (i.e. BG) is a one-step combination of the two well-known reforming reactions. Traditional SR (reaction 1) produces a syngas with a  $H_2/CO$  ratio of 3, while the stoichiometry of DR (reaction 3) yields a synthesis gas with a  $H_2/CO$  ratio of 1. The relation between the two reactions can be illustrated with the following equation:



where  $x = 1$  is the SR, while  $x = 0$  is the DR.

The combination of these two reactions leads to an endothermic process, as reported in equation 22:



That produce a syngas with a  $\text{H}_2/\text{CO}$  ratio of about 2, suitable for FT and methanol synthesis. One major feature of the process is its ability to convert  $\text{CO}_2$  from BG and/or flue gas without  $\text{CO}_2$  separation, that is often energy intensive and costly.

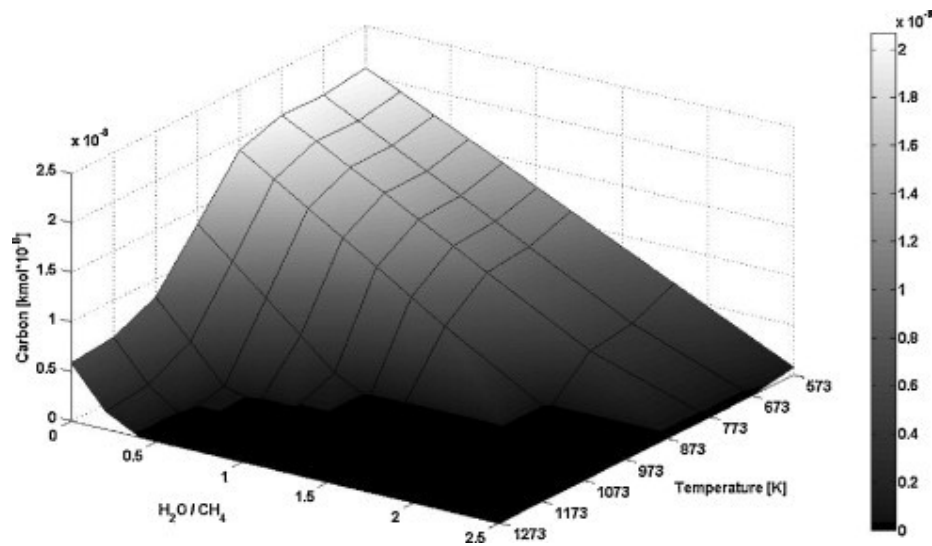


Figure 1.15. Effect of steam to carbon ratio and temperature on theoretical carbon formation rate [90].

As in the DR, the formation of coke in the reaction conditions is one of the major problems to overcome in order to realize a solid technology for the BG reforming. Chiodo *et al.* [90] have calculated the theoretical coke formation rate under different conditions by using Aspen Plus™. The inputs were: (i) BG composition (v/v)  $\text{CH}_4$  60 % and  $\text{CO}_2$  40%, (ii) reagents inlet flow temperature, (iii) temperature of the reactor, (iv) operative pressure of 1 bar. Figure 1.15 shows the results obtained for temperatures ranging from 300 to 1000 °C and the steam to carbon ratio (S/C) from 0.0 to 2.5.

In the DR conditions ( $\text{S/C} = 0.0$ ) the coke formation is favoured in all the temperature range, while the addition of steam to the mixture can considerably decrease its formation that practically disappears at  $T > 650$  °C and  $\text{S/C} > 0.5$ . Thus, the formation of coke can be avoided by raising the temperature of the reactor and/or changing the S/C ratio.

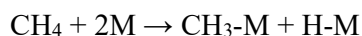
From this data it is possible to assert that the S/DR process has many practical advantages over DR reaction:

- (i) The coke formation is reduced/suppressed due to the oxidation/gasification of the carbonaceous species:  

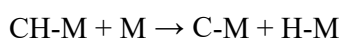
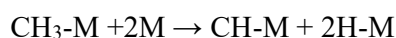
$$(23) \quad C_{(s)} + H_2O \rightarrow CO + H_2 \quad (\Delta H_{298K} = +131 \text{ KJ/mol})$$
- (ii) The production of syngas with a wider range of H<sub>2</sub>/CO ratios is possible by changing the concentration of CO<sub>2</sub> and/or steam in the feed.
- (iii) The use of steam instead of pure pressurized O<sub>2</sub> (like in the POX, CPOX and ATR) increases the safety of the plant and decreases the operational and capital costs [91].

### Reaction mechanism

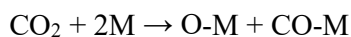
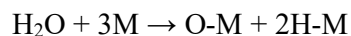
The reaction mechanism for S/DR process has been proposed by Qin *et al.* [92] using *in situ* labelled <sup>13</sup>CO<sub>2</sub> transient experiments and TPR experiments over MgO-supported noble metal catalysts. SR and DR reactions were found to start at the same time and to share the intermediate, O<sub>ad</sub>, produced by both steam and CO<sub>2</sub> dissociation. The reaction mechanism suggested is that adsorbed carbon species (CH<sub>x</sub>)<sub>ad</sub> (x = 0,1,2,3) from the activated CH<sub>4</sub>, react with O<sub>ad</sub> to produce CO. The molecular process can be described as follows (M is the active metallic site):



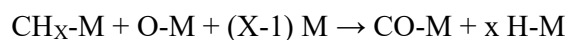
Activation of CH<sub>4</sub>



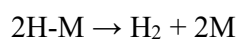
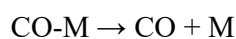
Decomposition of H<sub>2</sub>O and CO<sub>2</sub>



Reaction of adsorbed species



Production of CO and H<sub>2</sub>

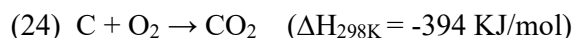


The reaction of the adsorbed species is supposed to be the rate determining step and to follow a Langmuir-Hinshelwood mechanism.

### 1.3.6 Tri-reforming (TMR)

This new process can produce syngas by adding O<sub>2</sub> to the SR/DR reaction. If pure oxygen is used, TMR shows the same drawbacks of the CPOX plant, but for this process the conversion of methane using flue gas from fossil fuel based electric power plants without pre-separation of CO<sub>2</sub> was also proposed. These flue gases typically contain (v/v) 8-10 % CO, 18-20 % H<sub>2</sub>O, 2-3 % O<sub>2</sub> 67-72 % N<sub>2</sub> and different concentrations of NO<sub>x</sub> and SO<sub>x</sub>. In this case, there is no need to handle pure oxygen and syngas with H<sub>2</sub>/CO ratios of ≈1.5-2 is produced by the combination of SR, DR and methane oxidation reactions [93].

For this application of the process, Minutillo *et al.* [94] suggested as optimum operating conditions a flue gas to methane molar ratio of 2-3 and a reforming temperature of 850 °C, estimated by thermal efficiency calculations. Addition of oxygen to the reactor feed can generate the heat required by SR and DR, doing the process more energy efficient [95], reducing also the coke formation on the catalyst thanks to the carbon oxidation reaction:



TMR can also be used for the transformation of low quality, CO<sub>2</sub>-rich NG into useful syngas [96] or for the valorisation of the BG to produce hydrogen/syngas. [97] The catalysts that can be used in the TMR are Ni-based ones, supported on a wide range of different materials (Al<sub>2</sub>O<sub>3</sub>, ZrO<sub>2</sub>, CeO<sub>2</sub>) like for DR and SR. The difference is that in TMR, the main deactivation reason is the catalyst re-oxidation due to the presence of O<sub>2</sub> in the feed [98] and Solov'ev *et al.* [95] found that a NiO/Al<sub>2</sub>O<sub>3</sub> catalyst, that reached almost 100 % of CH<sub>4</sub> conversion in the SR reaction, gave rise to a CH<sub>4</sub> conversion of only 15 % in the TMR conditions.

### 1.4 Syngas applications

Depending on the reforming process and conditions, the syngas composition can sensibly vary. After the removal of the undesired products, depending on its H<sub>2</sub>/CO ratio, the syngas can be further used to obtain chemicals, fuels or to produce electricity. The gas mixture produced by reforming of CO<sub>2</sub>-rich streams like BG, usually exhibit H<sub>2</sub>/CO ratio values between 1.0 and 2.5.

The most interesting processes to fully valorise this type of syngas and obtain high value products are the synthesis of methanol, which represents an important building block for

the chemical industry, and the FT synthesis to produce synthetic fuels and a wide range of chemicals.

### 1.4.1 Methanol synthesis

Methanol has a wide range of industrial applications and, because of that it is considered as a globally distributed product and potentially one of the best alternative fuel [99,100]. Methanol can be used to produce formaldehyde, aromatics, ethylene, methyl tertiary butyl ether (MTBE), acetic acid and other chemicals [101]. Moreover, it can be used to produce dimethyl carbonate (DMC) and biodiesel or it may provide conventional energy storage for fuel cell applications [102]. In figure 1.16 the data regarding the world methanol industrial demand are shown [103].

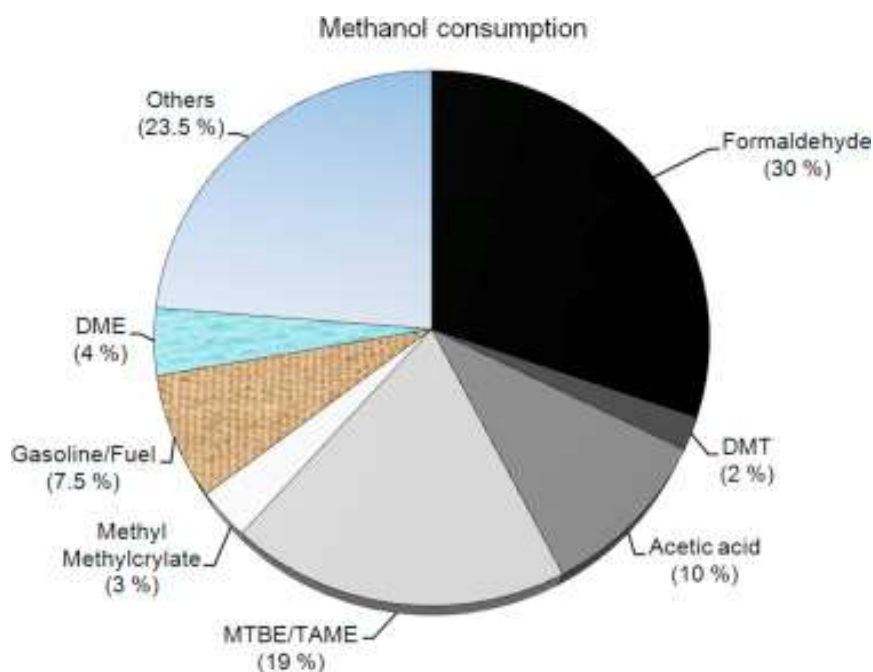


Figure 1.16. Methanol consuming industries [103].

Methanol is produced from syngas that contains a  $H_2/CO$  ratio of 2.0-2.5 and small concentrations of  $CO_2$ . The first high temperature, high pressure methanol synthesis catalyst-types were the  $ZnO/Cr_2O_3$  (Zn 20-75 % as atomic ratio) ones, operating at 300-400 °C and with the purified syngas compressed at 200-350 bar before to be fed into the reactor (Fig. 1.17) [104].

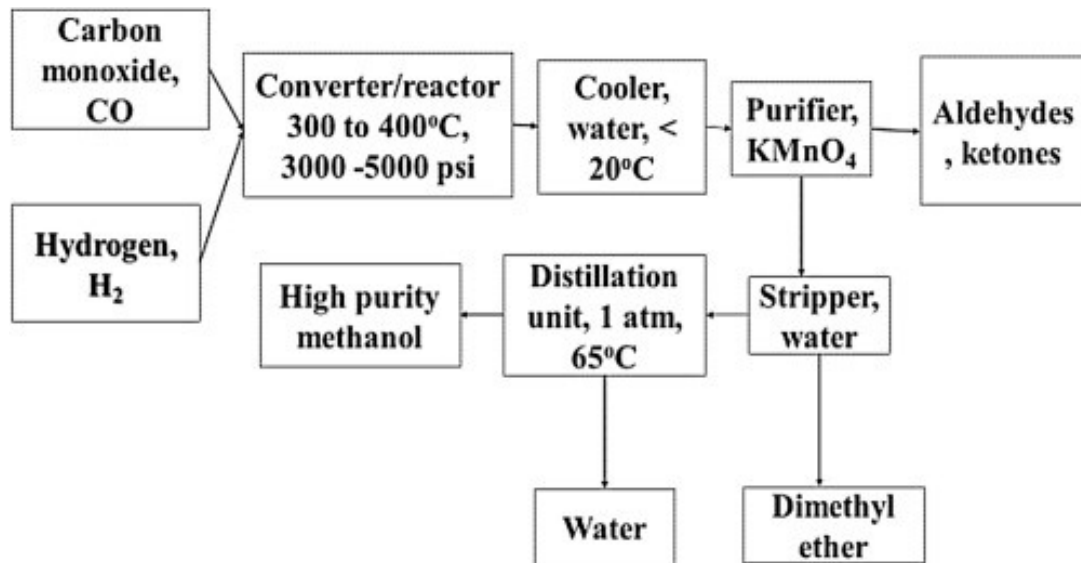


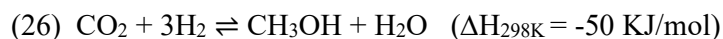
Figure 1.17. Industrial unit for methanol production at high pressure from syngas [104].

Over the years the technology was improved and a more active Cu/ZnO/Al<sub>2</sub>O<sub>3</sub> (Cu content  $\approx$  60 % as atomic ratio) catalyst was introduced, developing a new generation of methanol production plant. This new process operates at low temperature (220-275 °C) and low pressure (50-100 bar) and is, at present, used for all commercial production of methanol from syngas [60]. At normal commercial operating conditions, Cu/ZnO/Al<sub>2</sub>O<sub>3</sub> catalysts have a lifetime of 2-5 years that is drastically reduced when the gas-phase sulphur concentration is higher than 1ppm and the chlorides (mainly HCl) concentration is over 1ppb [105].



The methanol synthesis reaction is exothermic and requires significant cooling duties that are largely responsible for the investment costs of this process segment. If the reactor temperature is not properly controlled, the high exothermicity of the reaction can rapidly cause the catalyst deactivation by sintering of the Cu crystallites. The operating pressure used is necessary to shift the equilibrium towards methanol production. After the products cooling, the liquid methanol must be then carefully depressurized and purified from impurities such as aldehydes, ketones and dimethyl ether, that are usually present in concentration of 2-5 %. It should be noted that the ideal synthesis gas stoichiometry is not the molar ratio  $\text{H}_2/\text{CO} = 2.0$  as pointed out by Equation 25, but rather the module M given by the molar ratio:  $(\text{H}_2 - \text{CO}_2)/(\text{CO} + \text{CO}_2) = 2.0$ .

The temperature and, especially, the high pressure requirement for the methanol production have a serious impact on the environment and, over the past decades, the attention of the research in this field has been focused in the use of CO<sub>2</sub> to produce methanol through its hydrogenation:



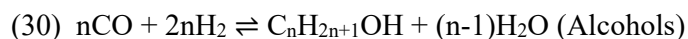
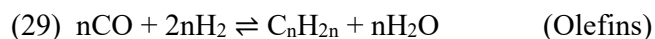
It has been reported that the addition of CO<sub>2</sub> in the CO/H<sub>2</sub> feed significantly improves the methanol yield, the energy balance, the reaction rate ( $\approx 100$  times faster) [106]. In this context, a huge number of investigations have been conducted to increase the catalyst properties in terms of surface area, active sites dispersion and particle size to increase its activity and stability [107-109].

#### 1.4.2 Fischer-Tropsch synthesis (FT)

The FT synthesis has two main characteristics: the production of a wide range of hydrocarbons and the liberation of a great amount of heat due to the exothermicity of the reaction. For these reasons, the reactor design and the development of the process is focused mainly on heat removal and the control of the reaction temperature, that would otherwise lead to an increase of the rate of deactivation (sintering and fouling) and the unwished high production of methane.

The distributions of the products are influenced by temperature, pressure, feed gas composition (H<sub>2</sub>/CO), catalyst composition and reactor design/type. Single pass FT synthesis produces a wide range of products such as olefins, paraffins and oxygenated compounds like alcohols, aldehydes, acids and ketones with water as by-product.

Depending on the types and quantities of FT products desired, the reaction can be carried out at low (200-240 °C) or high temperature (300-350 °C) using a Fe or Co catalyst. Co-based catalysts are used at low temperatures to produce high molecular weight linear waxes, while the Fe-based catalysts are used at high temperatures to obtain gasoline and low molecular weight olefins [105]. The main reactions are governed by the following equations:



After the FT synthesis it is possible to increase the yields of the wished products by applying various downstream work-up processes to obtain gasoline, diesel or chemicals. The best choice to increase the production of gasoline is to use a fluidised bed reactor and a Fe-based catalyst at 340 °C. 40 % (v/v) of straight gasoline is produced and the propene and butene contents ( $\approx 20$  % v/v) can be oligomerised to gasoline. The low octane value of this product needs anyway a further process of hydrogenation and isomerization, that makes this production less attractive than the diesel fuel option.

In this latter case, the use of a high capacity slurry bed reactor with Co-based catalyst is recommended to maximise wax production. With this configuration the straight run diesel selectivity is around 20 % (v/v) with a cetane number of about 75 (after hydrotreatment). The other products heavier than diesel (45-50 % v/v of the total) can be treated with a mild hydrocracking to produce high quality diesel. The final fuel has a cetane number around 70.

If chemicals have to be produced through the FT process, a high temperature fluidised bed reactor with Fe-based catalyst can lead to the synthesis of large amounts of  $\alpha$ -olefins up to C<sub>18</sub> atoms. These products can be used to produce polyethylene, polypropylene, acrylonitrile, etc. and the longer chain olefins can be converted to linear alcohols by hydroformylation [110].

## 1.5 Catalysis

The reforming processes, with their combination of high-pressure hydrocarbons and steam, are challenging environments for the industrial heterogeneous catalysts. The catalyst and its active phase can deactivate easily through several mechanisms which comprise strong chemisorption of contaminants from the feed, reduction of the total active surface area and decomposition of hydrocarbons to form deactivating coke. In this context, the properties and the right choice of the active phase and catalytic support, together with their synergic interactions, play an important role to enhance the catalyst life, mild the reaction conditions and decrease the operational costs of the plant.

### 1.5.1 Deactivation processes

#### Sulphur poisoning

Poisoning is the strong chemisorption of reactants, products or impurities on sites otherwise available for the catalysis. Thus, poisoning has an operational meaning: a species may act as a poison if its adsorption strength is significantly higher in comparison to those of the other species competing for the active sites. In the reforming processes that use Ni-based catalysts, one of the most severe and commonly encountered poisoning problems is caused by the chemisorption of sulphur impurities on the metal particles. In the state of the art of NG reforming, sulphur compounds are usually reduced to less than 0.5 ppm in the gas fed to the reformer and this can be achieved using hydrodesulphurization catalysts in combination with a bed of ZnO. [60] In the case of BG reforming, H<sub>2</sub>S from the feed adsorbs strongly and dissociates on Ni<sup>0</sup> surface:



The S-poisoned catalyst has essentially no activity below 700 °C. All sulphur compounds in the feed are converted into H<sub>2</sub>S at reforming conditions. The S:Ni surface stoichiometry is approximately 0.5, which corresponds to a sulphur uptake of 440 ppm (on weight basis) per m<sup>2</sup>/g of Ni. Formation of NiS is observed only at much higher sulphur levels than those normally experienced in a reformer. The maximum sulphur uptake in a reformer is therefore proportional to the Ni<sup>0</sup> surface area and is then connected to the extent of sintering of the catalyst [111].

#### Sintering

This phenomenon is strictly related to high reaction temperatures (e.g. > 500 °C) and is

generally accelerated by the presence of steam. Thermally induced deactivation of the catalysts results from: (i) loss of catalytic surface due to the growth of the catalytic phase crystallites, and (ii) loss of support area due to support collapse and/or of catalytic surface area due to pore collapse on the crystallites of the active phase. These two processes are typically referred to as “sintering” and they are driven by reduction in the total surface energy. The main mechanisms of metal crystallite growth are as follows:

- atomic migration or Ostwald ripening: involves the detachment of metal atoms from the crystallites, their migration on the support or via the gas phase and their capture on larger crystallites (Fig. 1.18 A)
- crystallite migration: involves the migration of entire crystallites over the support surface followed by collision and coalescence (Fig. 1.18 B).
- vapor transport: when the atomic migration is mediated by steam and occurs only at very high reaction temperatures.

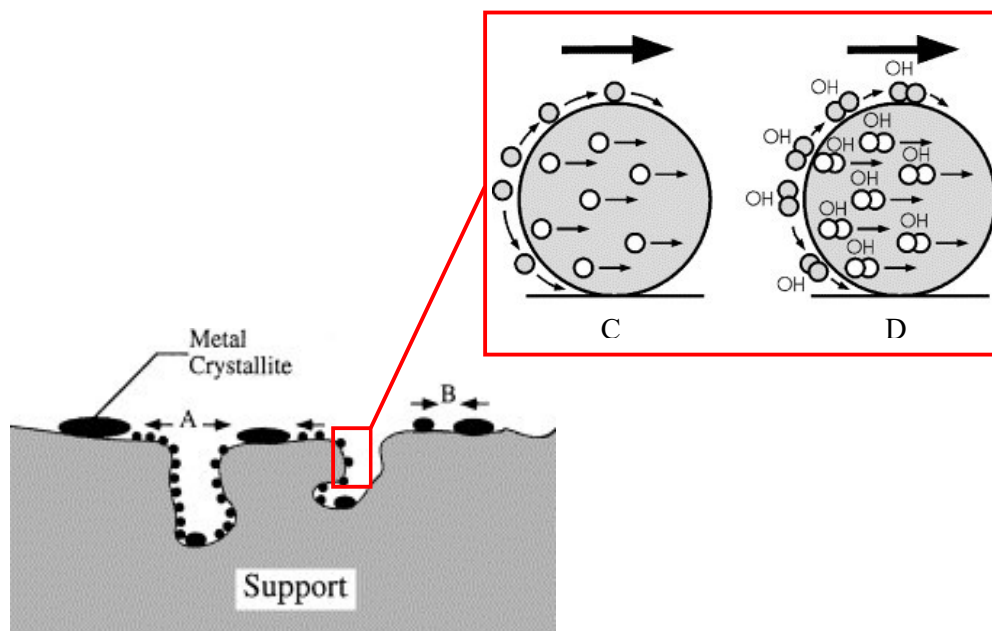


Figure 1.18 On the left, two conceptual models for crystallite growth due to sintering by: (A) atomic migration and/or (B) crystallite migration [112]. On the right, illustration of the possible mechanism for particle movement mediated by adjacent atoms (C) or Ni<sub>2</sub>OH complexes (D) [111].

At the surface of a Ni<sup>0</sup> particle, Ni-transport species as for example Ni-adjacent atoms move randomly. Transport of a Ni atom from one side of a particle to the other, results in a translational motion of the centre of the particle that produces the migration (Fig 1.18

C-D). In Figure 1.19, a series of electron microscopy images of a Ni/MgAl<sub>2</sub>O<sub>4</sub> reforming catalyst illustrates the particle migration and coalescence/sintering mechanisms (a) and the Ostwald ripening mechanism (b) [111,112].

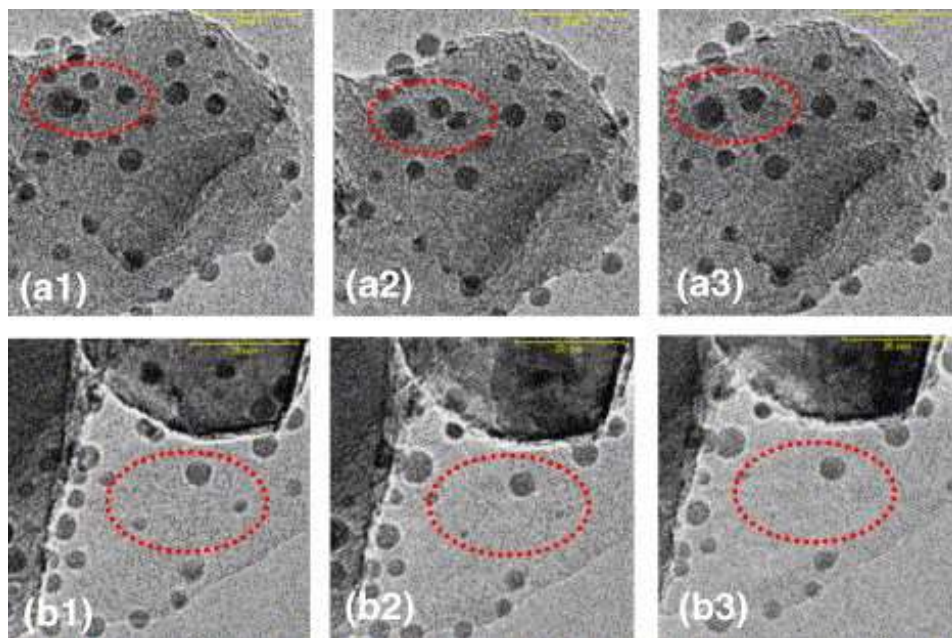


Figure 1.19 Metal particles migration by (a) coalescence/sintering mechanism, and (b) Ostwald ripening mechanism. The conditions were T: 706 °C, P: 3.1 mbar of H<sub>2</sub>. Relative times were 0.0 s (a1), 44.5 s (a2), 65.0 s (a3) and 0.0 s (b1), 41.0 s (b2), 44.5 s (b3) [111]

### Carbon formation

The risk of carbon deposition during the reforming reactions can be very high and dramatically reduces the catalyst performance in different ways. Coke may form a monolayer or physically adsorb in multilayers blocking the access of reactants to metal surface sites, plugging micro- and mesopores and, in extreme cases, growing inside the pores to the extent that causes the disintegration of catalyst pellets and plugging of the reactor voids. The main types of coke that have been observed in a reformer are three: pyrolytic, encapsulating and carbon whiskers.

- Pyrolytic carbon is generally formed from higher molecular weight hydrocarbons to high temperatures. If the catalyst activity is low (i.e. due to sulphur poisoning or sintering), higher hydrocarbons may reach high temperature in the reformer in the so called “hot bands” and decompose in this type of carbon.

- Encapsulating carbon takes place at low temperatures and high final boiling point of the hydrocarbon mixture; it consists of a thin  $\text{CH}_x$  film or layers of graphitic carbon that cover the metal particles. The carbon deposition causes a loss of catalyst activity that can be noticed as a drift in the temperature profile of the catalytic bed, with no increase in the pressure drop [111,112].

- Carbon whiskers can be the most destructive form of carbon formed during the reforming reactions. The whiskers grow as graphitic carbon at one side of the Ni particles after the reaction of hydrocarbons or CO (Fig. 1.20). Bengaard *et al.* [113] have shed light on the carbon whisker formation mechanism. From DFT calculations they found that adsorbed atomic carbon is much more stable on  $\text{Ni}^0$  steps than on  $\text{Ni}^0$  terraces. From the step sites, a graphene layer can grow because the energy of a carbon in this state is below the energy of the most stable form of surface adsorbed carbon (at the step), hence there is a driving force for graphene formation. If graphene covers the whole crystallite, encapsulating the  $\text{Ni}^0$  particle, carbon formation ceases, but if new layers nucleate below the first graphene layer by addition of carbon atoms, the detachment of the particle from the support takes place, resulting in growth of a carbon whisker from the  $\text{Ni}^0$  particle.

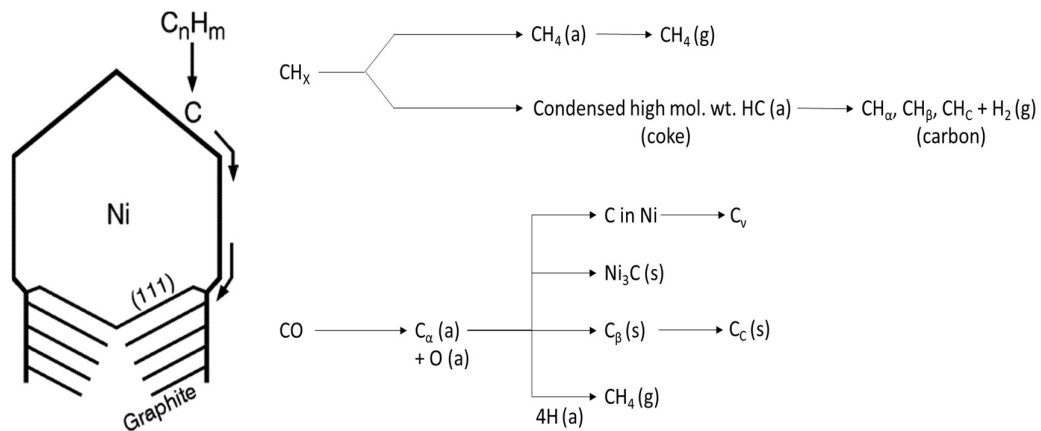
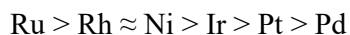


Figure 1.20. On the left, formation of carbon whiskers at the Ni particle during the reforming; on the right, formation, transformation and gasification of carbon on Ni. (s refers to adsorbed, g gaseous and s is solid state;  $\text{C}_\alpha$  atomic carbon,  $\text{C}_\beta$  polymeric carbon,  $\text{C}_c$  graphitic crystalline films,  $\text{C}_v$  fibres and/or whiskers of carbon). [111]

## 1.5.2 Heterogeneous catalysts for reforming reactions

### Active metal

Noble and transition metal-based catalysts were extensively investigated to promote the endothermic reforming reactions. As reported in the literature [80] already in the year 1993, Rostrup-Nielsen and Bak Hansen tested several metals supported on MgO and Al<sub>2</sub>O<sub>3</sub> as catalysts in the DR reaction founding the following order of activity:



Extensive research also on steam reforming has been carried out on catalysts that contain Rhodium [114], Ruthenium [115], and Platinum [116]. Hou *et al.* [117] prepared different catalysts for the DR reaction with non-noble (10 wt.% of Ni or Co) or noble (5 wt.% of Ru, Rh, Pt, Pd and Ir) metals by impregnation on  $\alpha$ -Al<sub>2</sub>O<sub>3</sub>. They found no evidences of coke deposition on the catalysts that contain noble metals, except for Pd (4.9 mg coke/g<sub>CAT</sub> · h). On the contrary, the carbon deposition values for Ni and Co were of 24 mg coke/g<sub>CAT</sub> · h and 49.4 mg coke/g<sub>CAT</sub> · h, respectively. It was concluded that among the noble metals, Rh exhibited the best performance in terms of activity and stability, followed by Ru, Ir, Pd and Pt.

The noble metals have high activity and resistance to coke formation and re-oxidation but, due to the lack of precious metals resources and their high prices, Ni-based catalysts (100-150 times cheaper than noble metals) are more widely used in industrial applications [118,119]. However, despite their apparent convenience, the high coke formation associated with the use of these catalysts leads to their deactivation in short time causing a major operational drawback. The difference in performance can be attributed to the fact that noble metals are able to better disperse on the support, retaining a small particle size in the reaction conditions. Therefore, the Ni catalysts must be modified to improve their catalytic properties.

Several studies have shown that the choice of a suitable catalyst support is a promising way to overcome the limitations of these catalysts [75]. Another approach is to use a bimetallic catalyst where a noble metal and a non-noble metal create an alloy, increasing the dispersion of the active phase and decreasing the size of the metal particles [120-122], and/or to add other metals as promoters [123,124]. Xu *et al.* [125] investigated the catalytic performance of a Ni/Co bimetallic catalysts supported on commercial  $\gamma$ -Al<sub>2</sub>O<sub>3</sub> modified with La<sub>2</sub>O<sub>3</sub> in the BG reforming. They demonstrated the formation of a Ni/Co

alloy that was able to improve pore textural properties of the catalyst, enhancing the metal particle dispersion (7Ni3Co/LaAl catalyst). The small particle size increased the catalytic activity and suppressed the coke formation in the reaction conditions.

The use of structured catalysts is also one promising option to improve the heat and mass transfer in the reactor, and Italiano *et al.* [126] tested Ni/CeO<sub>2</sub> and Ni-Rh/CeO<sub>2</sub> catalysts dip-coated on cordierite monoliths and alumina open cell foams. They observed good catalytic activity in the BG SR for the monometallic catalyst only at low space velocity, while the Ni-Rh based catalyst showed better performance, especially at low temperatures and high GHSV values, due to the Rh promoting effect. The promoting effect of noble metals addition was also investigated by Chen *et al.* in the DR reaction [127]. In their work, the promoting effect of small quantities of Pt, Pd and Rh to a Ni<sub>0.03</sub>Mg<sub>0.97</sub>O solid solution catalyst was demonstrated. The activity and the stability of the catalysts were higher for the bi-metallic catalysts. It was also found that the CH<sub>4</sub> decomposition, that is the rate-determining step of the reaction, was accelerated by the presence of alloys on the catalyst surface.

### **Catalytic support**

Generally, the support has no catalytic performance, its role being to provide high surface area for the dispersion of the active metals. On the other hand, it not only supports the catalyst in physical properties, but it also interacts with the active component to affect its performance and resistance to deactivation. High surface area and highly porous supports are desirable and its interaction with the active phase affects the reducibility and the stability of the catalysts. Properties of the catalytic support such as thermal stability (Al<sub>2</sub>O<sub>3</sub>, SiO<sub>2</sub>), oxygen storage capacity (CeO<sub>2</sub>, CeO<sub>2</sub>-ZrO<sub>2</sub>, TiO<sub>2</sub>), surface basicity (CaO, La<sub>2</sub>O<sub>3</sub>, MgO) and redox properties (CeO<sub>2</sub>, ZrO<sub>2</sub>) are of real importance to facilitate the reduction of the catalyst, avoid sintering phenomena and suppress the formation of carbonaceous species [128].

The DR reaction was tested by Wang *et al.* [129] using two kinds of oxide as support, reducible (CeO<sub>2</sub>, Nb<sub>2</sub>O<sub>5</sub>, Ta<sub>2</sub>O<sub>5</sub>, TiO<sub>2</sub>, ZrO<sub>2</sub>) and not reducible ( $\gamma$ -Al<sub>2</sub>O<sub>3</sub>, La<sub>2</sub>O<sub>3</sub>, MgO, SiO<sub>2</sub> and Y<sub>2</sub>O<sub>3</sub>). The Rh<sup>0</sup> was 0.5 wt.% in each catalyst, and under the same reaction conditions, the conversions varied changing the type of oxide, reflecting the importance of the support on the catalytic performance. The activity was higher if irreducible oxides were used in the sequence: La<sub>2</sub>O<sub>3</sub> < MgO  $\approx$   $\gamma$ -Al<sub>2</sub>O<sub>3</sub> probably due to stronger interaction between Rh<sub>2</sub>O<sub>3</sub> and support as confirmed by TPR and XRD analyses.

Metal-support interactions can crucially influence the catalytic performance of Ni-based catalysts [130] and Ewbank *et al.* [131] found that changing the preparation method of Ni-based catalysts supported on  $\gamma$ -Al<sub>2</sub>O<sub>3</sub> it is possible to increase the Ni-Al interactions, forming a core shell-like catalyst, active and stable in the DR due to the improved metal dispersion and resistance to carbon deposition. Naeem *et al.* [132] investigated the activity of Ni (5 wt.%) catalysts on several supports such as  $\gamma$ -Al<sub>2</sub>O<sub>3</sub> ( $S_{\text{BET}} = 180 \text{ m}^2/\text{g}$ ), CeO<sub>2</sub> ( $S_{\text{BET}} = 40 \text{ m}^2/\text{g}$ ), and ZrO<sub>2</sub> ( $S_{\text{BET}} = 35 \text{ m}^2/\text{g}$ ). They found that Ni-Zr catalyst showed best catalytic performance due to its combination of thermal stability, redox potential and reducibility. Ni-Ce catalyst was the less active and more prone to carbon deactivation due to the low Ni dispersion and its large Ni crystallites size. Furthermore, the best catalyst in terms of coke resistance was the Ni-Al because of the high metal dispersion on its higher surface together with its basic properties that improved the gasification of the carbonaceous species. The influence of the support basicity was also studied by Chang *et al.* [133], studying in the DR reaction Ni-based catalysts supported on alkaline-promoted zeolite. The addition of K and CaO promoted the CO<sub>2</sub> adsorption, creating an extra-supply of oxygen near the Ni<sup>0</sup> sites, preventing the sequential build-up of surface carbon. Another interesting support is MgO that with its high Lewis basicity can enhance the chemisorption of carbon dioxide. Several works [134,135] showed that Ni/MgO catalysts have high catalytic activity and stability due to the formation of a solid solution that increases the metal-support interaction. In these catalysts the Ni<sup>0</sup> active centres are more stable, well-dispersed on the surface and showed excellent anti-carbon ability.

Another property of the support that can affect the catalytic performance is its oxygen storage capacity. The oxygen defects in supports activate the CO<sub>2</sub>, weakening the C-O bond and enhancing the capability of surface oxygens to oxidize C to CO [136]. Roh *et al.* [137] carried out the DR reaction using Ni-based catalysts supported on CeO<sub>2</sub>-ZrO<sub>2</sub> solid solution obtained by co-precipitation method. Ni-Ce<sub>0.8</sub>-Zr<sub>0.2</sub>O<sub>2</sub> showed better stability in comparison to the corresponding Ni-CeO<sub>2</sub> and Ni-ZrO<sub>2</sub> catalysts, due to the higher oxygen storage capacity of the solid solution.

All these aspects are crucial to develop a highly active and stable catalyst for reforming reactions, and a good balance between the different properties of the support is one of the keys to obtain well-dispersed and carbon-resistant metal particles on the catalyst surface.

## References

1. S. Lee, J.G. Speight, S.K. Loyalka, Handbook of Alternative Fuels Technologies, 2nd ed., CRC Press, Oxford (UK), 2014, pp. 157-178.
2. J.E. Carruthers, J.P. Riva, G.I. Atwater, A.L. Waddams, L.H. Solomon, Natural gas, Britannica Online Encyclopedia, <http://www.britannica.com/science/natural-gas>
3. S. Faramawy, T. Zaki, A.A.E. Sakr, J. Nat. Gas Sci. Eng., 34 (2016) 34-54
4. World Gas and Renewable Review 2017, Eni Group, San Donato Milanese MI (I).
5. BP Statistical Review of World Energy, 67<sup>th</sup> edition, June 2018
6. C. Perego, R. Bortolo, R. Zennaro, Catal. Today 142 (2009) 9-16
7. D. Andriani, A. Wresta, Appl Biochem Biotech, 172 (2014) 1909-1928
8. M. Persson, O. Jonsson, A. Wellinger, Biogas Upgrading to Vehicle Fuel Standards and Grid Injection, IEA Bioenergy. Task 37 – Energy from Biogas and Landfill Gas, 2006
9. L. Appels, A. Van Assche, K. Willems, J.Degrève, J.Van Impe, R. Dewil, Biores. Tech. 102 (2011) 4124-4130
10. P. Weiland, Appl. Microbiol. Biotech., 85 (2010) 849-860
11. S. Rasi, A. Veijanen, J. Rintala, Energy, 32 (2007) 1375-1380
12. S. Rasi, J. Lantela, J. Rintala, Ener. Conv. Manag., 52 (2011) 3369-3375
13. P. Sosnowski, A. Wieczorek, S. Ledakowicz, Adv. Envir. Res., 7 (2003) 609-616
14. S. Luostarinen, S. Luste, M. Sillanpaa, Biores. Tech. 100 (2009) 79-85
15. O. Jonsson, E. Polman, JK. Jensen, R. Eklund, H. Schyl, S. Ivarsson, Sustainable Gas Enters the European Gas Distribution System, Danish Gas Technology Centre, Hørsholm (DK), 2003
16. Y. Chen, J.J. Cheng, K.S Creamer, Biores. Tech., 99 (2008) 4044-4064
17. J.B. Holm-Nielsen, T. Al Seadi, P. Oleskowicz-Popiel, Biores. Tech., 100 (2009), 5478-5484
18. C. Mao, Y. Feng, X. Wang, G. Ren, Renew. Sust. Energ. Rev., 45 (2015) 540-555
19. C. Grande, A. Rodrigues, Ind. Eng. Chem. Res., 46 (2007) 4595-4605
20. D. Ko, R.Siriwardane, L.T. Biegler, Ind. Eng. Chem. Res., 42 (2003),339-348
21. S. Cavenati, C. Grande, A. Rodrigues, Energy Fuels, 19 (2005) 2545-2555
22. M.T. Ho, G.W. Allison, D.E. Wiley, Ind. Eng. Chem. Res., 47 (2008) 4883-4890
23. V.G. Gomes, K.W.K. Yee, Sep. Purif. Tech., 28 (2002) 161-171

24. P. Cozma, C. Ghinea, *Clean-Soil Air Water*, 41 (2013) 917-927
25. P. Cozma, W. Wukowi, A. Friedl, M. Gavrilesco, *Clean Tech. Envir. Policy*, 17 (2014) 373-391
26. L. Yang, X. Ge, C. Wan, F. Yu, Y. Li, *Renew. Sustain. Energy Rev.*, 40 (2014) 1133-1152
27. N. Abatzoglou, S. Boivin, *Biofuel. Bioprod. Bior.*, 3 (2009) 42-71
28. R. Chandra, V.K. Vijay, P.M.V. Subbarao, *Rev. Energy*, 2 (2012) 1-6
29. J. Eze, K. Agbo, *Am. J. Sci. Ind. Res.*, 1 (2010) 604-609
30. L. Tock, M. Gassner, F. Maréchal, *Biomass. Bioenergy*, 34 (2010) 1838-1854
31. X. Chen, H.Vinh-Thang, A.A. Ramirez, D.Rodrigue, S. Kaliaguine, *RSC Adv.*, 5 (2015) 24399-24448
32. E. Privalova, S.Rasi, P. Maki-Arvela, K. Eranen, J. Rintala, D.Y. Murzin, *RSC Adv.*, 3 (2013) 2979-299
33. V. Palma, D. Barba, P. Ciambelli, *Brazilian J. Chem. Eng.*, 21 (2013) 5-6
34. A. Makaruk, M.Miltner, M. Harasek, *Sep. Purif. Tech.*, 74 (2010) 83-92
35. S. Basu, A.L. Khan, A. Cano-Odena, C. Liu, I.F.J. Vankelecom, *Chem. Soc. Rev.*, 39 (2010) 750-768
36. M.Scholz, T. Melin, M.Wessling, *Renew. Sustain. Energy Rev.*, 17 (2013) 199-212
37. A. Bos, I.G.M. Punt, M. Wessling, H. Strathmann, *J. Membr. Sci.*, 155 (1999) 67-7
38. M. Reazei, A.F. Ismail, G. Bakeri, S.A. Hashemifard, T. Matsuura, *Chem. Eng. J.*, 260 (2015) 875-885
39. C. Barboiu, B. Sala, S. Bec, S. Pavan, *J. Membr. Sci.*, 32 (2009) 514-525
40. K.E. Zanganeh, A. Shafeen, C. Salvador, *Energy Procedia*, 1 (2009) 247-252
41. M.K. Mondal, H.K. Balsora, P.Varshney, *Energy*, 46 (2012) 431-441
42. E. Ryckebosch, M. Drouillon, H. Vervaeren, *Biomass. Bioenergy*, 35 (2011) 1633-1645
43. M. Ajhar, M. Travesset, S. Yuce, T. Melin, *Biores. Tech.*, 101 (2010) 2913-2923
44. *Renewable Energy for Rural Applications*, Annual report 2013-2014, Ministry of New and Renewable Energy of India, 2014
45. *Renewables 2017, Global Status Report*, Renewable Energy Policy Network for the 21th Century REN21, Paris F).
46. W.J. Van Nes, T.D.Nhete, *Biogas for a Better Life: an African Initiative*, *Renew. Energy World*, 10(4) (1 July 2007); <https://www.renewableenergyworld.com/articles/print/volume-10/issue-4/htm>
47. N. Scarlat, J.F. Dallemand, F. Fahl, *Renew. Energy*, 129A (2018) 457-472
48. A. Abbaszaadeh, B. Ghobadian, M.R. Omidkhan, G. Najafi, *Ener. Conv. Manag.*, 63 (2012) 138-148
49. D. O. Akinyele, R.K. Rayudu, *Sust. Energy Tech. Assess.*, 8 (2014) 74-91

50. A.D. Smith, P.J. Mago, N. Fumo, *Sust. Energy Tech. Assess.*, 1 (2013) 3-12
51. Q. Sun, H. Li, J. Yan, L. Liu, Z. Yu, X. Yu, *Renew. Sust. Energy Rev.*, 51 (2015) 521-532
52. H. Hahn, K. Hartmann, M. Wachendorf, *Biores. Tech.*, 179 (2015) 348-358
53. S.S. Kapdi, V.K. Vijay, S.K. Rajesh, R. Prasad, *Renew. Energy*, 30 (2005) 1195-1202
54. K.A. Subramanian, V.C. Mathad, V.K. Vijay, P.M.V. Subbarao, *Appl. Energy*, 105 (2013) 17-29
55. H. Shiga, K. Shinda, K. Hagiwara, A. Tsutsumi, M. Sakurai, K. Yoshida, *Int. J. Hydr. Energy*, 23 (1998) 631-64
56. A. Effendi, K. Hellgardt, Z.G. Zhang, T. Yoshida, *Fuel*, 84 (2005) 869-874
57. L.C. Pérez, P. Koski, J. Ihonon, J.M. Sousa, A. Mendes, *J. Power Sources*, 258 (2014) 122-128
58. R. Kandepu, L. Imsland, B.A. Foss, C. Stiller, B. Thorud, O. Bolland, *Energy*, 32 (2007) 406-417
59. D. Hotza, J.C.D. Da Costa, *Int. J. Hydrogen Energy*, 33 (2008) 4915-4935
60. M.V. Twigg, *Catalyst Handbook*, 2<sup>nd</sup> ed., Manson Publishing, London (UK), 1996
61. Z. Wei, J. Sun, Y.Li, A.K. Datye, Y.Wang, *Chem. Soc. Rev.*, 41 (2012) 7994-8008
62. J.R. Rostrup-Nielsen, J. Sehested, J.K. Nørskov, *Adv. Catal.*, 47 (2002) 65-139
63. J.R. Rostrup-Nielsen, T. Rostrup-Nielsen, *CATTECH*, 6 (2002) 150-159.
64. A.P.Simpson, A.E. Lutz, *Int. J. Hydr. Energy*, 32 (2007) 4811-4820
65. L. Barelli, G. Bidini, F. Gallorini, S. Servili, *Energy*, 33 (2008) 554-570
66. M.C. Kung, H.H. Kung, *Surf. Sci.*, 104 (1981) 253-269
67. N.C. Schiødt, *Eur. Patent* 2,141,118 B1 (2009)
68. R. Faure, G. Fornasari, D. Gary, C. Lucarelli, N. Schiaroli, A. Vaccari, *Eur. Patent* 325,4760 A1 (2017)
69. J.R. Rostrup-Nielsen, *US Patent* 3791993 (1974)
70. J.H. Lunsford, *Catal. Today*, 63 (2000) 165-174
71. R. Raudaskoski, E. Turpeinen, R. Lenkkeri, E. Pongracz, R.L. Keiski, *Catal. Today*, 144 (2009) 318-323
72. T.D. Gould, A. Izar, A.W. Weimer, J.L. Falconer, J.W. Medlin, *ACS Catal.*, 4 (2014) 2714-2717
73. X. Xie, T. Otremba P. Littelwood, R. Schomacker, A. Thomas, *ACS Catal.*, 3 (2013) 224-229
74. N.A.K. Aramouni, J.G.Touma, B.A. Tarboush, J. Zeaiter, M.N. Ahmad, *Renew. Sust. Energy Rev.*, 82 (2018) 2570-2585
75. O. Muraza, A. Galadima, *Int. J. Energy Res.*, 39 (2015) 1196-1216

76. S. Arora, R. Prasad, *RSC Adv.*, 6 (2016) 108668-108688
77. M.N. Nikoo, N.A.S. Amin, *Fuel Process. Tech.*, 92 (2011) 678-691
78. Istadi, N. Amin, *Fuel*, 85 (2006) 577-592
79. S. Wang, G.Q. Lu, G.J. Millar, *Energy Fuels*, 10 (1996) 896-904
80. P.M. Mortensen, I. Dybjaer, *Appl. Catal. A Gen.*, 495 (2015) 141-151
81. L.S. Neiva, L. Gama, *Brazil. J. Petrol. Gas*, 4 (2010) 119-127
82. M. Pena, J. Gomez, J.L.G. Fierro, *Appl. Catal. A Gen.*, 144 (1996) 7-57
83. K. Aasberg-Petersen, I. Dybkjaer, C.V. Ovesen, N.C. Schjødt, J. Sehested, S.G. Thomsen, *J. Nat. Gas Sci. Eng.*, 3 (2011) 423-459
84. C. Cheephat, P. Daorattanachai, S. Devahastin, N. Laosiripojana, *Appl. Catal. A Gen.*, 563 (2018) 1-8
85. F. Wang, W.Z. Li, J.D. Lin, Z.Q. Chen, Y. Wang, *Appl. Catal. B Env.*, 231 (2018) 292-298
86. F. Basile, P. Benito, G. Fornasari, M. Monti, E. Scavetta, D. Tonelli, A. Vaccari, *Catal. Today*, 157 (2010) 183-190
87. A. Ballarini, F. Basile, P. Benito, I. Bersani, G. Fornasari, S. de Miguel, S.C.P. Maina, J. Viella, A. Vaccari, O.A. Scelza, *Appl. Catal. A Gen.*, 433-434 (2012) 1-11
88. J. Dahl, T.S. Christensen, S. Winter-Madsen, S.M. King, Proven Autothermal Reforming Technology for Modern Large-scale Methanol Plants, 2014 Nitrogen + Syngas Int. Conf. & Exhibition, Paris (F) 24-27 February 2014.
89. K. Aasberg-Petersen, C. Stub Nielsen, I. Dybkjaer, J. Perregaard, Large Scale Methanol Production from Natural Gas, H. Topsøe A/S Technical Bulletin.
90. V. Chiodo, F. Urbani, A. Galvagno, N. Mondello, S. Freni, *J. Power Sources*, 206 (2012), 215-221
91. M.A. Al-Nakoua, M.H. El-Naas, *Int. J. Hydr. Energy*, 37 (2012) 7538-7544
92. D. Qin, J. Lapszewicz, X. Jiang, *J. Catal.*, 159 (1996) 140-149
93. C. Song, W. Pan, *Prepr. Am. Chem. Soc., Div. Fuel Chem.*, 49 (2004) 128-131
94. A. Minutillo, A. Perna, *Int. J. Hydr. Energy*, 34 (2009) 4014-4020
95. S.A. Solov'ev, Y. Gubareni, Y. Kurilets, S.N. Orlik, *Theor. Exp. Chem.* 48 (2012) 199-205
96. C. Song, W. Pan, *Catal. Today*, 98 (2004) 463-484
97. U. Izquierdo, V.L. Barrio, J. Requies, J.F. Cambra, M.B. Guemez, P.L. Arias, *Int. J. Hydr. Energy*, 38 (2013) 7623-7631
98. H. Jiang, H. Li, H. Xu, Y. Zhang, *Fuel Process. Tech.*, 88 (2007) 988-995

99. L. William, W.L. Luyben, *Ind. Eng. Chem. Res.*, 49 (2010) 6150-6163
100. G.A. Olah, *Angew. Chem. Int. Ed.*, 44 (2005) 2636-2639
101. F.T. Zangeneh, S. Sahebdehfar, M.T. Ravanchi, *J. Nat. Gas. Chem.*, 20 (2011) 219-231
102. B. Steinhauer, M.R. Kasireddy, J. Radni, A. Martin, *Appl. Catal. A: Gen*, 366 (2009), 333-341
103. K.A. Ali, A.Z. Abdullah, A.R. Mohamed, *Renew. Sust. Energy Rev.*, 44 (2015) 508-518
104. A. Galadima, O. Muraza, *J. Nat. Gas Sci. Eng.*, 25 (2015), 303-316
105. P.L. Spath, D.C. Dayton, Preliminary Screening, National Renewable Energy Laboratory Golden, 2003, Report No.: NREL/TP-510-34929
106. M. Saito, T. Fujitani, M. Takeuchi, T. Watanbe., *Appl. Catal. A: Gen.*, 138 (1996) 311-318
107. Y. Zhang, J. Fei, Y. Yu, X. Zheng, *J. Nat. Gas Chem.*, 16 (2007) 12-15
108. Z.S. Hong, Y. Cao, J.F. Deng, K.N. Fan, *Catal. Lett.*, 82 (2009) 37-44
109. Y. Liu, Y. Zhang, T. Wang, N. Tsubaki, *Chem. Lett.*, 36 (2007) 1182-1183
110. M.E. Dry, *Catal. Today*, 71 (2002) 227-241
111. J. Sehested, *Catal. Today*, 111 (2006) 103-110
112. C.H. Bartholomew, *Appl. Catal. A: Gen.*, 212 (2001) 17-60
113. H.S. Bengaard, J.K. Nørskov, J. Sehested, B.S. Clausen, L.P. Nielsen, A.M. Molenbroek, J.R. Rostrup-Nielsen, *J. Catal.*, 209 (2002) 365-384
114. R. Horn, K.A. Williams, N.J. Degenstein, L.D. Schmidt, *J. Catal.*, 242 (2006) 92-102,
115. J.G. Jakobsen, T.L. Jorgensen, I. Chorkendorff, J. Sehested, *Appl. Catal. A: Gen.*, 377 (2010) 158-166
116. M.M.V.M. Souza, O.R.M. Neto, M. Schmal, *J. Nat. Gas Chem.*, 15 (2006) 21-27
117. Z. Hou, P.Chen, H. Fang, X. Zheng, T. Yashima, *Int. J. Hydr. Energy*, 31 (2006) 555-561
118. M. Zeppieri, P.L. Villa, N. Verdone, M. Scarsella, P.D. Filippis, *Appl. Catal. A: Gen.*, 387 (2010) 147-154
119. J.T. Richardson, M. Garrait, J.K. Hung, *Appl. Catal. A: Gen.*, 255 (2003) 69-82
120. C. Crisafulli, S. Scirè, S. Minicò, L. Solarino, *Appl. Catal. A: Gen.* 225 (2002) 1-9
121. M. García-Diéguez, E. Finocchio, M.A. Larrubia, L.J. Alemany G. Busca, *J. Catal.*, 274 (2010) 11-20
122. A. Horvath, G. Stefler, O. Geszti, A. Kienneman, A. Pietraszek, L. Guzzi, *Catal. Today*, 169 (2011) 102-111
123. A.S.A. Al-Fatesh, A.H. Fakeeha, A.E. Abasaheed, *Chin. J. Catal.*, 32 (2011), 1604-1609

124. T. Odedairo, J. Ma, J. Chen, S. Wang, Z. Zhu, J. Solid State Chem., 233 (2016) 166-177
125. J. Xu, W. Zhou, Z. Li, J. Wang, J. Ma, Int. J. Hydr. Energy, 34 (2009) 6646-6654
126. C. Italiano, R. Balzarotti, A. Vita, S. Latorrata, C. Fabiano, L. Pino, C. Cristiani, Catal. Today, 273 (2016) 3-11
127. Y. Chen, K. Tomishige, K. Yokoyama, K. Fujimoto, Appl. Catal. A: Gen., 165 (1997) 335-347
128. P. Frontera, A. Macario, A. Aloise, P.L. Antonucci, G. Giordano, J.B. Nagy, Catal. Today, 218-219 (2013) 18-29
129. H.Y. Wang, E. Ruckenstein, Appl. Catal. A: Gen., 204 (2000) 143-152
130. A. Winkler, H. Borchert, K. Al-Shamery, Surf. Sci., 600 (2006) 3036-3044
131. J.L. Ewbank, L. Kovarik, F.Z. Diallo, C. Sievers, Appl. Catal. A: Gen., 494 (2015) 57-67
132. M.A. Naeem, A.S. Al-Fatesh, W.U. Khan, A.E. Abasaeed, A.H. Fakeeha, Int. J. Chem. Eng. Appl., 4 (2013) 315-320
133. J.S. Chang, S.E. Park, H. Chon, Appl. Catal. A: Gen., 145 (1996) 111-124
134. M. Usman, W.M.A.W. Daud, RSC Adv., 6 (2016) 91603-91616
135. R. Zanganeh, M. Rezaei, A. Zamaniyan, Int. J. Hydr. Energy, 38 (2013) 3012-3018
136. P. Djinovic, J. Batista, A. Pintar, Int. J. Hydr. Energy, 37 (2012) 2699-2707
137. H.S. Roh, H.S. Potdar, K.W. Jun, Catal. Today, 93-95 (2004) 39-44

## 2. Experimental section

### 2.1 Catalysts preparation

The catalysts prepared for this research work were synthesized using different methods. The mixed oxide precursors were obtained by co-precipitation of hydrotalcite-type (Ht) precursors. The use of a non-ionic surfactant to obtain the final catalyst via surfactant-assisted templating route was also tested. The two different methodologies will be explained in the following sections.

#### 2.1.1 Synthesis by co-precipitation of hydrotalcite-type precursors

The structure of hydrotalcite-type (Ht) solids, also called Layered Double Hydroxide (LDH), may be derived from that of the brucite ( $\text{Mg}(\text{OH})_2$ ), in which the  $\text{Mg}^{2+}$  cations are octahedrally coordinated by hydroxyl ions, sharing the edges and forming octahedra layers, that are connected by hydrogen-type bonds [1]. The partial substitution of  $\text{M}^{2+}$  with  $\text{M}^{3+}$  cations with similar radius (like  $\text{Al}^{3+}$  for  $\text{Mg}^{2+}$ ) leads to positively charged layers. An anionic layer (i.e.  $(\text{CO}_3)^{2-}$ ) is sandwiched between them, compensating the positive charge, along with the water molecules trapped inside these layers (Fig. 2.1).

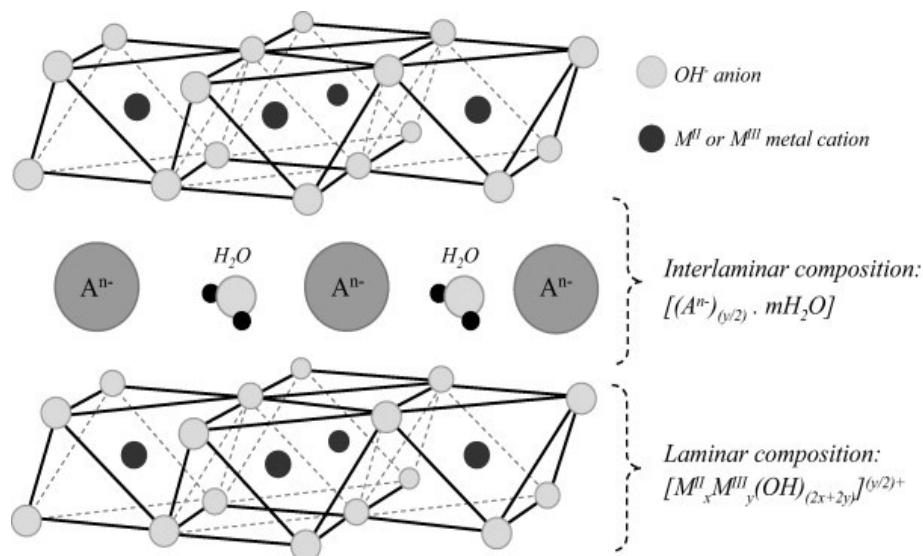
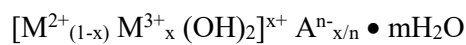


Figure 2.1. Schematic representation of the hydrotalcite-type structure [2].

The general formula of these compounds can be expressed as follow:



where  $M^{2+}$  and  $M^{3+}$  are the divalent and trivalent cations ( $Mg^{2+}$ ,  $Ni^{2+}$ ,  $Zn^{2+}$ ,  $Cu^{2+}$ , etc.),  $A^{n-x/n}$  is the interlayer anion ( $(CO_3)^{2-}$ ,  $(NO_3)^-$ ,  $(SiO_4)^{4-}$ ,  $OH^-$ ,  $Cl^-$ ,  $(SO_4)^{2-}$ ) and the water content ( $m$ ) can vary over a wide range, giving rise to a large class of isostructural solids. Ht compounds are formed with  $x$  values in the range  $0.1 \leq x \leq 0.5$ , while pure Ht materials may be obtained only for  $0.20 \leq x \leq 0.33$ ; a high concentration of trivalent cations can lead to the formation of hydroxides side phases [1,2]. These materials are widely used in catalysis because, after calcination, the obtained mixed oxides show interesting and unique properties that are difficult to obtain using other types of precursor:

- High surface area
- Chemical homogeneity and strong and tuneable Lewis basic sites
- Small crystallite size, stable to thermal treatments and able to form metal crystallites after a reduction step
- “Memory effect”, which allows the re-construction under mild conditions, of the original Ht-type structure (i.e. when the mixed oxides are put in contact with an anionic water solution)

One of the most interesting property of Ht-derived material as a catalyst, is its surface basicity which promotes the abstraction of protons from hydrocarbons. This is the initial step for dehydrogenation of hydrocarbons which leads to the hydrogen production, or syngas generation. Fine tuning of the basicity of the Ht precursors results in the formation of highly active catalysts that can be further shape up with the addition of small quantities of promoters directly in the Ht synthesis, assuring the chemical homogeneity of the final solid.

The catalysts obtained in this PhD thesis using the traditional Ht co-precipitation synthesis were prepared as follow:

1. Preparation of a  $M^{2+}$  and  $M^{3+}$  nitrate solution [2M] and of a  $Na_2CO_3$  [1M] solution in deionized water.
2. Co-precipitation by dropwise addition of the metal nitrate solution into the well stirred  $Na_2CO_3$  solution at controlled temperature ( $60^\circ C$ ) and pH (10). The pH was kept constant during the synthesis by dropwise addition of a 3M solution of NaOH.
3. Aging of the solid at the synthesis conditions for 60 min.

4. The obtained precipitate was filtered and washed carefully by a large amount of deionized water (> 500 mL/g<sub>Ht</sub>) and dried at 70 °C for 12 h.
5. Calcination of the solid at 900°C for 6 h.

The catalysts obtained following this method and tested in the reforming reactions are listed in Table 2.1. The name of the catalysts derived from the following nomenclature:



where: X = Ni wt.%; Y = M<sup>2+</sup>/M<sup>3+</sup> atomic ratio; Z = Rh or Cu wt.%

Table 2.1. Weight percent composition of the calcined catalysts obtained by co-precipitation.

Catalyst	Ni (wt.%)	Mg (wt.%)	Al (wt.%)	Rh (wt.%)
10NiMgAl2_Rh05	10.00	30.50	20.10	0.50
10NiMgAl3	10.00	35.79	14.78	///
10NiMgAl3_Rh05	10.00	35.63	14.59	0.50
10NiMgAl4	10.00	38.99	11.97	///
10NiMgAl4_Rh003	10.00	38.98	11.96	0.03
10NiMgAl4_Rh05	10.00	38.82	11.79	0.50
10NiMgAl4_Rh14	10.00	38.52	11.48	1.40
10NiMgAl4_Cu05	10.00	38.75	11.97	0.50
10NiMgAl4_Cu2	10.00	37.92	11.97	2.00

For the catalysts tested in the WGS reaction the same synthesis of the precursors was used but, during the co-precipitation the pH was kept constant to a value of 9. The nomenclature of the Cu/Zn/Al catalysts (Table 2.2) is the following:



where: Z = Zn; A = Al, C = Cu; X = Cu wt.% (2: 20 %, 04: 4 %) Y = M<sup>2+</sup>/M<sup>3+</sup> atomic ratio; Z = doping element; 50 = Al/Z as molar ratio.

Table 2.2. Weight percent composition of the Water Gas Shift (WGS) calcined catalysts obtained by co-precipitation.

Catalyst	Cu (wt.%)	Zn (wt.%)	Al (wt.%)	Zr or Ga (wt.%)
ZAC23Zr50	20.0	46.3	8.9	0.6
ZAC041Ga50	4.0	45.0	19.9	1.0

### 2.1.2 Synthesis by co-precipitation via surfactant-assisted-templating route

The synthesis of these precursors is similar to that described in the section 2.1.1. In this case a non-ionic surfactant was used to obtain the catalyst precursors:

1. Preparation of a  $M^{2+}$  and  $M^{3+}$  nitrate solution using water and a small volume of ethanol at 0 °C with a certain amount of non-ionic surfactant.
2. Co-precipitation by dropwise addition of the metal nitrate solution into the well stirred surfactant solution at controlled temperature (60°C) and pH (10). The pH was kept constant during the synthesis by dropwise addition of NaOH (1.5M).
3. Aging of the solid at the synthesis condition for 60 min.
4. The obtained precipitate was filtered and washed carefully by a large amount of an ethanol/deionized water solution (50/50 v/v) and dried at 70 °C for 12 h.

After the synthesis the solid was calcined at 900 °C (10°C/min) for 6 h and the catalysts were named as follows:



where:

10 = Ni wt.%; 4 =  $M^{2+}/M^{3+}$  atomic ratio;

X = Rh wt.%

## 2.2 Characterization methods

### 2.2.1 X-Ray diffraction analyses

The XRD powder analysis was carried out using a PANalytical X'Pert diffractometer equipped with a copper anode (Cu  $K_{\alpha}$ ,  $\lambda = 0.15418$  nm) and a fast X'Celerator detector. A  $2\theta$  range from 5° to 80° was investigated, using a step size of 0.05° and a scan step time of 15.25 s. The d value was calculated using the Bragg law (eq. 2.1) and the crystalline phases were identified by comparison with the ICSD database present in the X'Pert Highscore software.

$$(2.1) \quad \text{Bragg law:} \quad n\lambda = 2d \sin\theta$$

where:

n = reflection order (integer)

$\lambda$  = wavelength of the incident radiation

$d$  = distance between two crystalline planes

$\theta$  = diffraction angle

### **2.2.2 Temperature programmed reduction/desorption analyses (TPR/D)**

The reduction and desorption profiles were measured using a Micromeritics AutoChem II Chemisorption Analyzer, equipped with a Thermal Conductivity Detector (TCD). The analyses were carried out loading  $\approx 100$  mg of sample in a quartz reactor and using two different procedures for H<sub>2</sub>-TPR and CO<sub>2</sub>-TPD experiments.

#### **H<sub>2</sub>-TPR**

- Pre-treatment: the sample was pre-treated under He (30 mL/min) from room temperature (r.t.) to 500 °C (10 °C/min) and hold at this temperature for 1 h.
- Reduction: after cooling to 35 °C, the reduction analysis was performed using a 5 % H<sub>2</sub>/Ar (v/v) mixture (30 mL/min), increasing the temperature of the sample to 900 °C (10 °C/min) and keeping this temperature for 1 h.

#### **CO<sub>2</sub>-TPD**

- Pre-treatment: the sample was pre-treated under He (30 mL/min) from r.t. to 500°C (10 °C/min) and hold at this temperature for 2 h.
- CO<sub>2</sub> adsorption: after cooling to 40 °C, the CO<sub>2</sub> adsorption was performed using a 10 % CO<sub>2</sub>/Ar (v/v) mixture (30 mL/min) at constant temperature for 2 h.
- CO<sub>2</sub> desorption: the physisorbed CO<sub>2</sub> was removed by He purging (30 mL/min) for 1 h. Then, the sample was heated up to 900 °C (10 °C/min) under a stream of He (30 mL/min), while the desorbed CO<sub>2</sub> was monitored and recorded using an online Mass Spectrometer (Cirrus 2, MKS instruments), that was calibrated by manual injections of pure CO<sub>2</sub> ( $m/z = 44$ ) pulses.

### **2.2.3 BET surface area and BJH pore analyses**

The surface area values of the catalysts were determined by N<sub>2</sub>-physisorption at -196°C using the Braunauer-Emmer-Teller (BET) method using a Carlo Erba Sooty instrument. The sample (0.3 g) was pretreated at 150 °C under vacuum to eliminate impurities and adsorbed water then analysed in a liquid bath of N<sub>2</sub>. The BJH analyses were carried out using a Micromeritics ASAP 2020 instrument; solid samples were heated up to 150 °C

and evacuated at a pressure better than 0.02 Torr, kept for 120 min at this temperature, and lastly heated up to 250 °C for calcined samples only and kept at this temperature for 30 min.

#### **2.2.4 Raman Spectroscopy**

The Raman spectroscopy analyses were carried out to evaluate the presence and type of carbon formed on the catalyst surface during the reaction. The experiments were performed using a Renishaw RM1000 instrument equipped with a microscope to focus the beam in the zone of interest. The laser beam used was green (Ar<sup>+</sup> 514.5 nm) with a relative power of 10 % to avoid the oxidation of the carbon eventually present in the sample. The spectra were recorded in the region 4000 – 200 cm<sup>-1</sup>, with an acquisition time of 10 s and a total of 10 accumulations.

#### **2.2.5 Transmission Electron Microscopy (TEM)**

Transmission electron microscopy characterization was carried out by a TEM/STEM FEI TECNAI F20 microscope, equipped with an EDS analyser. Powder catalysts were suspended in ethanol under ultrasounds for 20 min. The suspension was subsequently deposited on an Au grid with lacey multi-foil carbon film and dried at 100 °C before doing the measurement. The distribution of the metallic particles on the catalysts surface before and after reaction was determined by statistical distribution of at least 200 particle diameters.

#### **2.2.6 Scanning Electron Microscopy (SEM)**

The samples analyses by SEM/EDS technique were performed using an EVO 50 Series Instrument (LEO ZEISS) equipped with an INCAEnergy 350 EDS micro-analyses system and an INCASmartMap for imaging the spatial variation of elements in a sample (Oxford Instruments Analytical). The accelerating voltage was 25 kV, the beam current 1.5 nA, and the spectra collection time 100 s.

#### **2.2.7 Thermogravimetric Analyses (TGA)**

TG analyses were carried out on a TA instrument Q600 equipped with a FT-IR after the heating chamber for the analyses of the gasses released during the experiments. 8-10 mg of sample were placed in an Alumina pan, heated up to 900 °C (10 °C/min) and kept 10 min at this temperature under a continuous flow of synthetic air (100 ml/min).

## 2.3 Catalytic performance

### 2.3.1 Catalyst shape

The catalysts obtained by calcination of the dried Ht precursors were pressed at 10 t for 20 min to produce a tablet, crushed and sieved to obtain particles with a dimension in the range 30-40 mesh. The particle size is crucial to optimize the radial temperature gradient and reduce the diffusion effects ( $d_{\text{reactor}}/d_{\text{catalysts}} \geq 5$ ).

### 2.3.2 Reduction step

Before the catalytic tests, an activation by reduction step of the catalysts was necessary. The reduction procedure used was different for the Steam/Dry Reforming (S/DR) and Water Gas Shift (WGS) reactions.

#### Steam/Dry Reforming

- 1) Air present in the reactor was removed by flowing N<sub>2</sub> at r.t. for 30 min. Then, the reactor was heated up to 300 °C (10 °C/min), increasing the pressure to 5 bar.
- 2) At 300 °C and 5 bar, a mixture of H<sub>2</sub>/N<sub>2</sub> (1/10 v/v, total flow: 200 ml/min) was fed to the reactor for 30 min.
- 3) The reactor temperature was increased to 900 °C (5 °C/min) under a continuous flow of H<sub>2</sub>/N<sub>2</sub> and kept 1 h at this temperature

#### Water Gas Shift

For Medium Temperature Shift (MTS) catalysts the reduction step was performed feeding a mixture of H<sub>2</sub>/N<sub>2</sub> at 10 bars and with a Weight Hourly Space Velocity (WHSV) between 340 and 450 ml/(h·g<sub>cat</sub>), following this procedure:

- 1) Air present in the reactor was removed using a flow of N<sub>2</sub> and heated up to 175 °C (1 °C/min) in 90 min.
- 2) At 175 °C, the reduction started using a flow of 1.2 % H<sub>2</sub>/N<sub>2</sub> (v/v) and hold for 2 h at this temperature.
- 3) The reactor temperature was then increased to 220 °C (1°C/min) without changing the composition of the gas flow.
- 4) At 220 °C, H<sub>2</sub> was added up to 4 % H<sub>2</sub>/N<sub>2</sub> (v/v) and hold for 20 h.

For High Temperature Shift (HTS) catalysts the reduction was performed feeding the reaction mixture (CO, CH<sub>4</sub>, CO<sub>2</sub>, H<sub>2</sub> v/v) and steam [Steam to Dry Gas (S/DG) 0.29 or 0.55 v/v] at 10 bar and with a GHSV of 1200 h<sup>-1</sup>:

- 1) Air present in the reactor was removed using a flow of N<sub>2</sub> and heating up to 275 °C (10 °C/min).
- 2) At 275 °C the reduction step began using the reaction mixture.
- 3) The reactor was heated up to 350 °C (0.5 °C/min).

### 2.3.3 Lab-scale plant

The catalytic tests were performed in the laboratory scale plants reported in Figures 2.2 and 2.3 for the S/DR and WGS reaction, respectively. The plants used were very similar except for the feed section: for the S/DR plant it consisted in four gas lines (N<sub>2</sub>, H<sub>2</sub>, CH<sub>4</sub>, CO<sub>2</sub>) plus the steam generator section, while the WGS feed section was composed by three gas lines (N<sub>2</sub>, H<sub>2</sub>, and Dry Gas: CO, CH<sub>4</sub>, CO<sub>2</sub>) and the line to feed steam. Gas flow rates were controlled by thermal mass flow controllers (BROOKS instruments), while deionized H<sub>2</sub>O was fed by a HPLC Jasco pump. The steam generator operated at 250 °C and water was mixed with the other gasses after vaporization at the inlet of the reactor. The reaction section was composed by a fixed bed reactor (INCOLOY 800HT: 19-23 % Cr, 30-35 % Ni, 39.5 % Fe and 0.06-0.1 % C) with an internal diameter of 10 mm (WGS reactor) or 8 mm (S/DR reactor), vertically placed into an electric tubular furnace. The internal temperature profiles were measured with a cromel/alumel thermocouple inserted inside the reactor. The catalysts (mass = 1.0 g) were loaded in the isothermal zone, between two layers of inter material (20 mesh quartz particles). The unreacted water was completely separated from the exit stream by a cooled gas liquid separator maintained at 1 °C. The operating pressure was controlled by a pressure controller (BROOKS instruments) placed after the condenser, while the gas stream was sent to the analysis section. The gas flows were measured by a gas flowmeter and the composition of the stream was analysed by an online gas chromatograph (Agilent Technology 7890A GC) equipped with a CarboPLOT P7 (carrier gas: H<sub>2</sub>, 27.5 m/ 750 µm/ 25 µm) and a HP-Molesieve (carrier gas: N<sub>2</sub>, 30 m/ 530 µm/ 50 µm) columns and two Thermal Conductivity Detectors (TCD).

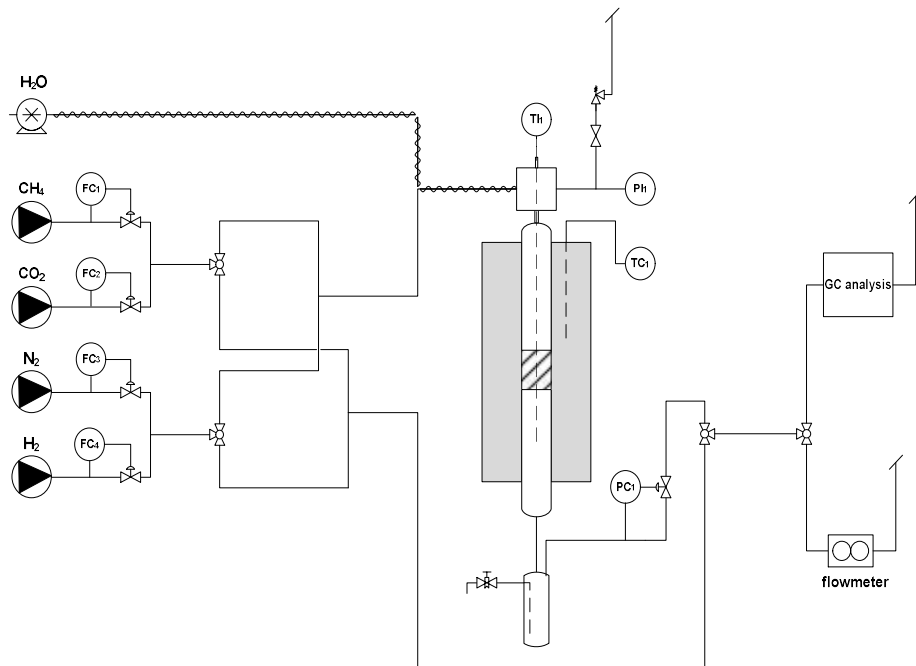


Figure 2.2. Flow diagram of the lab-scale S/DR pilot plant.

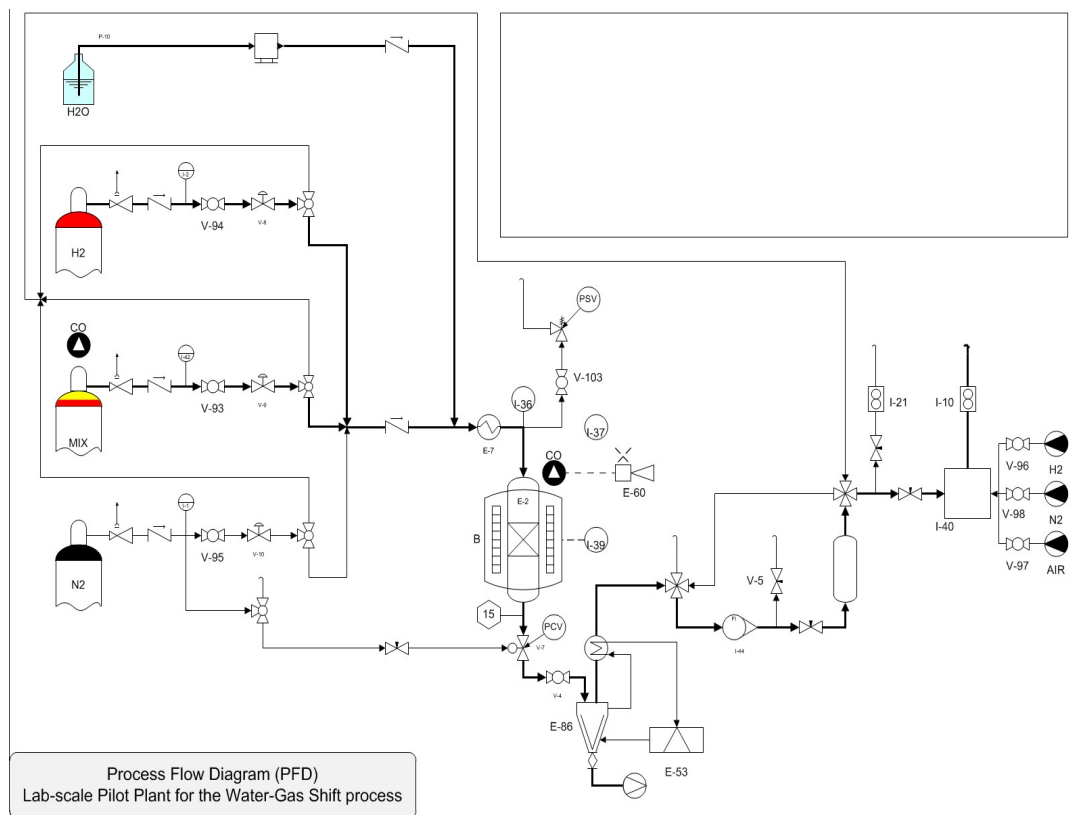


Figure 2.3. Flow diagram of the lab-scale WGS pilot plant.

### 2.3.4 Activity tests

#### Dry and Steam/Dry Reforming tests

The study was focused at first on the feasibility of the Dry Reforming Reaction on Ni-based catalysts. In this case an equimolar mixture of CH<sub>4</sub> and CO<sub>2</sub> was fed to the reactor without any addition of steam. The tests were carried out at constant pressure and Weight Hourly Space Velocity (WHSV) values, at increasing temperatures (Table 2.3).

Table 2.3. Experimental conditions used for the Dry Reforming reaction tests.

Test	T (°C)	P (bar)	WHSV (ml/(h·g <sub>cat</sub> ))
1	700	5	25,000
2	800	5	25,000
3	900	5	25,000

The tests carried out in the S/DR conditions were performed feeding an equimolar mixture of CH<sub>4</sub> and CO<sub>2</sub> at constant WHSV values, decreasing the temperature from 900 °C to 700 °C and changing the Steam to CH<sub>4</sub> molar ratio (S/CH<sub>4</sub>) to evaluate how the amount of water affects the catalytic performance and the composition of the exit syngas. After the full cycle of tests, a test in the same conditions than the first one was performed to evaluate the catalyst deactivation in terms of CH<sub>4</sub> and CO<sub>2</sub> conversion (Table 2.4).

Table 2.4. Experimental conditions for the Steam/Dry Reforming reaction tests.

Test	T (°C)	S/CH <sub>4</sub> (mol/mol)	P (bar)	WHSV (ml/(h·g <sub>cat</sub> ))
1	900	2.0	5	50,000
2	900	1.0	5	50,000
3	900	0.5	5	50,000
4	800	2.0	5	50,000
5	800	1.0	5	50,000
6	800	0.5	5	50,000
7	700	2.0	5	50,000
deact.	900	2.0	5	50,000

### Water gas shift tests

The activity tests simulated the industrial conditions and the reagent streams reproduced the exit syngas from the S/DR plant. The study was mainly focused on the optimization of the S/DG ratio to obtain the highest yield of H<sub>2</sub> together with the smaller concentration of CO in the exit stream for its further application in fuel cells. Experimental conditions used were different for MTS (Table 2.5) and HTS (Table 2.6). As before, the deactivation of the catalyst in terms of CO conversion was evaluated repeating a test in the same conditions than the second one, after the end of the cycle.

Table 2.5. Experimental conditions for the MTS process tests.

Test	T (°C)	P (bar)	S/DG (mol/mol)	WHSV (ml/h·g <sub>cat</sub> )
1	250	15	0.55	16,400
2	250	15	0.55	8,200
3	300	15	0.55	16,400
4	300	15	0.55	8,200
5	350	15	0.55	16,400
6	350	15	0.55	8,200
deact.	250	15	0.55	8,200

Table 2.6. Experimental conditions for the HTS process tests.

Test	T (°C)	P (bar)	S/DG (mol/mol)	WHSV (ml/h·g <sub>cat</sub> )
1	350	15	0.55 or 0.29	16,400
2	350	15	0.55 or 0.29	8,200
3	350	15	0.55 or 0.29	4,100
4	400	15	0.55 or 0.29	8,200
5	400	15	0.55 or 0.29	4,100
6	450	15	0.55 or 0.29	8,200
7	450	15	0.55 or 0.29	4,100
deact.	350	15	0.55 or 0.29	8,200

### 2.3.5 Data elaboration

The data obtained from the GC analyses showing the dry gas (DG) composition during the reaction, together with the measured inlet and outlet stream flows, allowed to calculate the conversions ( $\chi$ ), the H<sub>2</sub>/CO molar ratio and the mass balance (C<sub>OUT/IN</sub>) values, using the following equations:

#### CH<sub>4</sub>, CO<sub>2</sub>, CO conversion

$$\chi_{CH_4, CO_2, CO} = \frac{[CH_4]^{IN} - [CH_4]^{OUT}}{[CH_4]^{IN}} \cdot 100 = \left( 1 - \frac{\%CH_4^{OUT} \cdot F_{DG}^{OUT}}{\%CH_4^{IN}} \right) \cdot 100$$

#### H<sub>2</sub>/CO molar ratio

$$\frac{H_2}{CO} = \frac{\%H_2^{OUT}}{\%CO^{OUT}}$$

#### Carbon balance

$$\begin{aligned} C_{OUT/IN} &= \frac{[CH_4]^{OUT} + [CO_2]^{OUT} + [CO]^{OUT}}{[CH_4]^{IN} + [CO_2]^{IN} + [CO]^{IN}} \cdot 100 \\ &= \left( \frac{\%CH_4^{OUT} + \%CO_2^{OUT} + \%CO^{OUT}}{\%CH_4^{IN} + \%CO_2^{IN} + \%CO^{IN}} \cdot \frac{F_{DG}^{OUT}}{F_{DG}^{IN}} \right) \cdot 100 \end{aligned}$$

#### Nomenclature

$\%CH_4^{IN}$  = inlet percentage of CH<sub>4</sub>       $\%CH_4^{OUT}$  = outlet percentage of CH<sub>4</sub>

$\%CO_2^{IN}$  = inlet percentage of CO<sub>2</sub>       $\%CO_2^{OUT}$  = outlet percentage of CO<sub>2</sub>

$\%CO^{IN}$  = inlet percentage of CO       $\%CO^{OUT}$  = outlet percentage of CO

$F_{DG}^{IN}$  = inlet percentage of dry gas       $F_{DG}^{OUT}$  = outlet percentage of dry gas

### References

1. F. Cavani, F. Trifirò, A. Vaccari, Catal. Today, 11 (1991) 173-302
2. R. Salomao, L.M. Milena, M.H. Wakamatsu, V.C. Pandolfelli, Ceramics International, 37 (2011) 3063-3070

### 3. Results and discussion

#### 3.1.1 Dry Reforming of clean biogas (CB)

The feasibility of the CO<sub>2</sub> reforming (Dry Reforming or DR) of CB using Ni-based catalysts was investigated with the aim to point out the main drawbacks of the reaction. Special attention was paid to the parameters that affect carbon formation during the process, studying the effect of the reaction temperature on the catalyst activity and stability. The influence of a small amount of Rh (0.5 wt.%) to boost the catalyst activity and stability was deeply investigated, focusing the attention on the role of Ni-Rh interaction.

In the early stages of the work, the feasibility of the DR of CB was studied. The first tests were carried out using a Ni-based catalyst (Ni = 10 wt.%), and with a M<sup>2+</sup>/M<sup>3+</sup> ratio of 3. The Hydrotalcite-type (HT) structure of the dried precipitate evolves in a mixture of oxides such as evidenced by XRD analyses (Fig. 3.1). The 10NiMgAl3 catalyst after calcination is composed mainly of MgO and a spinel phase containing Mg and Al. The peaks related to the Ni-containing phases overlapped with those of MgO and MgAl<sub>2</sub>O<sub>4</sub> doing difficult to identify the NiAl<sub>2</sub>O<sub>4</sub> and NiO phases.

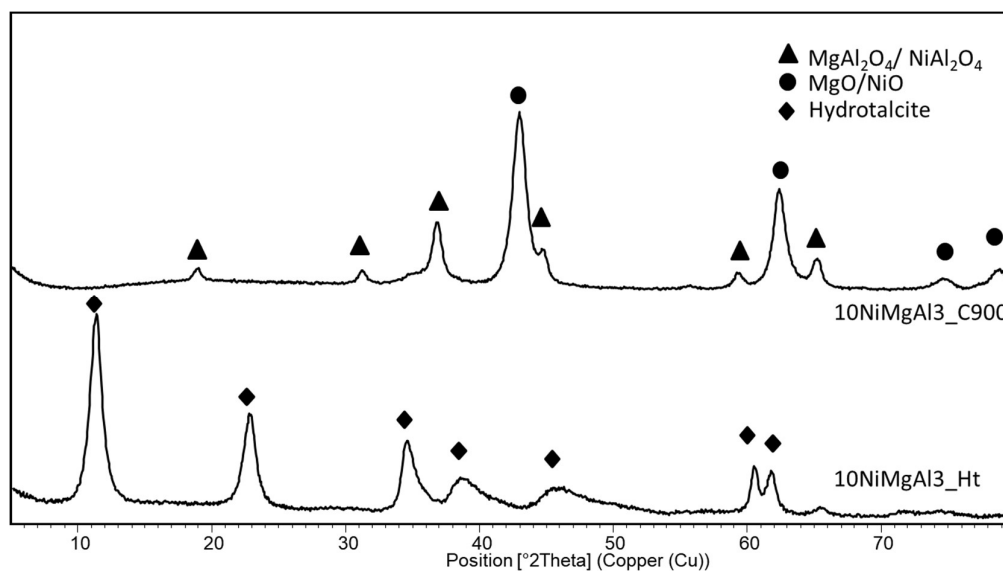


Figure 3.1. XRD patterns of the 10NiMgAl3 catalyst dried (Ht) and calcined at 900 °C.

The 10NiMgAl3 catalyst was tested at increasing temperatures while keeping constant the WHSV value and the operating pressure (5 bar). In figure 3.2 the catalytic activities for the tests at 700°C and 800°C are reported.

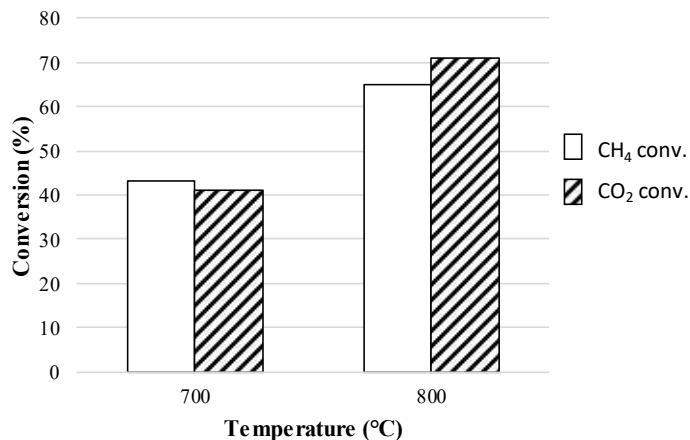


Figure 3.2. CH<sub>4</sub> and CO<sub>2</sub> conversions for the 10NiMgAl<sub>3</sub> catalyst in the DR conditions.

How foreseeable by the reaction thermodynamic, the CB conversion increased with the temperature. If at 700°C the CO<sub>2</sub> and CH<sub>4</sub> conversion values are comparable and in line with the reaction stoichiometry, that of CO<sub>2</sub> at 800°C was higher than the conversion of CH<sub>4</sub>, due to the Reverse Water Gas Shift (RWGS) reaction that may occur in these reaction conditions. Best results in terms of CH<sub>4</sub> and especially CO<sub>2</sub> conversion values were obtained promoting the catalyst with 0.5 wt.% of Rh regardless the temperature investigated (Fig. 3.3).

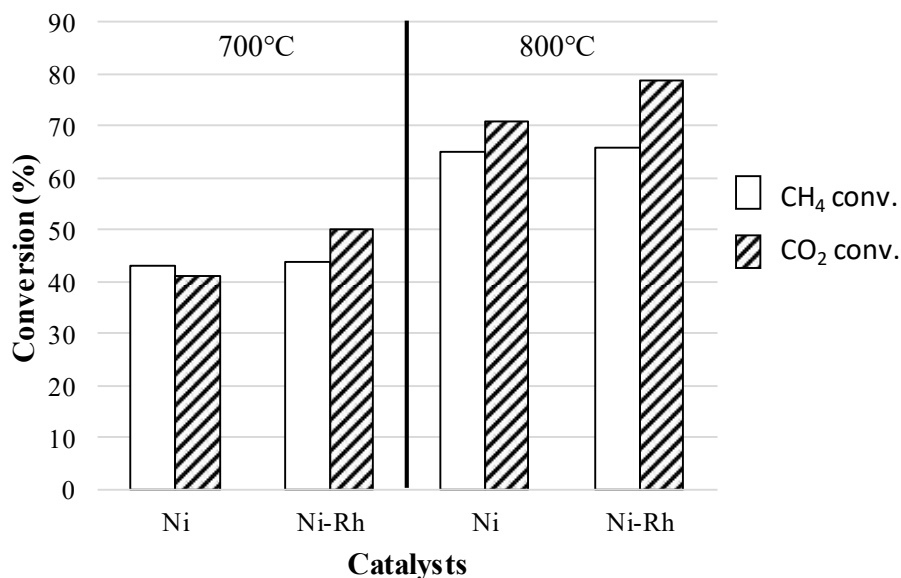


Figure 3.3. CH<sub>4</sub> and CO<sub>2</sub> conversions for the 10NiMgAl<sub>3</sub> and 10 NiMgAl<sub>3</sub>\_Rh05 catalysts in the DR conditions.

Despite the good catalytic activities, both the catalysts suffered from a strong carbon formation at these temperatures. After a few hours of time-on-stream, an increasing pressure drop in the reactor due to the breakage of the catalyst granules was observed and the tests were stopped. The presence of carbon was evidenced also by the Raman spectra collected on the two spent catalysts (Fig. 3.4 and 3.5) in which it is possible to observe three main bands associated to carbon-related species on the surface.

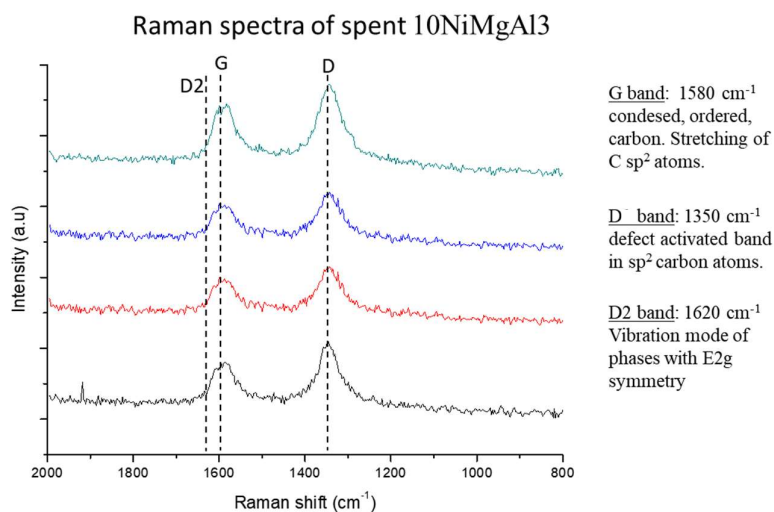


Figure 3.4. Raman spectra collected in different zones of the 10NiMgAl3 catalyst after the test at 800°C.

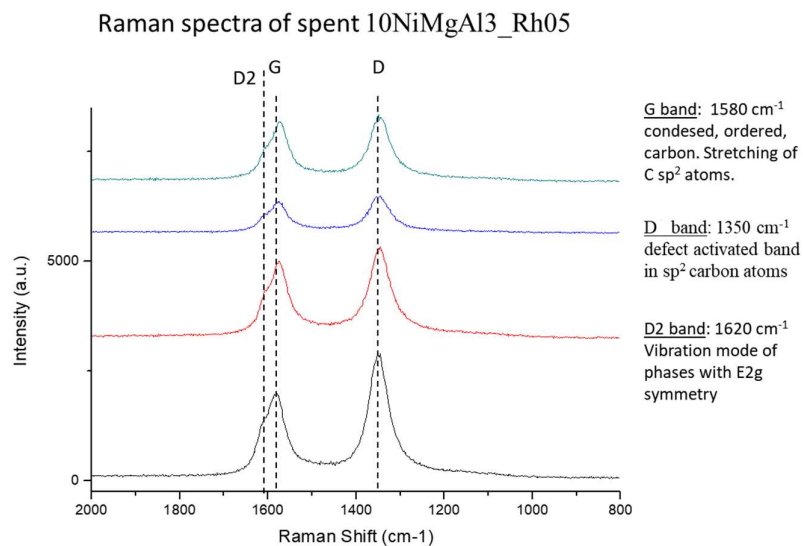


Figure 3.5. Raman spectra collected in different zones of the 10NiMgAl3\_Rh05 catalyst after the test at 800°C.

All the bands are typical of sp<sup>2</sup> hybridized carbon [1] (ordered and defective graphene phases) probably associated to the presence of carbon nanotubes formed by the

Boudouard reaction in the CO-rich reaction environment. The presence of crystalline carbon was confirmed by the XRD analysis of the two spent catalysts (Fig. 3.6) that showed an intense characteristic peak at  $2\theta = 26.3^\circ$ . After reaction a peak attributable to the presence of metallic Ni was also detected for both samples, indicating the formation of large and not well-dispersed particles of active phase during the reduction/reaction step.

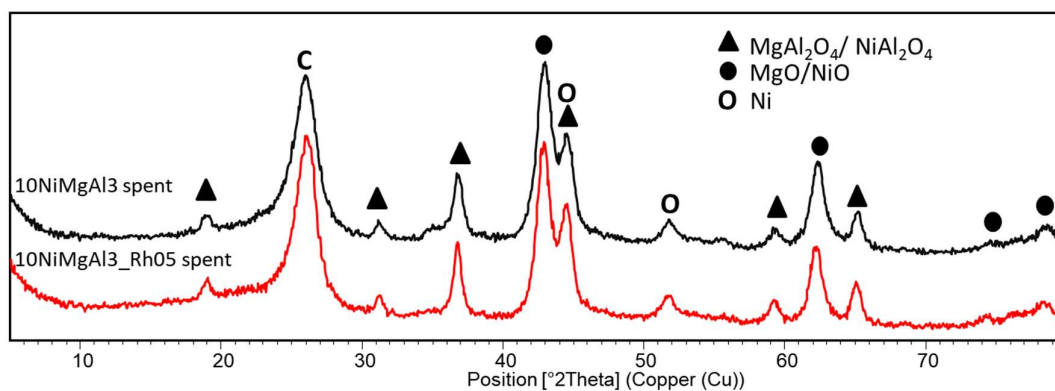


Figure 3.6. XRD patterns of the 10NiMgAl3 and 10NiMgAl3\_Rh05 catalysts after reaction at 800°C.

One possible solution to overcome/reduce the carbon formation rate, improving the stability, in the DR process is to increase the reaction temperature, treating unfairly the Boudouard reaction. For this reason, the two catalysts were tested at 900°C monitoring the activity for 5 h. No increase of pressure drop in the reactor was observed, revealing an improved stability of the catalysts at this temperature. The activity of the 10NiMgAl3 catalyst remained stable, without any evidence of deactivation (Fig. 3.7).

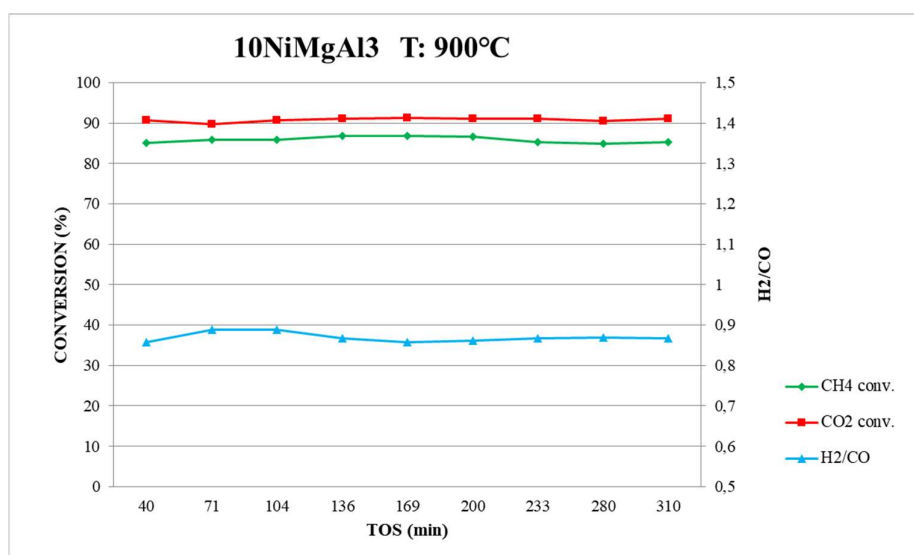


Figure 3.7. Activity of 10NiMgAl3 catalyst at 900°C in the DR conditions along 5 h.

Moreover, good catalytic performances were achieved, and the CO<sub>2</sub> conversion was higher than that of CH<sub>4</sub>. Increasing the reaction temperature, the RWGS reaction was favoured as confirmed by the H<sub>2</sub>/CO value of the outlet stream, stable for all the 5 h to values lower than 1 ( $\approx 0.88$ ). The addition of 0.5 wt.% of Rh increased the conversion of the CB (CH<sub>4</sub> conversion  $\approx 90\%$ ), although the RWGS reaction was not suppressed giving rise to a syngas with a H<sub>2</sub>/CO value around 0.91 (Fig. 3.8).

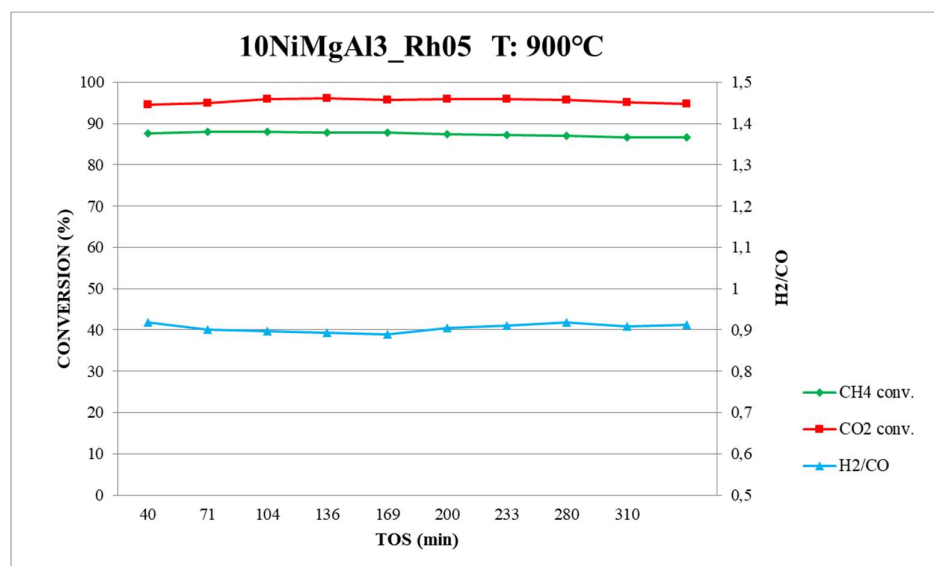


Figure 3.8. Activity of 10NiMgAl<sub>3</sub>\_Rh05 catalyst at 900°C in the DR conditions along 5 h.

An explanation of the improved activity of the catalyst promoted by Rh may be obtained from the reduction profiles obtained by H<sub>2</sub>-TPR analysis on the two calcined catalysts (Fig. 3.9). Three main effects may be attributed to the presence of Rh in the catalyst formulation: i) a “strong” decrease of the Ni<sup>2+</sup> reduction temperature that shifted, for the un-doped sample, from 900°C to 895°C; ii) a symmetrical shape of the Ni<sup>2+</sup> reduction profile when Rh is present; iii) a very broad peak of Ni<sup>2+</sup> reduction for the un-doped sample, evidencing a low degree of reducibility with the formation of large and not well distributed Ni<sup>0</sup> particles. These results evidence that the presence of Rh favoured the reduction of Ni<sup>2+</sup> ions, with the formation of more active metal particles on the catalyst surface. The peak at 467 °C observed for the 10NiMgAl<sub>3</sub>\_Rh05 catalyst can be associated to the reduction of Rh<sup>3+</sup> containing species. The TEM images (Fig. 3.10) of the two catalysts after reduction allowed to determine the distribution and size of the active metal particles before reaction. The two statistical distributions showed that the addition of a 0.5 wt.% of Rh is sufficient to give rise to smaller and better dispersed metal particles on the catalyst surface.

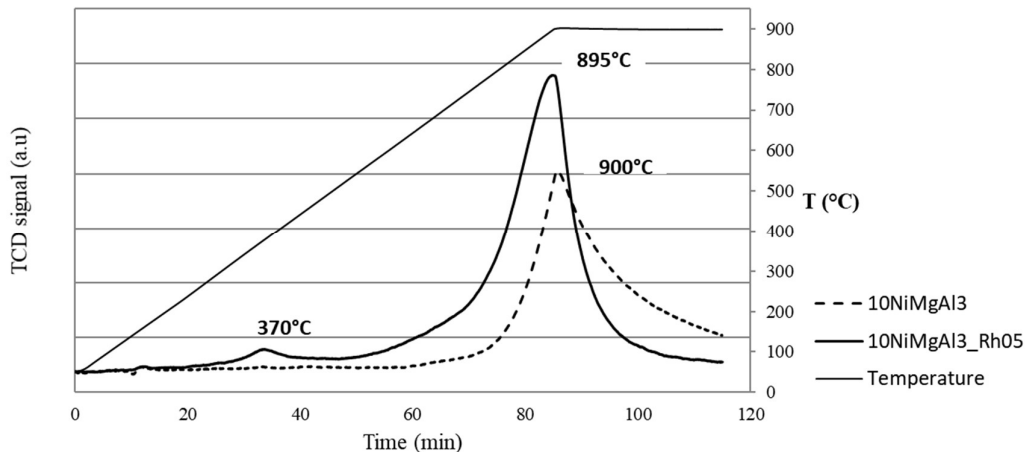


Figure 3.9. H<sub>2</sub>-TPR profiles for the calcined 10NiMgAl<sub>3</sub> and 10NiMgAl<sub>3</sub>\_Rh05 catalysts.

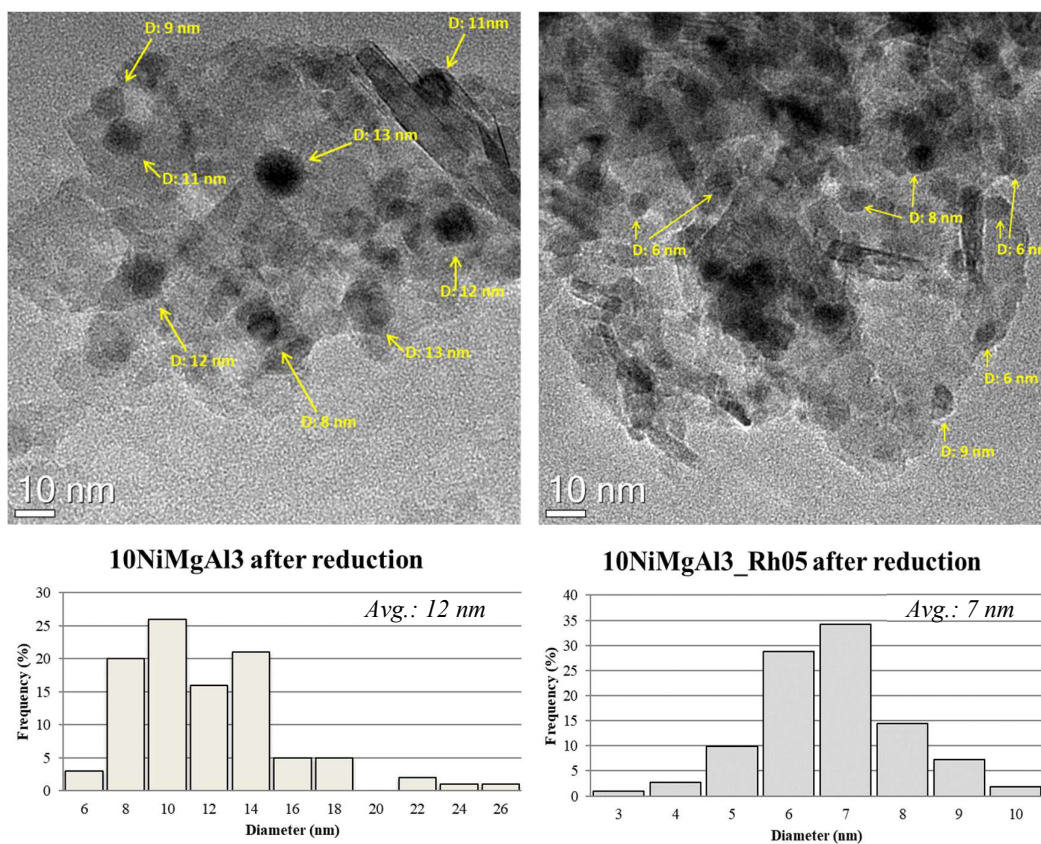


Figure 3.10. TEM images and respective statistical distributions of the metal particles for the undoped 10NiMgAl<sub>3</sub> (on the left) and doped 10NiMgAl<sub>3</sub>\_Rh05 (on the right) catalysts after reduction.

The 10NiMgAl<sub>3</sub> catalyst showed a significant presence of metal particles larger than 14 nm, while the average diameter was reduced of  $\approx 42\%$  when Rh was added to the formulation, showing a distribution centred around a value of 7 nm without particles

larger than 10 nm, pointing out that both reducibility and activity of the catalyst were driven by the active phase dispersion. The analyses on the two spent catalysts revealed relevant differences in terms of resistance to carbon deposition. As it is possible to observe in the Raman and TG analyses of the 10NiMgAl3 catalyst after reaction (Fig. 3.11), notwithstanding the good results observed in terms of stability, the sample showed the presence of a significant amount of carbon deposited during the reaction. The Raman spectra showed evidences of  $sp^2$  carbon, with an increased intensity of the ordered carbon (G band:  $1580\text{ cm}^{-1}$ ) in comparison to the results obtained at  $800\text{ }^\circ\text{C}$  (Fig. 3.4 and 3.5), while the TG analysis revealed a mass loss of  $\approx 25\%$  between  $425$  and  $700\text{ }^\circ\text{C}$  attributable to the oxidation of carbonaceous species, as confirmed by the presence of  $\text{CO}_2$  in the exit gas stream.

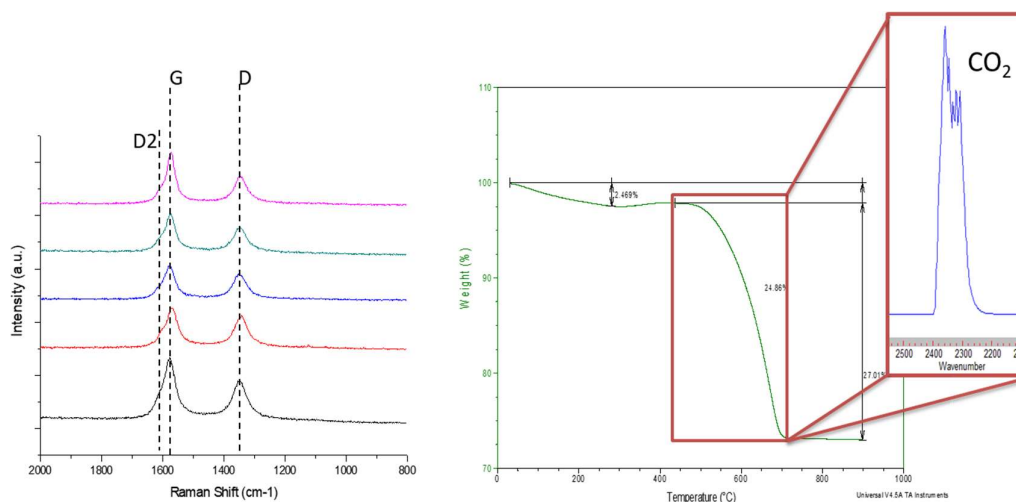


Figure 3.11. Raman spectra (on the left) and TG analysis (on the right) conducted on the 10NiMgAl3 spent catalyst after the test at  $900\text{ }^\circ\text{C}$ . Inside the red square, IR spectrum of the gases released during the TG analysis.

On the contrary, the presence of Rh in the 10NiMgAl3\_Rh05 catalyst improved the resistance to carbon formation during the DR process and the Raman spectra (Fig.3.12, on the left) of the spent sample showed a small presence of carbonaceous species, quantified by the TGA as  $\approx 3\%$  of the total weight, with a reduction of carbon deposition of about  $88\%$ .

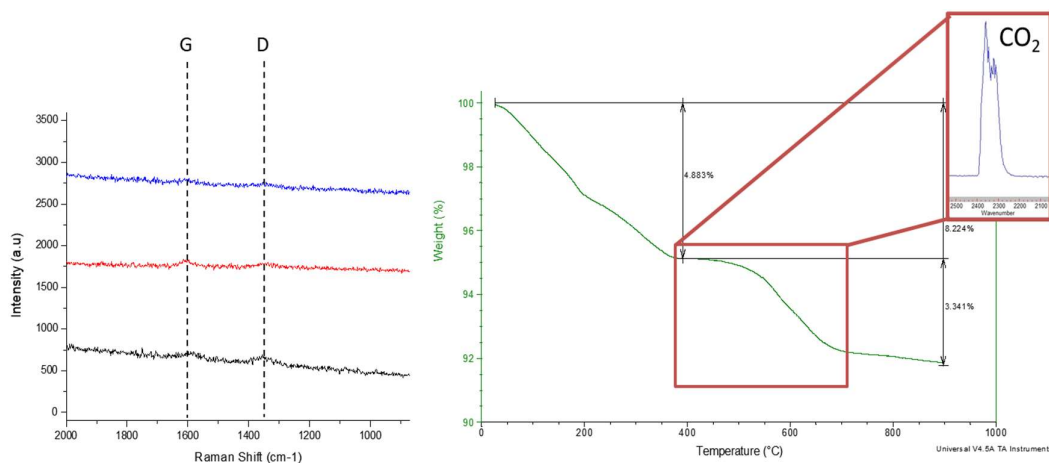


Figure 3.12. Raman spectra (on the left) and TG analysis (on the right) conducted on the 10NiMgAl<sub>3</sub>\_Rh05 spent catalyst after the test at 900 °C. Inside the red square, IR spectrum of the gases released during the TG analysis.

The XRD patterns of the two spent catalysts confirmed these observations; in figure 3.13 the peak of the crystallized carbon was present only in the 10NiMgAl<sub>3</sub> catalyst, while the other crystalline phases were comparable without any real difference in terms of crystallinity between the two samples after reaction.

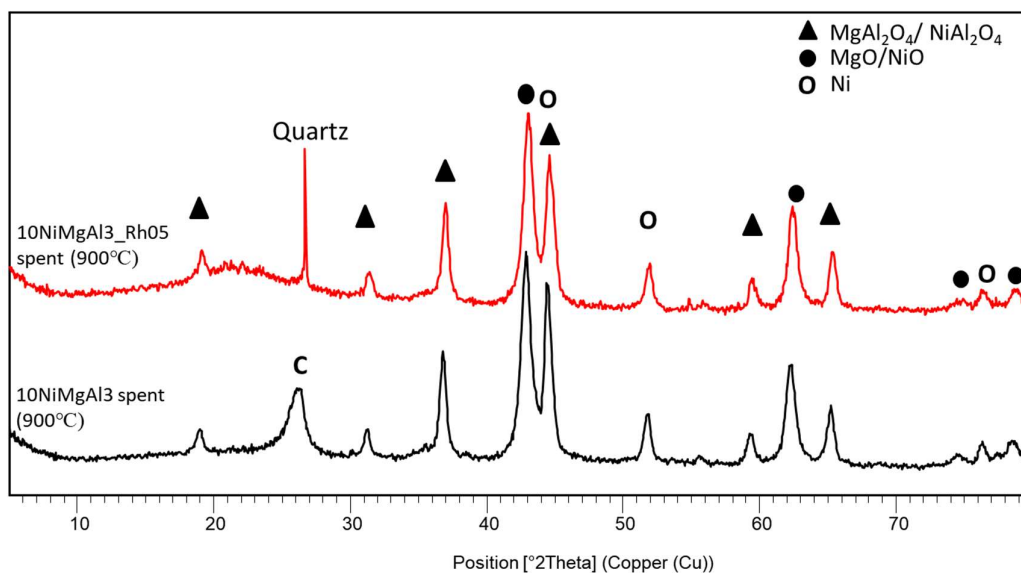


Figure 3.13. XRD patterns of the 10NiMgAl<sub>3</sub> and 10NiMgAl<sub>3</sub>\_Rh05 catalysts after reaction at 900 °C (The peak of quartz is due to the presence of inert particles in the sample).

From the TEM observations of these two samples it was possible to find the presence of long and well distributed carbon nanotubes for the Rh-free catalyst, together with the formation of encapsulating graphitic carbon around some Ni<sup>0</sup> particles (Fig. 3.14).

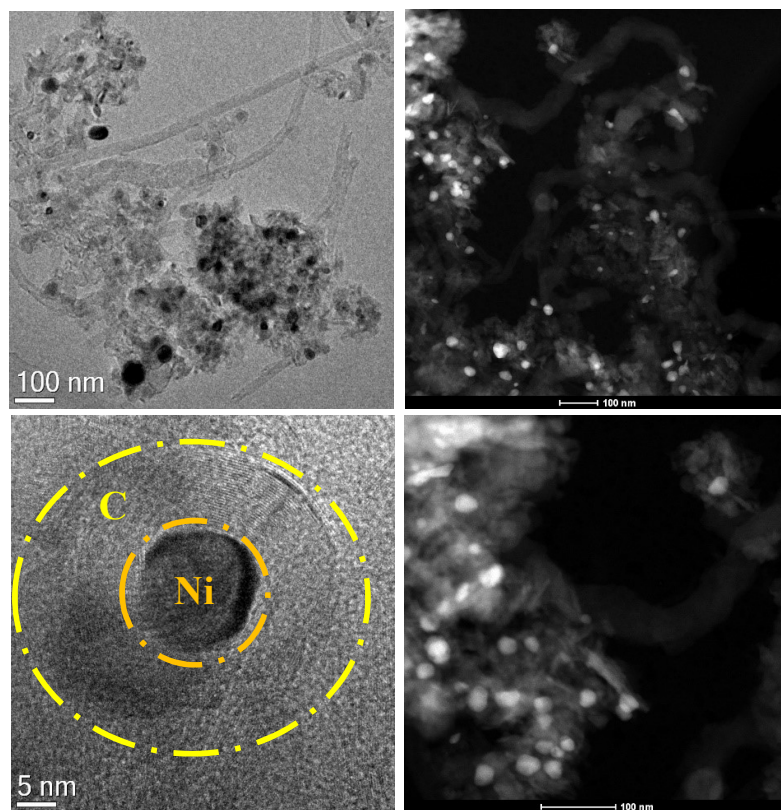


Figure 3.14. TEM (left) and STEM-HAADF images (right) of the 10NiMgAl<sub>3</sub> catalyst after reaction at 900 °C.

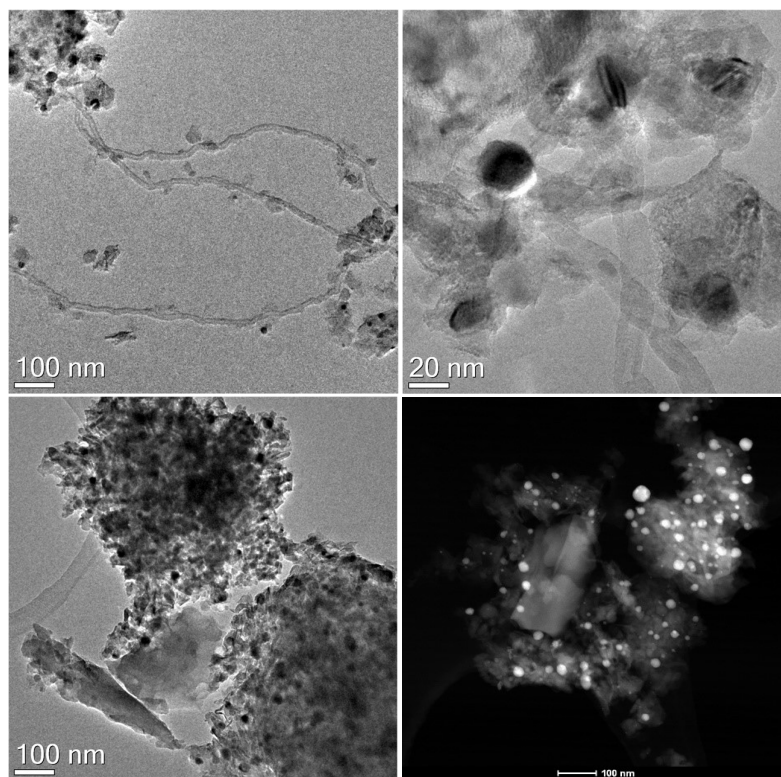


Figure 3.15. TEM (left) and STEM-HAADF images (right) of the 10NiMgAl<sub>3</sub>\_Rh05 catalyst after reaction at 900 °C.

Although the detachment of some Ni<sup>0</sup> particles from the catalytic support due to the generation of carbon nanotubes was also observed for the 10NiMgAl\_Rh05 spent catalyst (Fig. 3.15), their presence was small, not homogeneous along the sample and without evidences of encapsulating carbon. The harsh reaction conditions and the high temperature promoted the sintering of the active phase for both the catalysts with a distribution of the metal particles (Fig. 3.16 and 3.17) that showed a critical increase of the diameter to values that evidenced also the presence of particles larger than 60 nm.

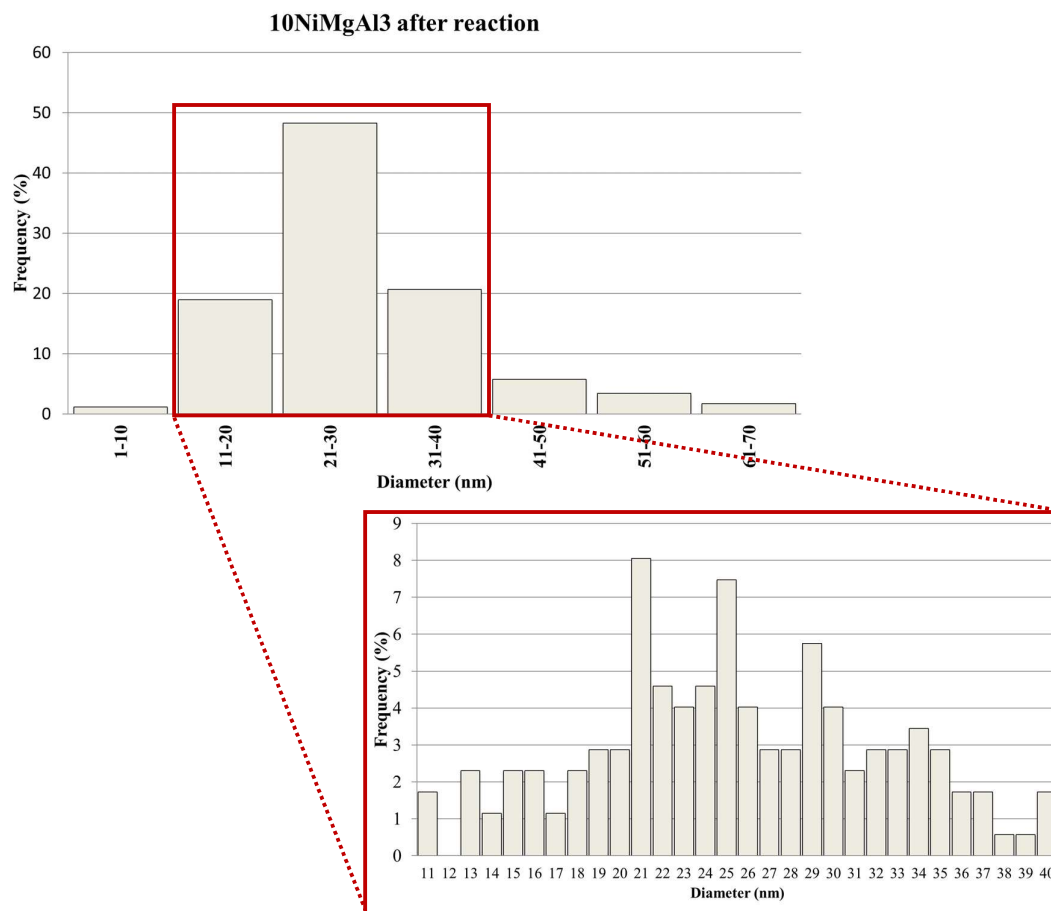


Figure 3.16. Distribution of the metal particles for the 10NiMgAl3 catalyst after reaction at 900 °C in DR conditions.

The metal particles distribution of the 10NiMgAl3\_Rh05 (Fig. 3.17) was wider but exhibited at the same time a higher number of particles in the range 1-30 nm. These sintering phenomena caused a decreased in the metallic surface area, leading to a reduction of the reaction endothermicity, flattening the thermal profile of the catalytic bed during the 5 h test (Fig.3.17).

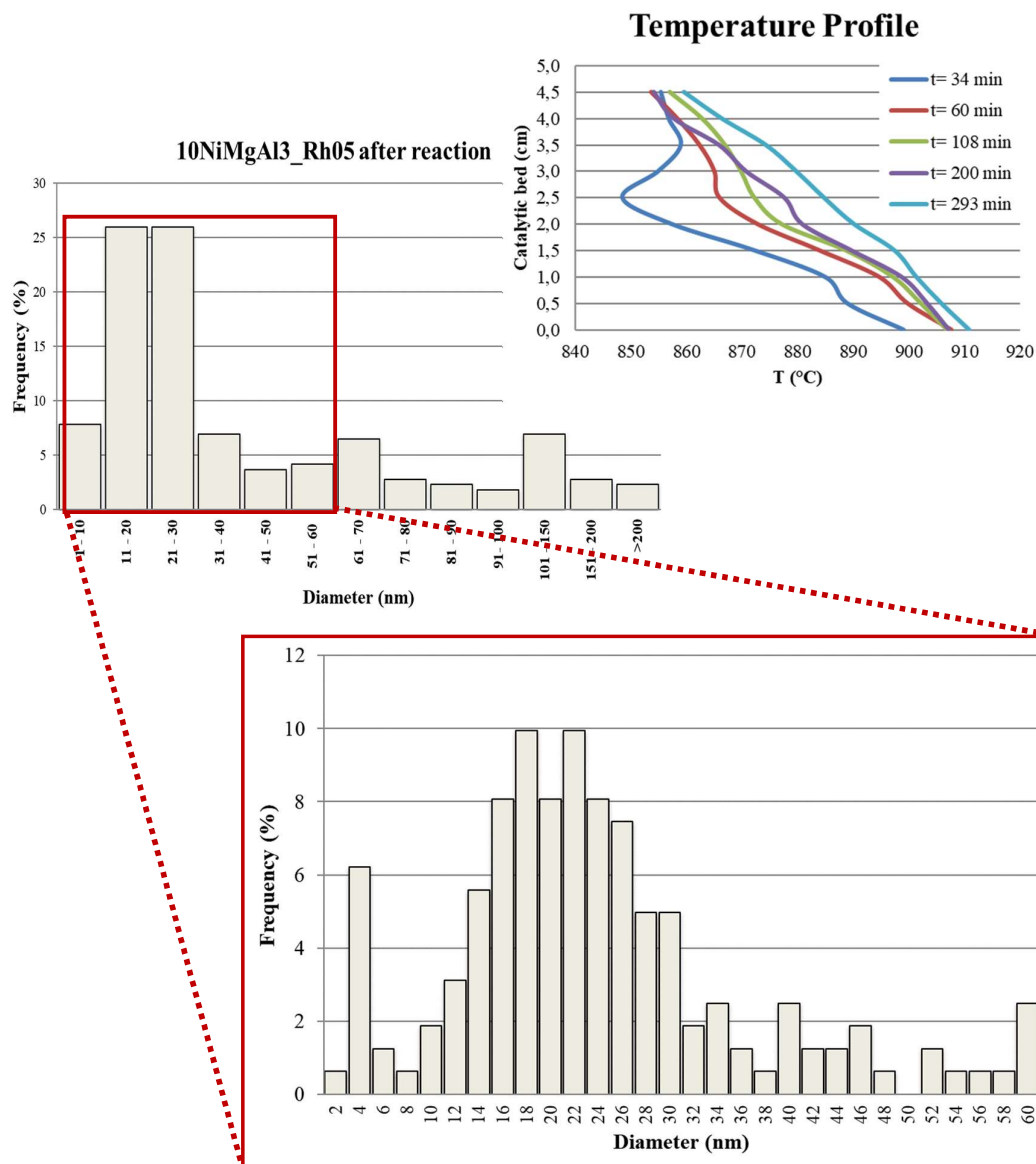
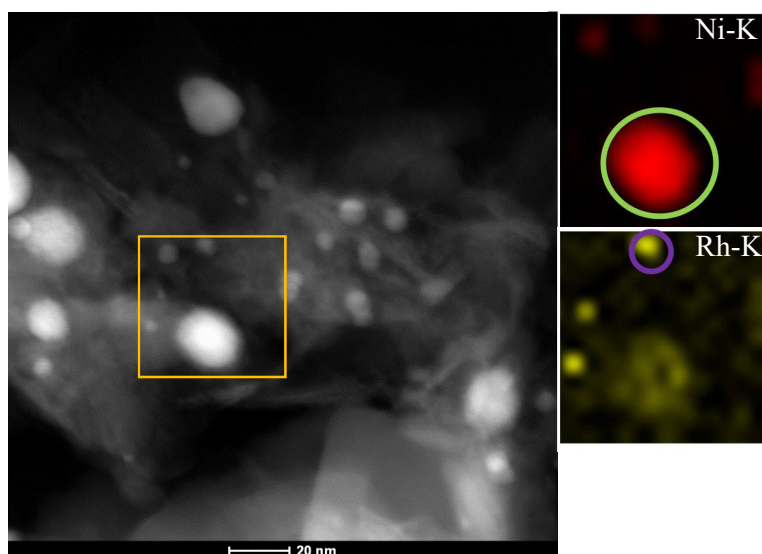


Figure 3.17. Distribution of the metal particles for the 10NiMgAl<sub>3</sub>\_Rh05 catalyst after reaction at 900 °C in DR conditions and thermal profiles of the catalytic bed at different time-on-stream values (right).

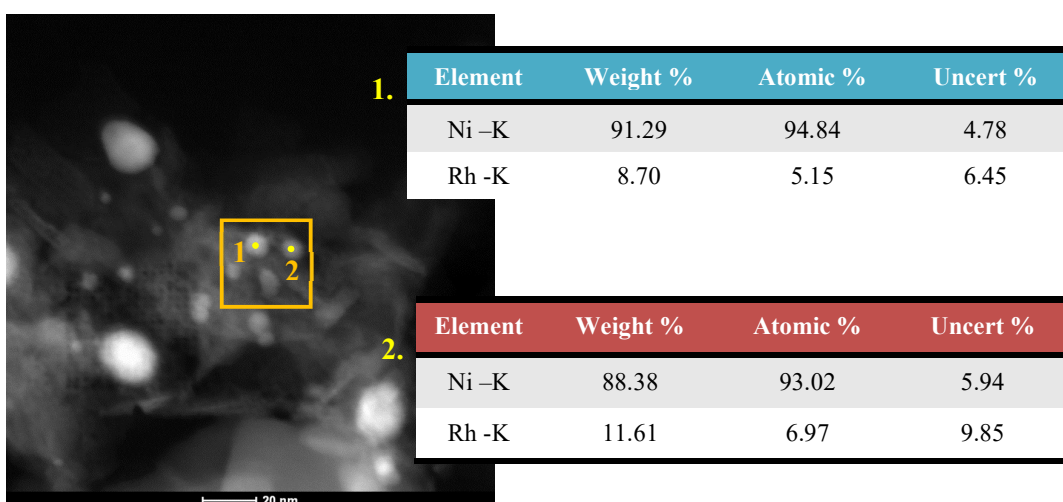
From the EDX analyses carried out during the TEM observations it was possible to further investigate the interaction between Ni and Rh. In figure 3.18 the EDX maps of a zone of the catalyst that contains reduced particles with different diameter is shown; the metal particles inside the yellow square were analysed to quantify the concentration of the two metals. The composition was very variable, but the smaller particles were mainly made of Rh. The concentration of this latter lowered by increasing the particle size, reaching a value around zero for the largest particles mainly constituted of Ni, while the formation of a Ni-Rh alloy was evidenced for the particles with a size of 5-7 nm ca.



Element	Weight %	Atomic %	Uncert %
Ni -K	100.00	100.00	3.17
Rh -K	///	///	///

Element	Weight %	Atomic %	Uncert %
Ni -K	65.09	76.57	5.41
Rh -K	34.90	23.42	11.30

Figure 3.18. STEM-HAADF image and EDX maps of some metal particles of the 10NiMgAl<sub>3</sub>\_Rh05 spent catalysts, under the figures the compositional analyses are reported.



Element	Weight %	Atomic %	Uncert %
Ni -K	91.29	94.84	4.78
Rh -K	8.70	5.15	6.45

Element	Weight %	Atomic %	Uncert %
Ni -K	88.38	93.02	5.94
Rh -K	11.61	6.97	9.85

Figure 3.19. STEM-HAADF image and EDX compositional analyses of two metal particles with the same diameter on the surface of the 10NiMgAl<sub>3</sub>\_Rh05 spent catalyst.

It was also found that the alloy composition for two particles with the same diameter (Fig.3.19) was comparable, pointing out that the Rh concentration in the alloy seems to determine the active phase dispersion and size, leading to smaller and more stable nanoparticles. A confirmation of this hypothesis may be found studying the compositional particle profiles as a function of their size; in figure 3.20, the compositions of the Ni-Rh alloy in the centre of the particles as a function of their diameter is reported. The Rh content varied from a value of 2% (atomic percent, green table) in the 25 nm particle to a value around 66% (atomic percent, blue table) in the smaller particles (diameter = 3 nm), showing that the formation of the alloy with different metal ratio influenced the properties and the distribution of the active phase.

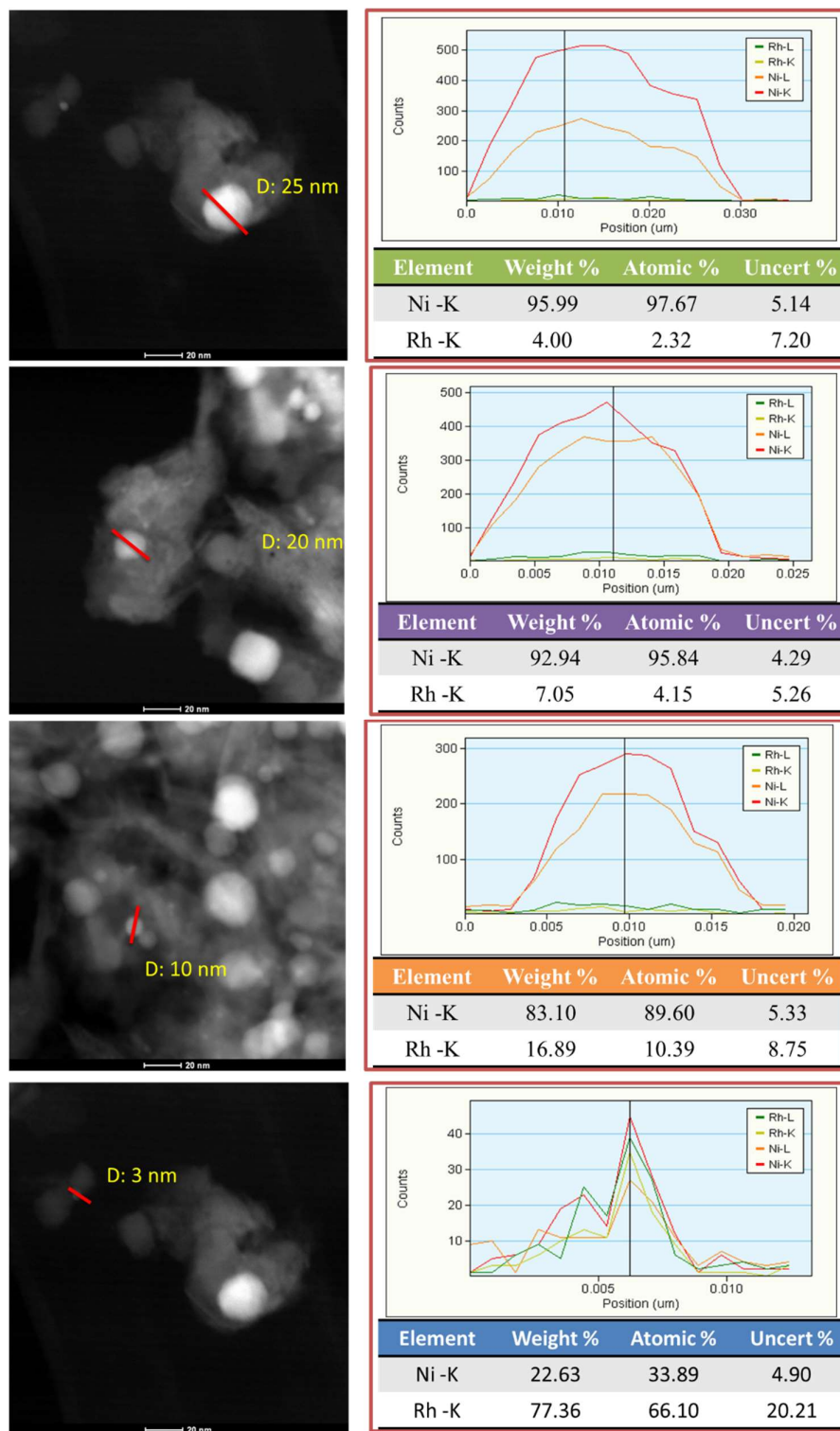


Figure 3.20. STEM-HAADF images and EDX compositional profiles of some nanoparticles as a function of their diameter. The Tables illustrate the Ni-Rh alloy composition in the centre of the particles.

### 3.1.2 Preliminary conclusions

Through the Dry Reforming of the clean biogas it is possible to valorise the CO<sub>2</sub> content of the feed producing a syngas with a H<sub>2</sub>/CO ratio suitable for further processes. Although the two Ni-based catalysts showed good catalytic activity in the reaction conditions, relevant drawback associated to the DR process were also detected. The reaction temperature is a key parameter to decrease the strong carbon deposition on the surface of the catalysts, avoiding at 900 °C the dangerous increase of the pressure drop inside the reactor. The addition of 0.5 wt.% of Rh to the catalyst promotes the reducibility of the Ni particles, improving the distribution of the active phase after reduction and increasing the catalyst activity and stability. The presence of the noble metal significantly reduces the carbon formation and the detachment of the nanoparticles from the support, although it does not suppress the sintering of the active phase. The improved properties of the 10NiMgAl<sub>3</sub>\_Rh<sub>05</sub> catalyst are attributable to the formation of a Ni-Rh alloy that, although present in variable compositions in the different metal particles, controls the size of the active phase and, consequently, its activity in the DR reaction.

### 3.2.1 Addition of steam: Steam/Dry Reforming reaction (S/DR)

One of the possible solutions to overcome the main drawbacks associated to the DR process is the addition of an oxidant to the reaction feed. Pure oxygen, air or steam are the most feasible reactants to be used and their presence at high temperatures, can considerably decrease the deposition of carbon on the catalyst surface during the reaction, increasing the H<sub>2</sub>/CO molar ratio in the outlet synthesis gas for more exploitable values [2]. The introduction of steam, in different amounts, as co-reactant was investigated with the aim to reduce the carbon deposition and increase the H<sub>2</sub>/CO ratio of the outlet stream. The two Ni-based catalysts (10NiMgAl3 and 10NiMgAl3\_Rh05) were tested in the S/DR conditions, changing the reaction parameters, evaluating the effect of Rh on the catalyst properties and pointing out the main differences between the two reforming (Steam and Dry, SR and DR) process.

The influence of steam was at first tested on the 10NiMgAl3 catalyst. In this case the catalytic performances were evaluated at 5 bar, working at decreasing temperatures (from 900 to 700 °C), changing the value of the Steam/CH<sub>4</sub> ratio (S/CH<sub>4</sub>) of the feed (2, 1, 0.5 v/v) but maintaining a constant WHSV value of 50,000 ml/(h · g<sub>CAT</sub>). The first results obtained in the combined process are shown in figure 3.21.

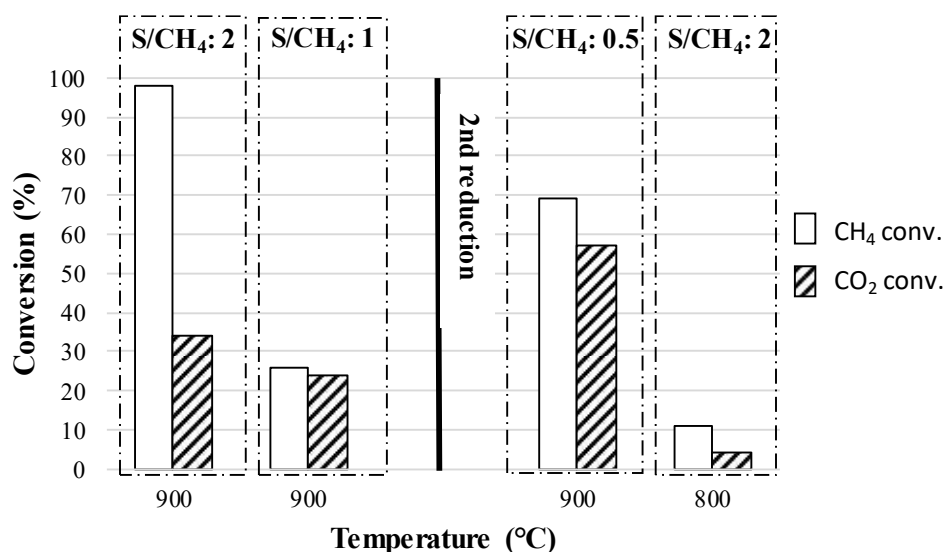


Figure 3.21. CH<sub>4</sub> and CO<sub>2</sub> conversion values for the 10NiMgAl3 catalyst tested in the S/DR conditions

The presence of steam in the first test conducted at 900 °C (S/CH<sub>4</sub> = 2) led to an increase in the CH<sub>4</sub> conversion (≈ 98 %) but the CO<sub>2</sub> conversion was reduced (≈ 33 %) due to the

occurrence of the SR reaction. After two hours of test, the S/CH<sub>4</sub> ratio was decreased to a value of 1 and a strong deactivation of the catalyst in terms of CH<sub>4</sub> and CO<sub>2</sub> conversion was observed (losses in activity: CH<sub>4</sub> conversion = -75 %, CO<sub>2</sub> conversion = -33 %). The behaviour was attributed to the instability of the active phase in the reaction environment, and for this reason the catalyst was subjected to a further reduction. After this step, the catalytic activity was recovered in the third test (T = 900 °C, S/CH<sub>4</sub> = 0.5) in which the CB conversions were stable over 2 h. However, after a further change of the reaction conditions (4<sup>th</sup> test, T = 800 °C, S/CH<sub>4</sub> = 2), another dramatic drop of activity was observed, confirming the instability of this catalyst. The behaviour was attributed to the re-oxidation of the active phase due to the presence of steam at high temperatures. The greenish colour (characteristic of Ni<sup>2+</sup>-containing phases) of the catalyst granules after reaction (Fig. 3.22), strongly supported this hypothesis.



Figure 3.22. A picture of the 10NiMgAl3 catalyst after reaction in the S/DR conditions, with the presence of some green particles that evidence the existence of Ni<sup>2+</sup>-containing phases in the catalyst structure.

The XRD patterns of the spent catalyst (Fig. 3.23) showed the characteristic reflections of the MgO-NiO solid solution and MgAl<sub>2</sub>O<sub>4</sub>, without presence of Ni<sup>0</sup> and Ni<sub>2</sub>Al<sub>2</sub>O<sub>4</sub>, together with an increase of crystallinity, confirmed by a decrease of the BET specific surface area of -57 % (100 m<sup>2</sup>/g for the fresh catalyst → 43 m<sup>2</sup>/g for the spent catalyst). From the comparison of the XRD patterns of the fresh and spent catalyst, it was possible to observe only a weak shift of the reflection at 2θ of 43 ° ca. towards lower Bragg angles of the spent catalyst, suggesting that only a small amount of NiO was stably reduced during the S/DR reaction. Conversely, in the XRD pattern of the same catalysts after DR reaction (spectrum c), it was possible to detect the peak at 42.8° 2θ that perfectly matched

the MgO pattern, accompanied by the peak at  $44.4^\circ 2\theta$  characteristic of  $\text{Ni}^0$  that confirmed the complete segregation of the NiO from the periclase phase.

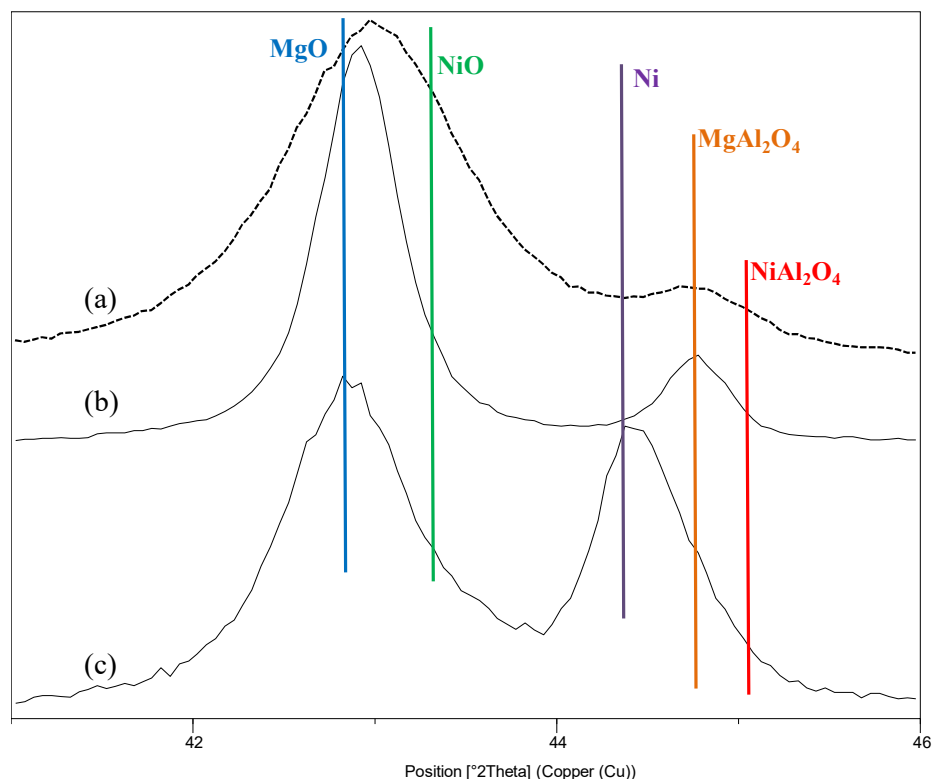


Figure 3.23. XRD patterns of the 10NiMgAl<sub>3</sub> catalyst after calcination (a), S/DR (b) and DR (c) reaction.

The 10NiMgAl<sub>3</sub>\_Rh05 catalyst, that showed the best performance in the DR was then also tested in the combined S/DR reaction. The results in terms of CH<sub>4</sub> and CO<sub>2</sub> conversion as a function of operating temperature and S/CH<sub>4</sub> volumetric ratio in the feed are showed in Figure 3.24. The addition of Rh stabilized the catalyst activity with no evidence of deactivation through all the cycle of tests. The CH<sub>4</sub> and CO<sub>2</sub> conversions were both favoured at high temperature, but the respective values varied considerably changing the reaction parameters. The S/CH<sub>4</sub> ratio is the main parameter that drive the reaction favouring one reaction over the other (SR vs. DR). The CH<sub>4</sub> conversion increased with the S/CH<sub>4</sub> value, i.e. in the conditions where SR is favoured, whereas the CO<sub>2</sub> conversion is promoted when the reaction environment is deficient in steam, with highest conversion values at 900 °C and a S/CH<sub>4</sub> ratio = 0.5.

The amount of steam also affected the H<sub>2</sub>/CO molar ratio in the produced synthesis gas, (Fig. 3.25), the value of which increased lowering the temperature at high S/CH<sub>4</sub> values, due to the predominance of the SR over the DR reaction. On the other hand, when the

S/CH<sub>4</sub> ratio was low, the H<sub>2</sub>/CO molar ratio decreased and was not significantly affected by the temperature, reaching values near 1 in the conditions promoting the CO<sub>2</sub> conversion.

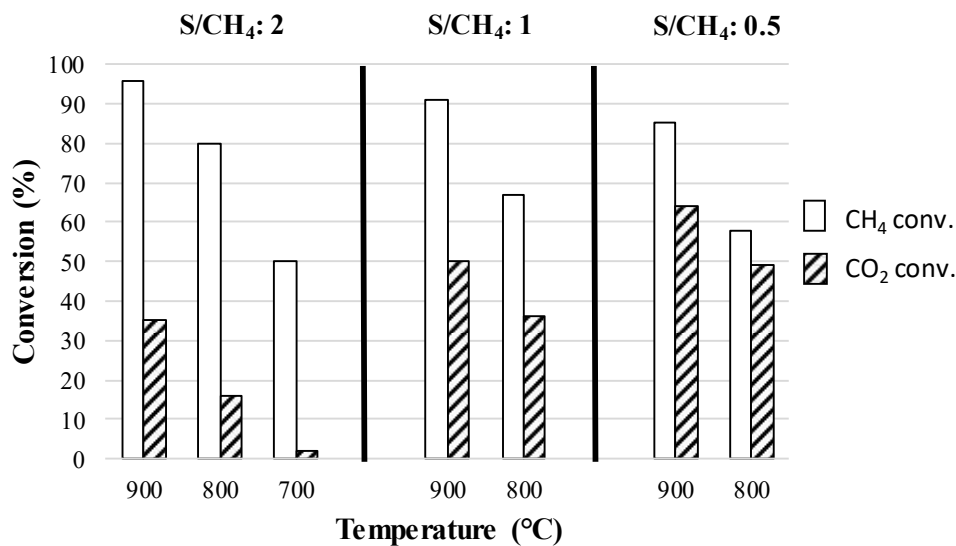


Figure 3.24. Catalytic activity of the 10NiMgAl<sub>3</sub>\_Rh05 catalyst in the S/DR tests.

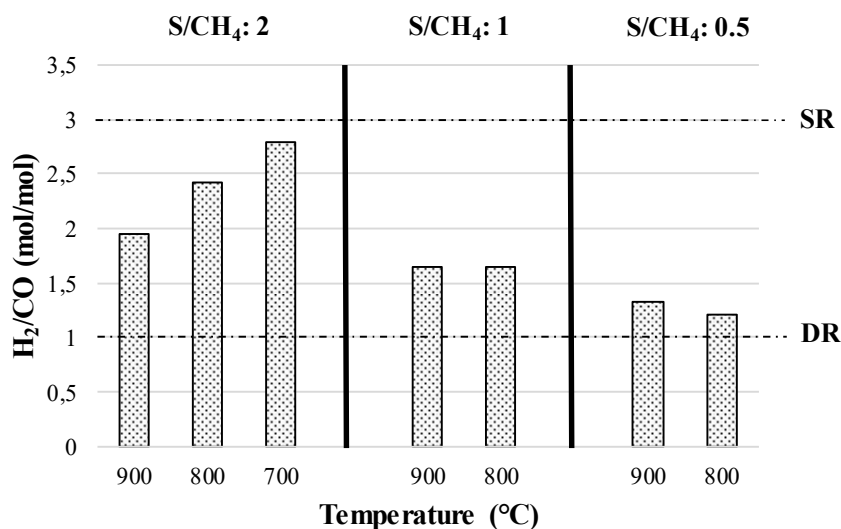


Figure 3.25. H<sub>2</sub>/CO molar ratio of the outlet synthesis gas for the 10NiMgAl<sub>3</sub>\_Rh05 catalyst in the S/DR tests.

The presence of Rh affected the distribution of the active phase after reaction. The diameter of the metal particles was between 2 and 9 nm and the distribution centred around 4 nm (Fig. 3.26), significantly lower than the value found after the DR (16 nm). The formation of big particles was avoided and the Raman (Fig. 3.27) and TG analyses

revealed a weak presence of carbon not homogeneously distributed, in an amount lower than 0.5 % of the total mass of the catalyst after reaction.

Even in these reaction conditions, the formation of the Ni-Rh alloy in the metal particles was observed. In this case, the alloy composition was more homogenous when varying the particle size and aggregates with different diameter showed only small differences in terms of Rh and Ni content (Fig. 3.28).

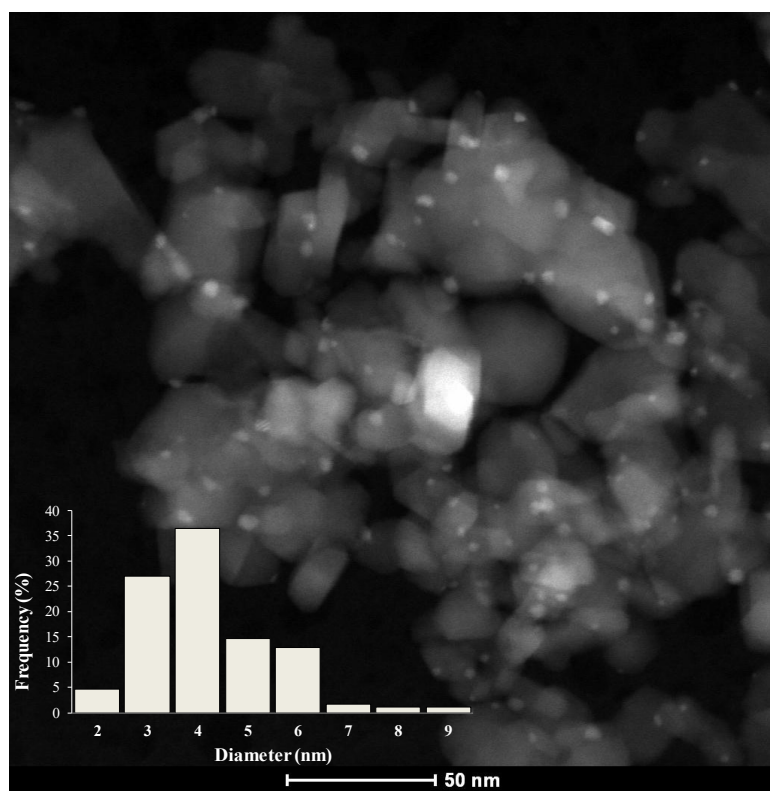


Figure 3.26. STEM-HAADF image of the 10NiMgAl<sub>3</sub>\_Rh05 catalyst and dimensional distribution of the active phase after S/DR reaction.

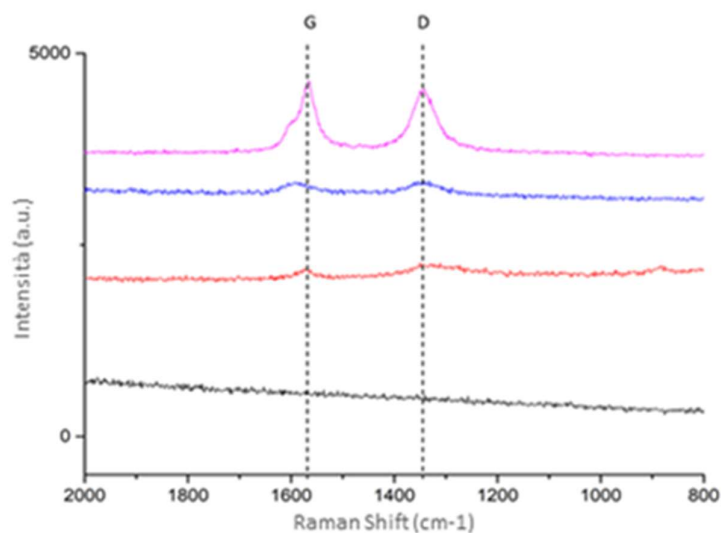


Figure 3.27. Raman spectra of the 10NiMgAl<sub>3</sub>\_Rh05 catalyst after S/DR reaction.

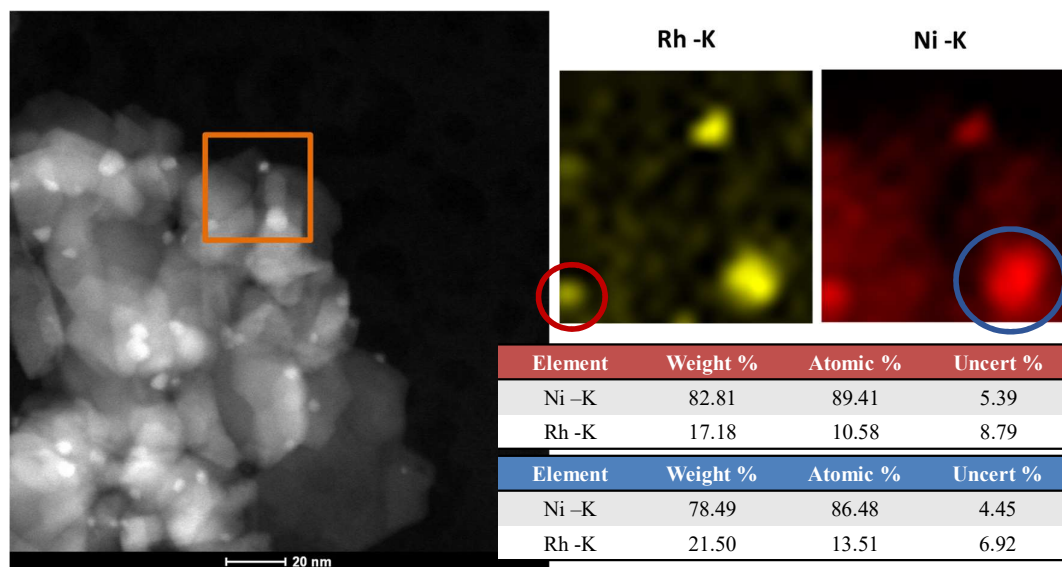


Figure 3.28. STEM-HAADF image and EDX compositional analyses of two metal particles with different diameters on the surface of the 10NiMgAl<sub>3</sub>\_Rh05 catalyst after the S/DR tests.

### 3.2.2 Preliminary conclusions

By the addition of steam to the inlet feed to perform the combined Steam/Dry Reforming (S/DR) reaction it was possible to better valorise the clean biogas content and overcome the main drawbacks of the DR. The CH<sub>4</sub> and CO<sub>2</sub> conversion values depend mainly on the amount of steam fed in the reactor. The S/CH<sub>4</sub> volumetric ratio is the key parameter that drives the two different reactions favouring a reforming process over the other and thus modifying the H<sub>2</sub>/CO molar ratio in the outlet synthesis gas. With the combined process it is possible to modulate the synthesis gas composition to more exploitable values > 1.5, avoiding the effect of the undesired Reverse Water Gas Shift (RWGS) reaction.

However, the presence of steam at high temperature can lead to the deactivation of the catalyst due to the re-oxidation of the active phase in the harsh reaction conditions. In this context, the promotion of the catalyst by a small amount of Rh (0.5 wt.%) forming an alloy with Ni, stabilizes the activity and spares the re-oxidation phenomena leading to well-distributed and stable metallic nanoparticles. The characterizations performed on the spent catalyst revealed that the synergetic effect of Rh, together with the presence of steam in the reaction environment, avoided the deactivation phenomena found previously in the DR. The over-reduction of the Ni particles to form large Ni<sup>0</sup> agglomerates was prevented and a negligible amount of carbon was deposited on the catalyst surface, very probably on account of the gasification reactions occurring in presence of steam.

### 3.3.1 Influence of the support composition

The tuning of the catalyst properties to boost the CB conversion may be realized by opportunely changing the support composition. In this context, the basicity of the catalyst could play a key role, favouring the CO<sub>2</sub> adsorption and conversion over the metallic active sites. Special attention was focused on the interaction between the active phase and the mixed oxide matrix, investigating how the interaction between NiO and MgO can affect the activity and stability in the S/DR reaction.

The influence of the support composition on the catalytic activity and stability of the Ni-Rh catalyst in the S/DR reaction was studied by changing the M<sup>2+</sup>/M<sup>3+</sup> molar ratio in the HT-precursors. Decreasing the amount of M<sup>3+</sup>, the 10NiMgAl<sub>2</sub>\_Rh05 catalyst was obtained, while increasing the Mg-content to the upper limit of the HT-precursor [3] the 10NiMgAl<sub>4</sub>\_Rh05 precursor was synthesized. The specific surface area values of the calcined catalysts were comparable, with a slight increase together with the Mg content:

**10NiMgAl<sub>2</sub>\_Rh05:** 91 m<sup>2</sup>/g; **10NiMgAl<sub>3</sub>\_Rh05:** 107 m<sup>2</sup>/g; **10NiMgAl<sub>4</sub>\_Rh05:** 107 m<sup>2</sup>/g

The calcined catalysts were composed of the same crystalline phases (Fig 3.29), while the intensity of the diffraction peaks varied accordingly to the Mg and Al content in the different samples (MgO and NiO peak more intense for the 10NiMgAl<sub>4</sub>\_Rh05 calcined catalyst).

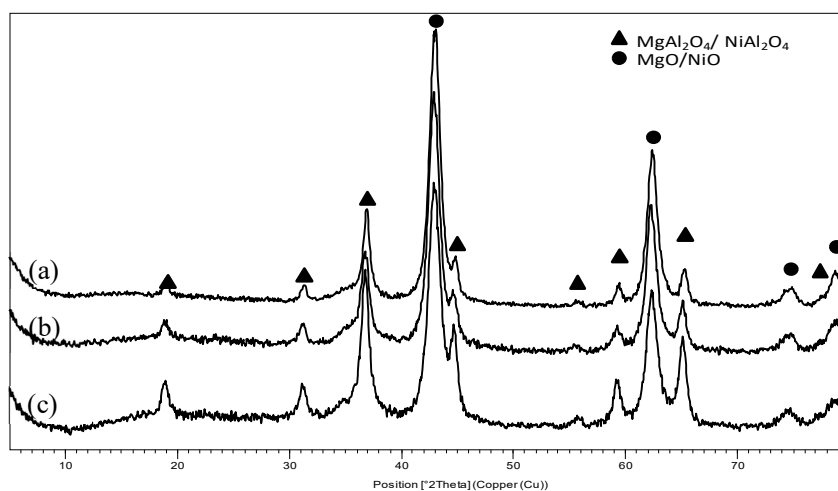


Figure 3.29. XRD patterns of the catalysts after calcination: (a) 10NiMgAl<sub>4</sub>\_Rh05, (b) 10NiMgAl<sub>3</sub>\_Rh05, (c) 10NiMgAl<sub>2</sub>\_Rh05

The properties of the catalysts were at first studied by investigating the reducibility of the active phase as a function of the Mg-content. The reduction temperature of the active

phase was greatly affected by its interaction with the catalytic support as showed by the H<sub>2</sub>-TPR profiles showed in figure 3.30.

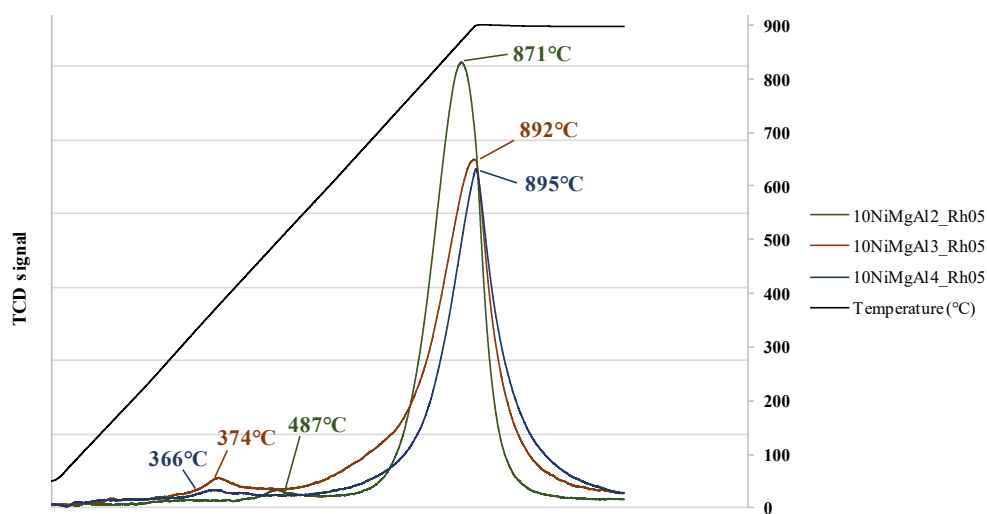


Figure 3.30. H<sub>2</sub>-TPR profiles of the three Ni-Rh catalysts after calcination.

The reduction of the catalysts took place in two separate regions; the first three broad peaks may be attributed to the reduction of the Rh<sup>3+</sup> ions weakly interacting with the catalytic support, while the intense peaks at high temperature may be ascribed to the reduction of Ni<sup>2+</sup> species (NiO and NiAl<sub>2</sub>O<sub>4</sub>) strongly interacting with the mixed oxide matrix. The increase of the Mg content (from 10NiMgAl<sub>2</sub>\_Rh05 to 10NiMgAl<sub>4</sub>\_Rh05) lowered the reduction temperature of the Rh<sup>3+</sup> species and led to a significant shift of the NiO reduction up to 895 °C (instead of 871 °C for 10NiMgAl<sub>2</sub>\_Rh05 catalyst), together with a decrease of the peak intensities. This behaviour was attributed to the formation of a MgO-NiO solid solution during the calcination. From the XRD patterns of three samples at 2θ of 41-46 ° and 60-65 ° (Fig. 3.31) it is possible to observe that, while increasing the value of the M<sup>2+</sup>/M<sup>3+</sup> ratio, an increasing shift of the reflections at 2θ = 43.0° and 62.4 ° ca., towards higher Bragg angles (typical of the NiO pattern) occurred, confirming the formation of a solid solution and suggesting a stronger interaction between the support and the active phase. The distribution of the metal particles after reduction obtained by TEM observations (Fig. 3.32) showed that the active phase was well-distributed on the catalyst surface with a size of the produced nanoparticles comprised in the range 2-12 nm, without any presence of large agglomerates. The average diameter decreased gradually at higher Mg concentration from 8 to 5 nm (10NiMgAl<sub>4</sub>\_Rh05).

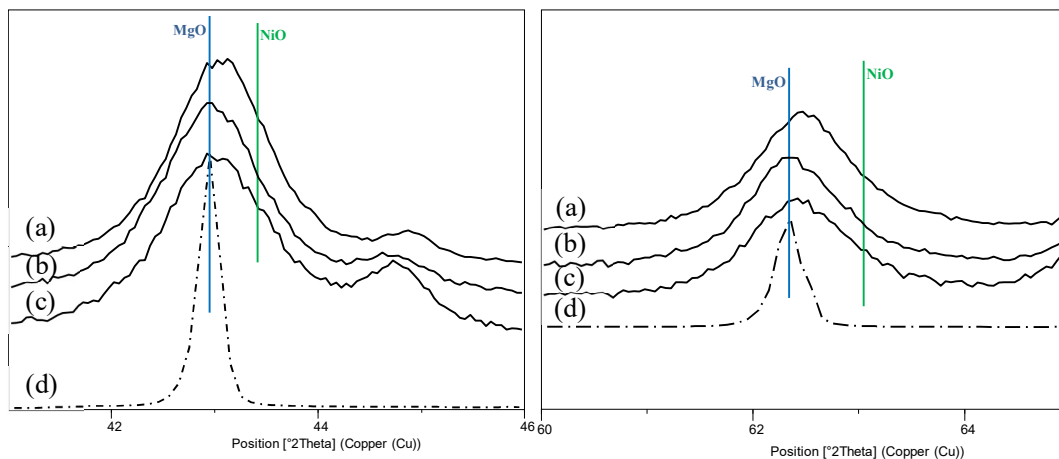


Figure 3.31. XRD patterns in the  $2\theta$  regions  $41-46^\circ$  and  $60-65^\circ$  of the samples calcined at  $900^\circ\text{C}$  for 6 h: (a)  $10\text{NiMgAl}_4\text{-Rh05}$ , (b)  $10\text{NiMgAl}_3\text{-Rh05}$ , (c)  $10\text{NiMgAl}_2\text{-Rh05}$ , (d) reference MgO.

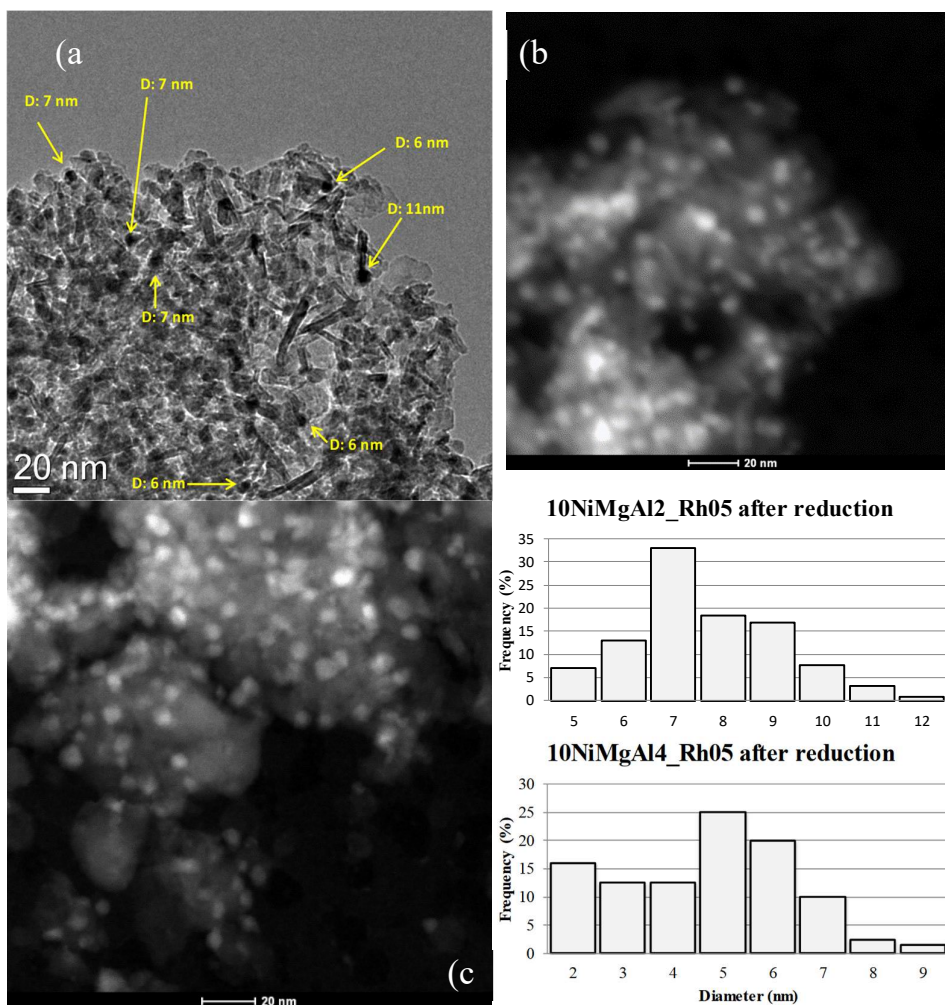


Figure 3.32. TEM image of (a)  $10\text{NiMgAl}_2\text{-Rh05}$ ; STEM-HAADF images of (b)  $10\text{NiMgAl}_2\text{-Rh05}$  (c)  $10\text{NiMgAl}_4\text{-Rh05}$  catalysts after reduction. On the right, the metal particles distribution for the two Ni-Rh catalysts after reduction.

The two catalysts, namely 10NiMgAl2\_Rh05 and 10NiMgAl4\_Rh05, were tested using the same procedure reported in the previous paragraphs and the activities were compared with those obtained for the 10NiMgAl3\_Rh05 catalyst in terms of CH<sub>4</sub> conversion values (Fig. 3.33).

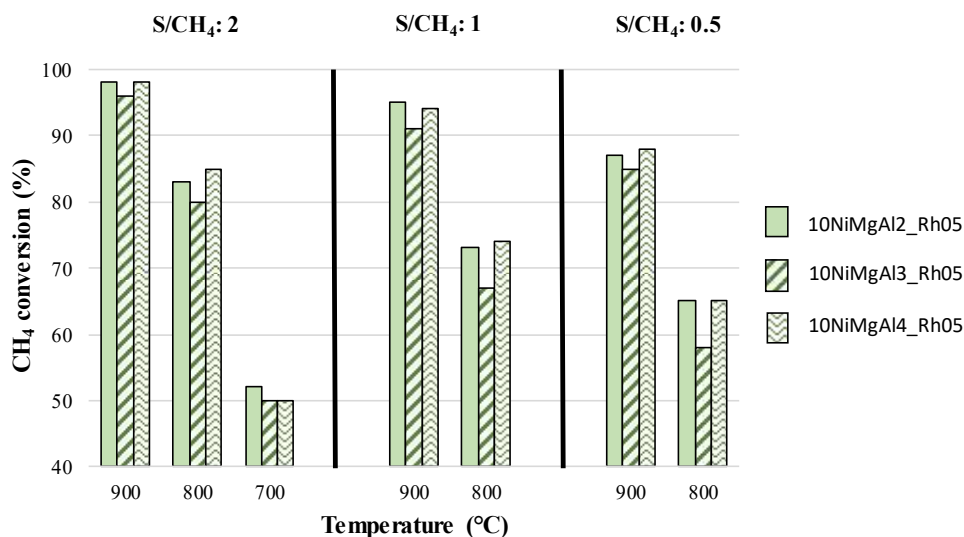


Figure 3.33. CH<sub>4</sub> conversion for the three Ni-Rh catalysts in the S/DR reaction.

The 10NiMgAl2\_Rh05 and 10NiMgAl4\_Rh05 catalysts showed the same activity, with negligible differences as a function of the reaction parameters. In the two latter cases, the CH<sub>4</sub> conversion is higher if compared to that showed by the 10NiMgAl3\_Rh05 sample regardless of the conditions tested, especially at lower temperatures and S/CH<sub>4</sub> ratios. A similar trend can be seen in the CO<sub>2</sub> conversions (Fig. 3.34), although the many side reactions that can involve this reactant do the interpretation of the results more difficult. Increasing the Mg-content (M<sup>2+</sup>/M<sup>3+</sup> value from 2 to 4) the CO<sub>2</sub> conversion seemed to slightly improve, especially at low temperature and decreasing the S/CH<sub>4</sub> value, where the DR reaction is favoured (i.e. T = 800 °C, S/CH<sub>4</sub> = 1.0-0.5). The H<sub>2</sub>/CO molar ratio reported in Figure 3.35, showed no significant differences in the behaviour of the different catalysts, that however produced in most of the reaction conditions a syngas suitable for further downstream applications such as the Fischer-Tropsch and the methanol synthesis, without needing a further Water Gas Shift (WGS) step to increase the H<sub>2</sub> yield

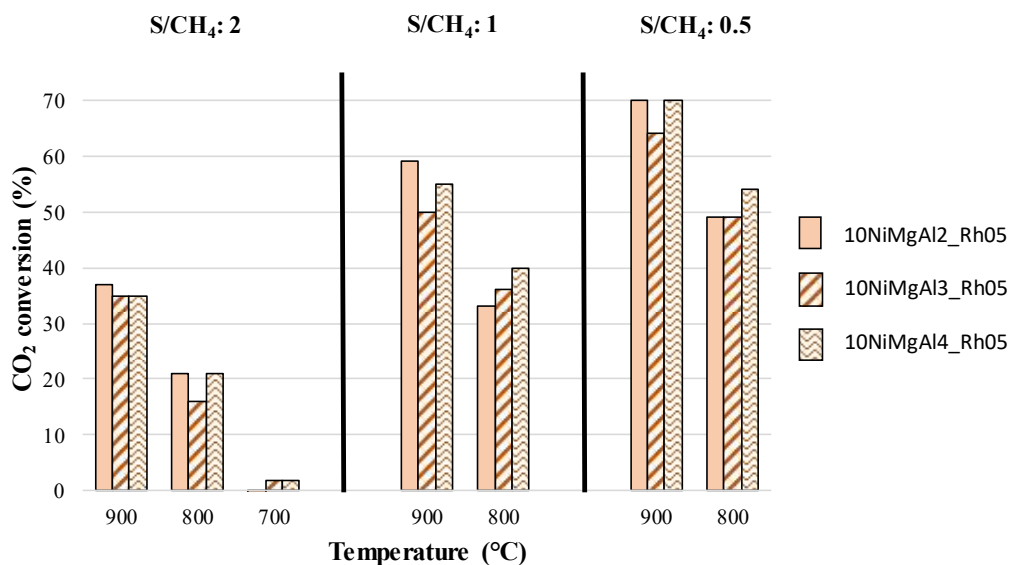


Figure 3.34. CO<sub>2</sub> conversion for the three Ni-Rh catalysts in the S/DR reaction.

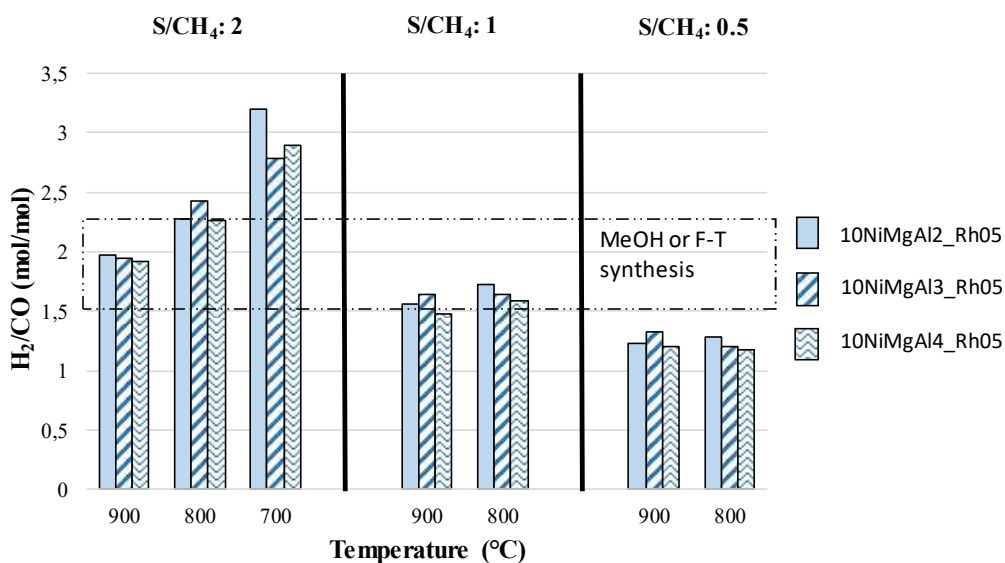


Figure 3.35. H<sub>2</sub>/CO molar ratio in the syngas produced in the S/DR reaction for the three Ni-Rh catalysts.

The improved activity of the 10NiMgAl<sub>4</sub>\_Rh05 catalyst can be correlated to the increased basicity of the support. The CO<sub>2</sub>-TPD profiles (Fig. 3.36 a) of the catalysts before reaction showed a clear difference between the three samples in terms of support basicity and, consequently, CO<sub>2</sub> adsorption. The intensities of the peaks increased with the Mg-content in the catalyst and three main desorption regions can be observed. The low temperature desorption peaks (110-120 °C) may be assigned to bicarbonate species formed on surface OH groups (weak basic sites); the middle temperature broad peaks (120-250 °C) were

attributed to bidentate carbonates desorbed from  $\text{Mg}^{2+}\text{-O}^{2-}$  pairs, while the high temperature peaks ( $> 250$  °C), clearly visible in the 10NiMgAl4\_Rh05 desorption profile, may be associated to the unidentate carbonates released from low-coordination  $\text{O}^{2-}$  anions (strong basic sites) [4,5]. By integrating the three curves, the total amount of adsorbed  $\text{CO}_2$  (mmoles/ $\text{g}_{\text{cat}}$ ) was calculated for each catalyst (Fig. 3.36 b), showing that the  $\text{CO}_2$  adsorption approximately doubled each time the  $\text{M}^{2+}/\text{M}^{3+}$  molar ratio was increased of one unit.

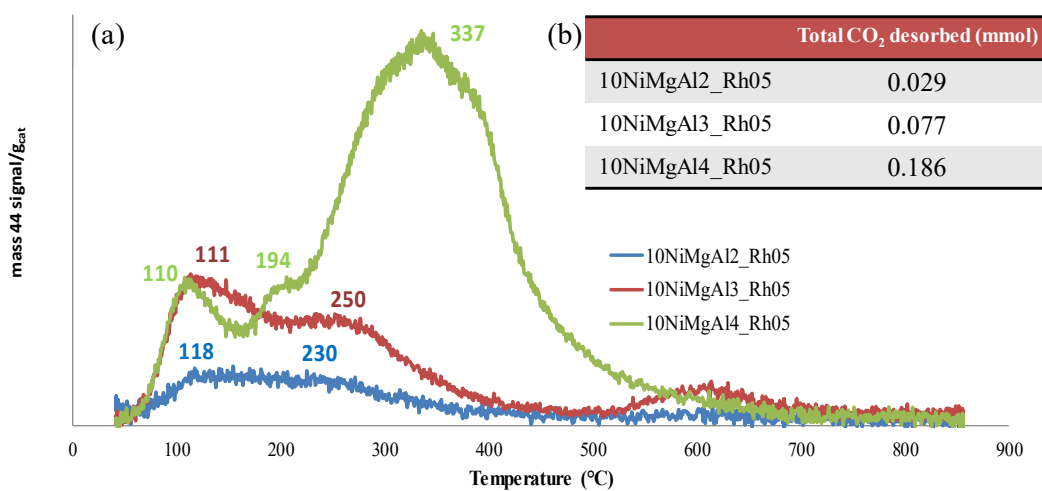


Figure 3.36. (a)  $\text{CO}_2$ -TPD profiles of the Ni-Rh catalysts after calcination; (b) Total amount of  $\text{CO}_2$  desorbed during the analyses for each catalyst.

The deactivation of the catalysts was monitored at the end of the catalytic tests, repeating the first test conducted ( $T = 900$  °C,  $\text{S}/\text{CH}_4 = 2$ ) and evaluating the differences in terms of  $\text{CH}_4$  and  $\text{CO}_2$  conversions after the same time-on-stream for the different catalysts. The results (Fig. 3.37) did not show any appreciable deactivation for the 10NiMgAl3\_Rh05 and 10NiMgAl4\_Rh05 catalysts, while revealed a drop in the  $\text{CO}_2$  conversion of  $\approx -16$  % for the sample 10NiMgAl2\_Rh05. The Raman spectra of the spent catalysts (Fig. 3.38) showed negligible presence of carbon regardless of the composition, such as confirmed by the TG analyses that presented weak weight losses ( $< 0.9$  %), attributable to the evolution of adsorbed surface water during the experiments.

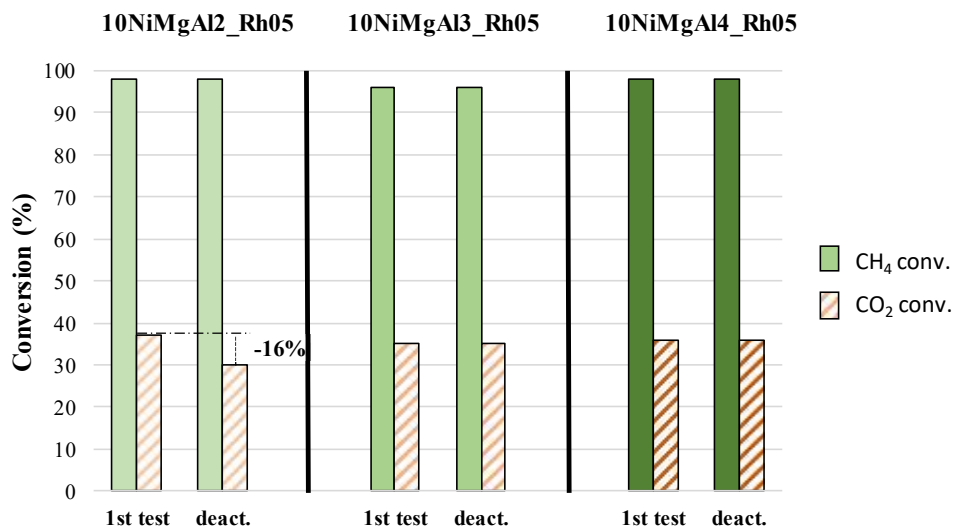


Figure 3.37. Results of the deactivation tests conducted on the catalysts, the percentage displayed for the 10NiMgAl<sub>2</sub>\_Rh05 indicates the deactivation in terms of CO<sub>2</sub> conversion.

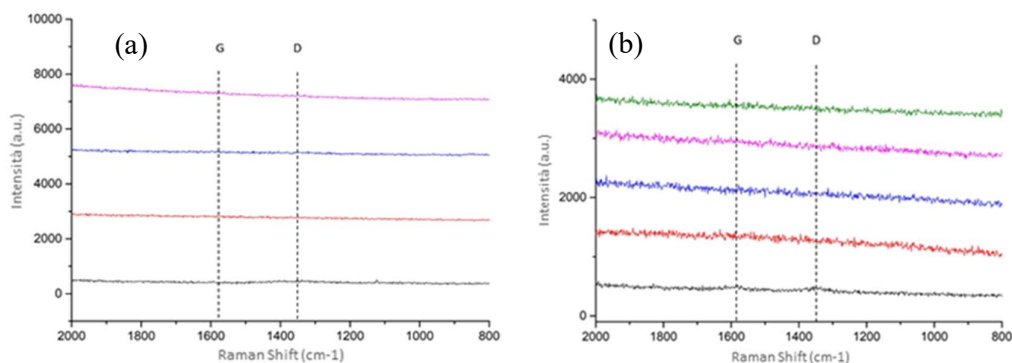


Figure 3.38. Raman spectra of the two spent catalysts: (a) 10NiMgAl<sub>2</sub>\_Rh05, (b) 10NiMgAl<sub>4</sub>\_Rh05

From the distributional analyses of the active phase obtained by TEM images of the catalysts after reaction (Fig.3.39), the sintering of the 10NiMgAl<sub>2</sub>\_Rh05 metal particles occurring during the reaction can be observed. No significant changes were visible in the 10NiMgAl<sub>3</sub>\_Rh05 and 10NiMgAl<sub>4</sub>\_Rh05 nanoparticles size, while the S/DR reaction led to an increase of the average diameter of the 10NiMgAl<sub>2</sub>\_Rh05 active phase (up to 10 nm) together with the formation of metal agglomerates larger than 20 nm, that caused the catalyst deactivation.

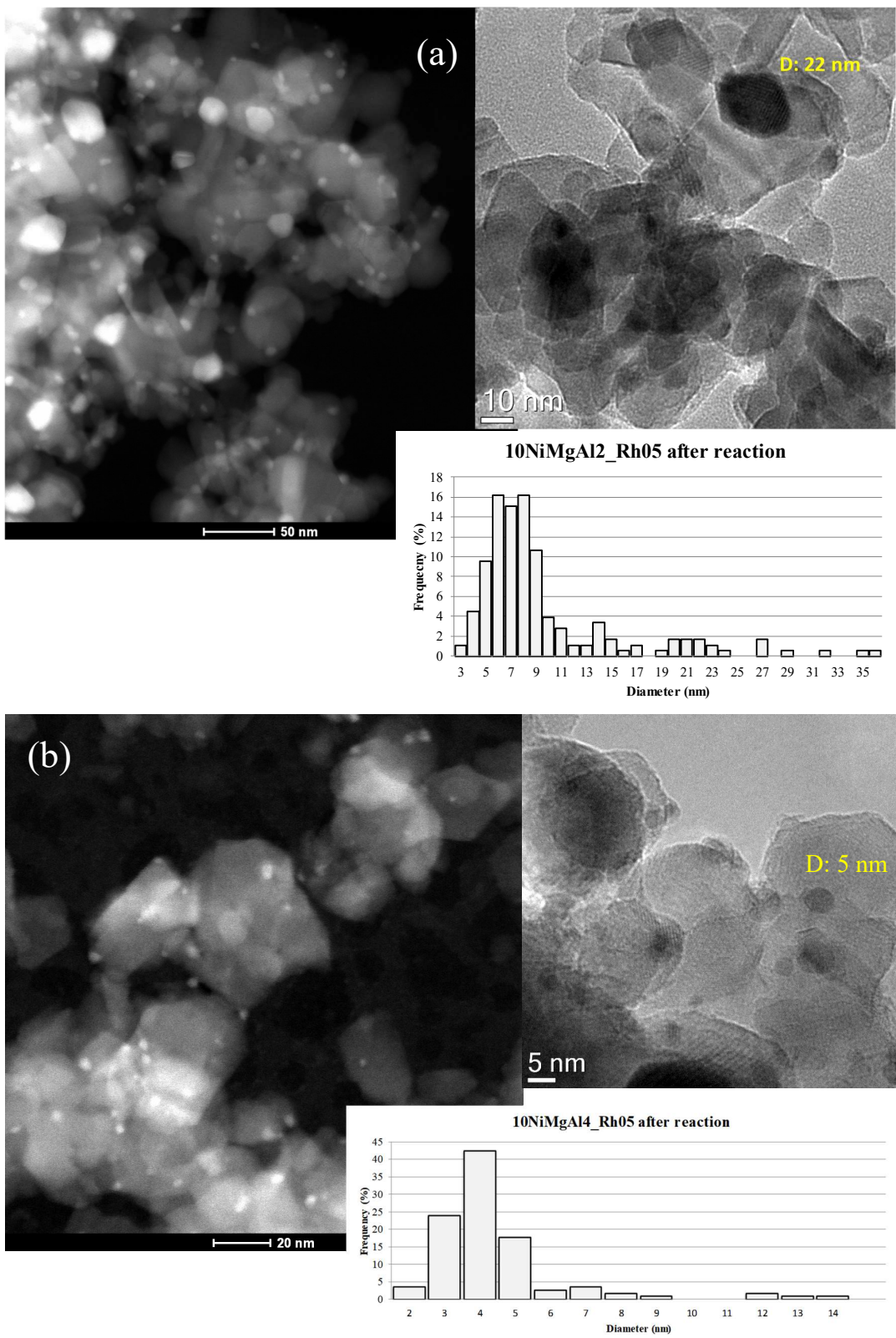


Figure 3.39. TEM and STEM-HAADF images and statistical distributions of the active phase after reaction for the (a) 10NiMgAl<sub>2</sub>\_Rh05 and (b) 10NiMgAl<sub>4</sub>\_Rh05 catalysts.

The BET and XRD analyses revealed a loss in the specific surface area after reaction of  $\approx 60-70\%$ , together with a comparable increase of the crystallite sizes for the three catalysts (Table 3.1):

Table 3.1. BET specific surface area of the catalysts and crystallite sizes (D) of a) MgO/NiO and b) Spinel phase.

Catalysts	SSA (m <sup>2</sup> /g) after calcination	SSA (m <sup>2</sup> /g) after reaction	D (nm) after calcination	D (nm) after reaction
10NiMgAl2_Rh05	91	30	<sup>a</sup> 11, <sup>b</sup> 12	<sup>a</sup> 25, <sup>b</sup> 32
10NiMgAl3_Rh05	107	40	<sup>a</sup> 12, <sup>b</sup> 14	<sup>a</sup> 24, <sup>b</sup> 27
10NiMgAl4_Rh05	95	29	<sup>a</sup> 11, <sup>b</sup> 16	<sup>a</sup> 26, <sup>b</sup> 32

According to the results previously discussed, the XRD patterns of the spent catalysts showed an increase of the crystallinity (Fig 3.40) and no detectable peaks that can be attributed to the presence of Ni<sup>0</sup>, probably due to its high dispersion on the oxides matrix.

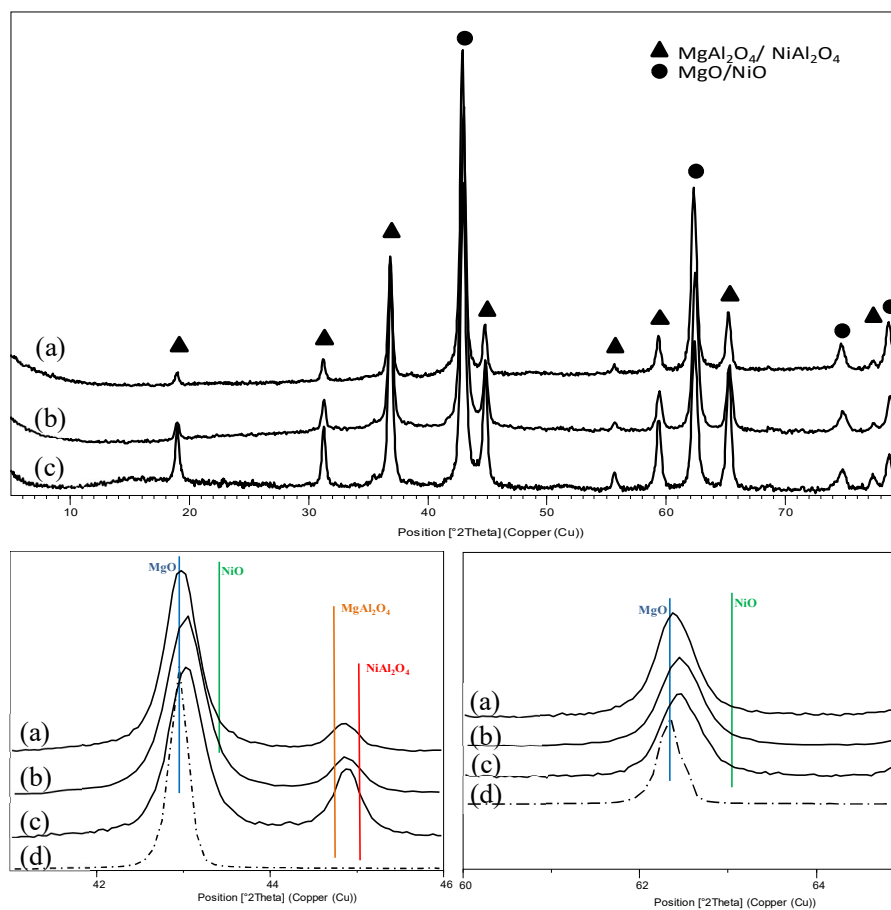


Figure 3.40. XRD patterns of the catalysts calcined at 900 °C for 6 h after reaction in the 2 $\theta$  regions 5-80 ° (top) and 41-46 ° and 60-65 ° (bottom): (a) 10NiMgAl4\_Rh05, (b) 10NiMgAl3\_Rh05, (c) 10NiMgAl2\_Rh05 and (d) reference MgO.

A shift of the two peaks at  $2\theta = \text{ca } 43.0$  and  $62.4^\circ$  to lower Bragg angles (typical of the MgO pattern) can be observed mainly for the 10NiMgAl4\_Rh05 catalyst, revealing that a segregation of the Ni particles from the MgO-NiO solid solution occurred, leading to the formation of stable Ni<sup>0</sup> nanoparticles strongly interacting with the catalytic support.

### **3.3.2 Preliminary conclusions**

The composition of the catalyst support affected significantly the properties of the catalysts in the S/DR reaction. The increase in the Mg-content in the catalyst formulation decreased the reducibility of the NiO phase but improved the interaction between the active phase and the support, due to the formation of a NiO-MgO solid solution after calcination. This phenomenon, together with the stronger basic sites present at the surface of the 10NiMgAl4\_Rh05 catalyst, improved the dispersion of the active phase increasing its activity and resistance to the sintering processes that leads to the catalyst deactivation. The agglomeration of the metal particles observed for the 10NiMgAl2\_Rh05 catalyst changed the activity during the tests, reducing the CO<sub>2</sub> conversion value and pointing out that the particles size may control the equilibrium between the SR and DR reactions when they are carried out in a one-step process.

### 3.4.1 Influence of Rh content

In the following chapter, the influence of Rh-content on the catalyst activity and stability will be investigated. Starting from the good results obtained for the 10NiMgAl4\_Rh05 catalyst, the amount of Rh will be changed to decrease the costs associated to a large-scale production of this promoted catalyst and to study how its concentration affects the dispersion of the active phase and the CB conversions in the S/DR reaction.

The amount of Rh in the different catalysts was varied from 0.00 to 1.40 wt.%, changing its amount in the HT-precursors, using the 10NiMgAl4\_Rh05 catalyst as reference, to obtain the catalyst compositions reported in Table 3.2 together with their BET specific surface area and crystallite size values after calcination at 900 °C for 6 h.

Table 3.2. Compositions of the final catalysts varying the Rh-content, their specific surface areas values and crystallite sizes calculated through the Scherrer equation after calcination of a) MgO/NiO and b) Spinel phase.

<b>Catalysts</b>	<b>Ni wt.%</b>	<b>Rh wt.%</b>	<b>Mg wt.%</b>	<b>Al wt.%</b>	<b>SSA (m<sup>2</sup>/g)</b>	<b>D (nm)</b>
10NiMgAl4	10.00	///	39.00	12.00	102	<sup>a</sup> 11, <sup>b</sup> 13
10NiMgAl4_Rh003	10.00	0.03	39.00	12.00	91	<sup>a</sup> 11, <sup>b</sup> 16
10NiMgAl4_Rh05	10.00	0.50	39.00	12.00	95	<sup>a</sup> 11, <sup>b</sup> 16
10NiMgAl4_Rh14	10.00	1.40	38.00	12.00	107	<sup>a</sup> 11, <sup>b</sup> 15

The physical properties, as specific surface area and crystallinity, seemed not to be influenced by changing the Rh-content as confirmed by the XRD patterns of the calcined catalysts (not reported), that did not show appreciable differences between the samples. The Ni-Rh interaction was studied before reaction by H<sub>2</sub>-TPR experiments (Fig. 3.41). The increase in Rh-content gave rise to a shift of the NiO reduction peak towards lower temperatures (reaching 860 °C for Rh = 1.40 wt.%) together with an increase of the TCD signal intensity. The peak associated to the reduction of Rh<sup>3+</sup> species was visible only at high metal concentration, with a reduction temperature that increased with the Rh content. The increasing reducibility of the catalysts led to a different dispersion of the active phase after reduction (Fig. 3.42). The average diameter of the metal particles decreased considerably by incrementing the Rh-content and the centre of the statistical distributions (Fig. 3.43) moved from a value of 16 nm (10NiMgAl4) to 5-4 nm for the 10NiMgAl4\_Rh05 and 10NiMgAl4\_Rh14 catalysts, respectively.

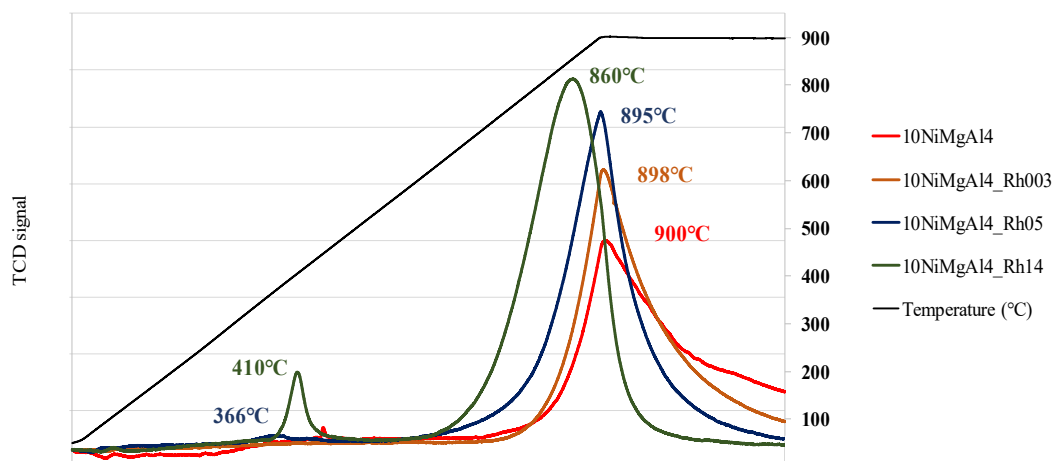


Figure 3.41. H<sub>2</sub>-TPR profiles of the catalysts after calcination at increasing Rh-content.

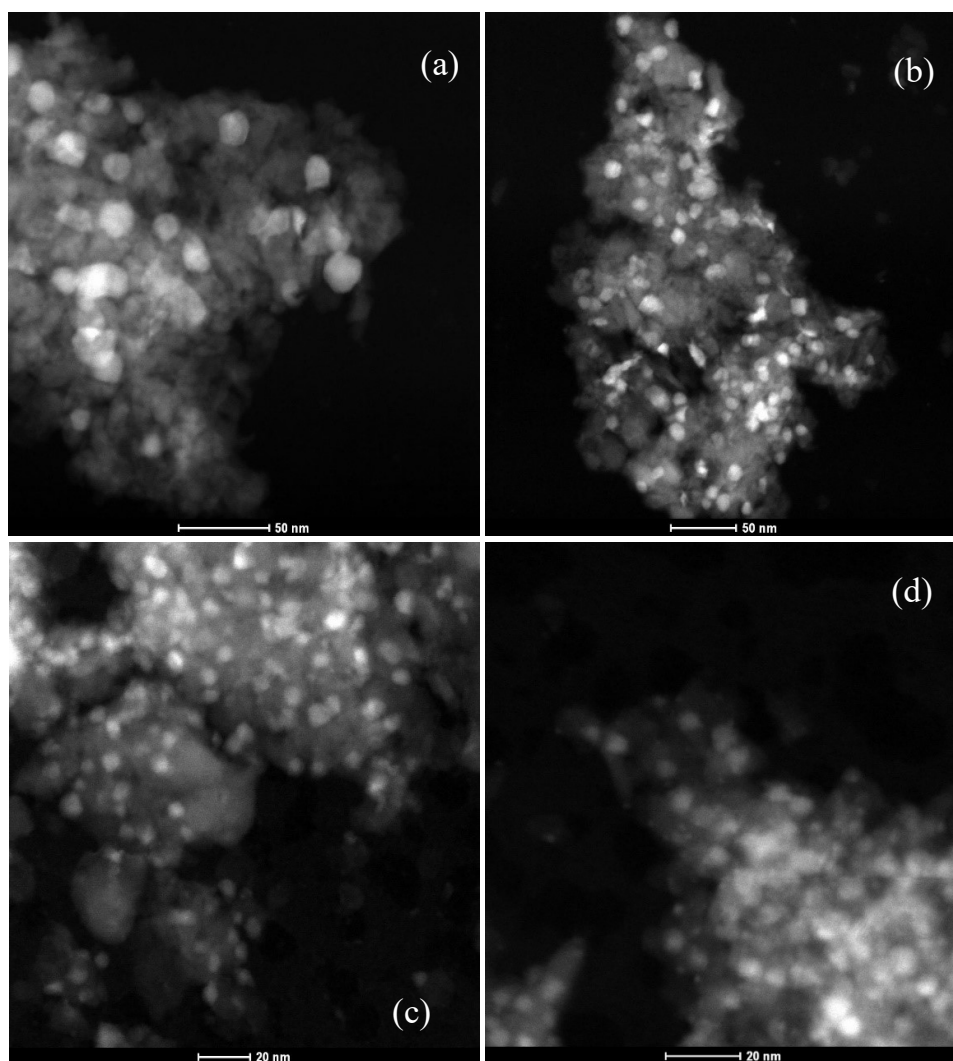


Figure 3.42. STEM-HAADF images of the catalysts after reduction: a) 10NiMgAl<sub>4</sub>, b) 10NiMgAl<sub>4</sub>\_Rh003, c) 10NiMgAl<sub>4</sub>\_Rh05, d) 10NiMgAl<sub>4</sub>\_Rh14.

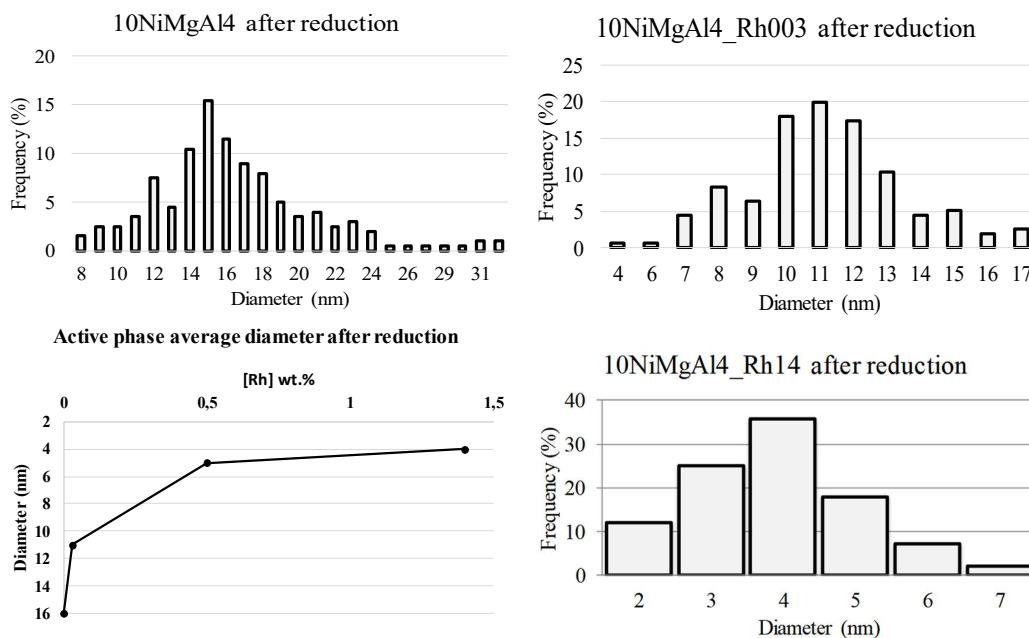


Figure 3.43. Statistical distributions of the active phase after the reduction in the different catalysts.

This trend affected the activity of the catalysts, in which the differences in the dispersions of the active phase strongly reflected. The results obtained in terms of CH<sub>4</sub> conversion (Fig. 3.44) showed that the addition of increasing amounts of Rh greatly improved the performance of the catalysts, especially at low temperature.

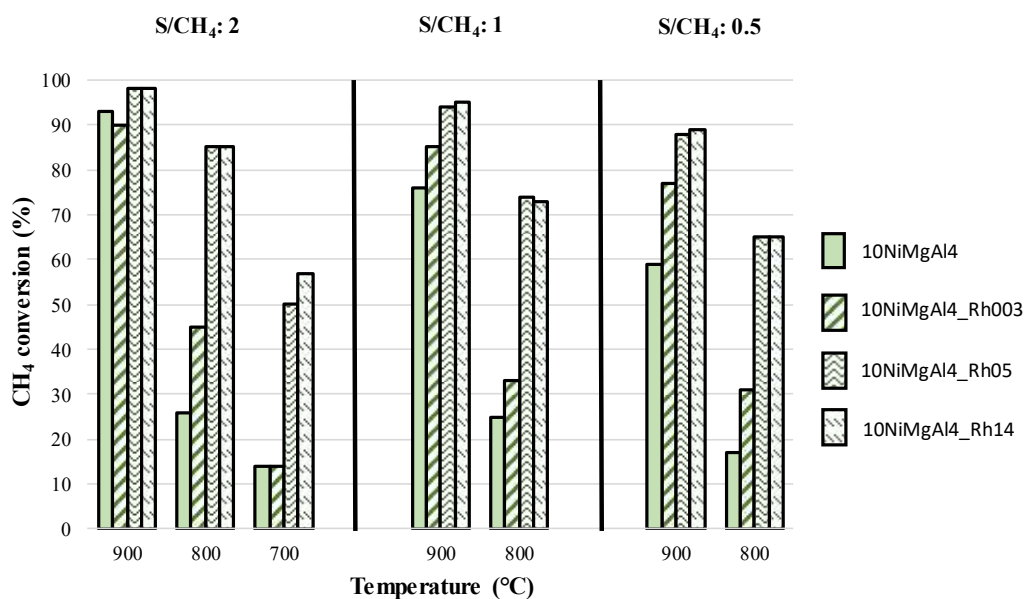


Figure 3.44. Activity of the catalysts in terms of CH<sub>4</sub> conversion in the S/DR reaction.

In fact, even if the activity differences were low near the thermodynamic equilibrium conditions ( $T = 900\text{ }^{\circ}\text{C}$ ,  $S/\text{CH}_4 = 2$ ), a significant improvement was observed for all the other conditions tested, with an increase higher than 100 % at 700-800  $^{\circ}\text{C}$  and  $S/\text{CH}_4$  ratios of 1.0-0.5. The addition of a pitiful amount of Rh (from 0.0 to 0.03 wt.%) was sufficient to increase the  $\text{CH}_4$  conversion, especially at low steam concentrations. The further addition of Rh to 0.5 wt.% additionally improved the performance of the catalyst that reached high conversion values in all the reaction conditions. The results obtained for the 10NiMgAl4\_Rh14 catalyst were comparable to those observed for the previous catalyst, suggesting that over a certain value of Rh ( $> 0.5\text{ wt.}\%$ ), a plateau in the catalyst activity is reached, and a further addition does not improve the CB conversion.

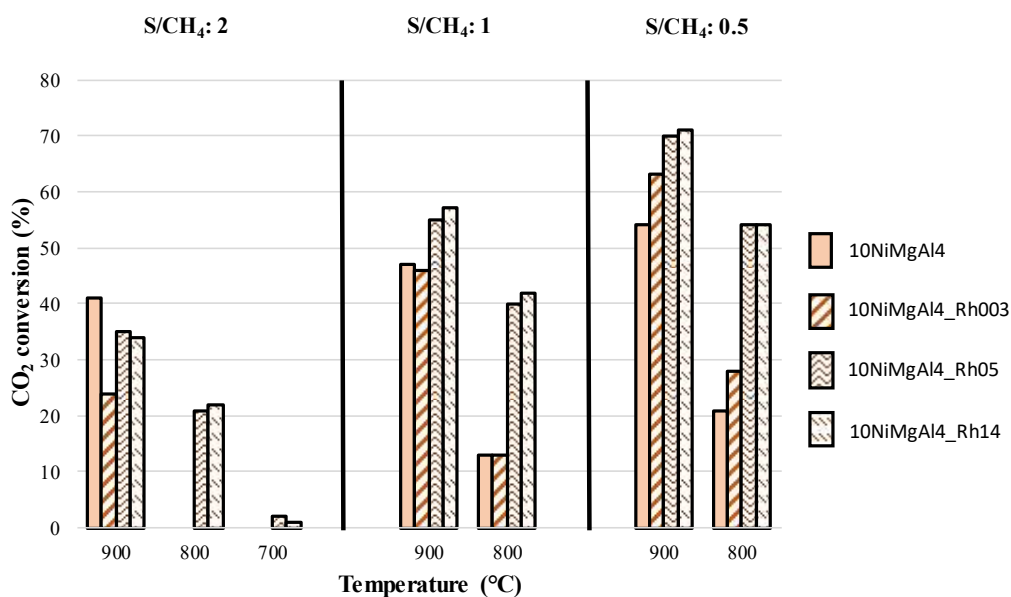


Figure 3.45. Activity of the catalysts in terms of  $\text{CO}_2$  conversion in the S/DR reaction

A similar behaviour was observed for the  $\text{CO}_2$  conversion values, that showed high but comparable activities for 10NiMgAl4\_Rh05 and 10NiMgAl4\_Rh14 catalysts (Fig. 3.45). The presence of Rh significantly improved the  $\text{CO}_2$  conversion at 700-800  $^{\circ}\text{C}$ , favouring the DR reaction at low  $S/\text{CH}_4$  values, exhibiting some DR activity also at  $S/\text{CH}_4 = 2$  for the higher Rh concentrations, as confirmed by the lower  $\text{H}_2/\text{CO}$  values obtained in these conditions by increasing the Rh-content (Fig. 3.46). The composition of the produced syngas (in terms of CO and  $\text{H}_2$  concentrations) did not show significant differences between the catalysts, although it seemed variable in the conditions in which the CB

conversions were low, where the H<sub>2</sub>/CO values exceeded values of 3 due to the occurrence of the WGS reaction, especially for the catalysts with low Rh-content.

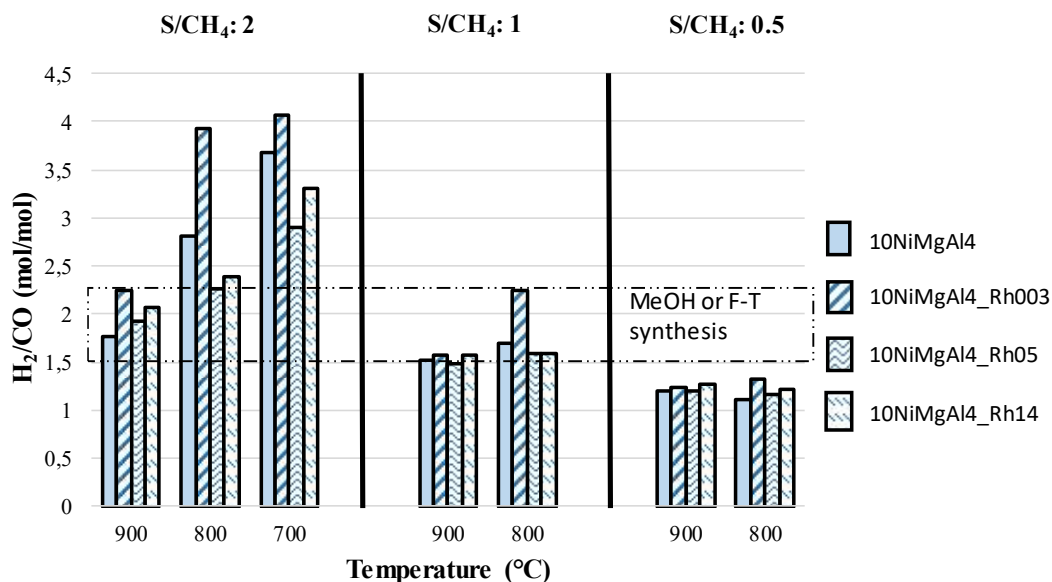


Figure 3.46. H<sub>2</sub>/CO molar ratio of the exit syngas varying the amount of Rh in the four Ni-based catalysts.

The presence of Rh affected also the stability of the catalysts. In Table 3.3 the percent losses in terms of CH<sub>4</sub> and CO<sub>2</sub> conversions revealed from the deactivation tests are reported. A strong deactivation was observed for the un-promoted catalyst, probably also due to some re-oxidation phenomena already observed in paragraph 3.2. The loss in activity decreased by increasing the Rh-content, reaching a complete stability for the 10NiMgAl<sub>4</sub>\_Rh05 and 10NiMgAl<sub>4</sub>\_Rh14 catalysts. It is noteworthy that in any case the deactivation values in terms of CO<sub>2</sub> conversion were always higher than those calculated for the CH<sub>4</sub> conversion.

Table 3.3. Deactivation percentage values in terms of losses in CH<sub>4</sub> and CO<sub>2</sub> conversions.

Deactivation	[Rh] 0 wt. %	[Rh] 0.03 wt. %	[Rh] 0.5 wt. %	[Rh] 1.4 wt. %
CH <sub>4</sub> conv.	-20 %	-4 %	0 %	0%
CO <sub>2</sub> conv.	-46 %	-13 %	0 %	0%

The carbon formed during the reaction determined by TG analyses (Tab. 3.4) followed the same trend, with maximum formation for 10NiMgAl<sub>4</sub> (mass lost 0.98 %) but not in the extent to fully justify the deactivation observed.

Table 3.4. Mass lost in TG analyses due to the presence of carbon on the catalysts after reaction.

<b>Mass lost (%)</b>			
<b>[Rh] 0 wt. %</b>	<b>[Rh] 0.03 wt. %</b>	<b>[Rh] 0.5 wt. %</b>	<b>[Rh] 1.4 wt. %</b>
0.98	0.85	0.08	0.02

The instability of the catalyst was due to the sintering of the active phase, limited by the presence of Rh for the 10NiMgAl4\_Rh05 and 10NiMgAl4\_Rh14 samples. The distributions of the nanoparticles obtained by the TEM images of the catalysts after reaction (Fig. 3.47) showed a strong occurrence of this phenomenon for the un-promoted catalyst, with the formation of large particles with a diameter over 150 nm, that can notably decrease the metallic surface area, and a size distribution centre of the smaller nanoparticles shifted from 16 to 18 nm after reaction. The extent of the sintering process was lower for the 10NiMgAl4\_Rh003, although the formation of large agglomerates of  $\approx 80$  nm was observed together with a broadening in the dispersion of the active phase. The deactivation of the catalysts was hence strictly related to metal particles size and the increase of the Rh content to 0.5-1.4 wt.% suppressed the sintering of the active phase, with a similar extent due to higher formation of the Ni-Rh alloy (Fig. 3.48), explaining the improved stability of these two formulations.

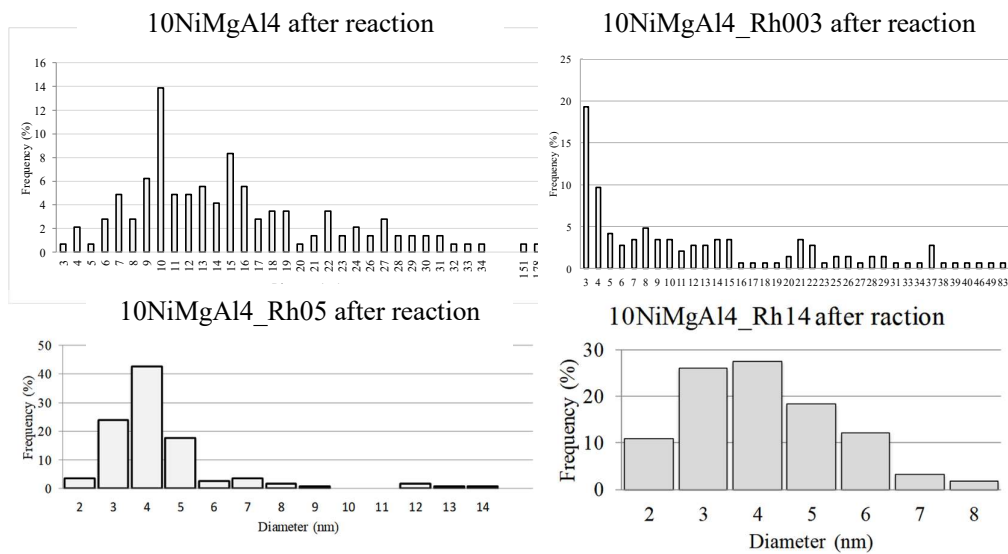
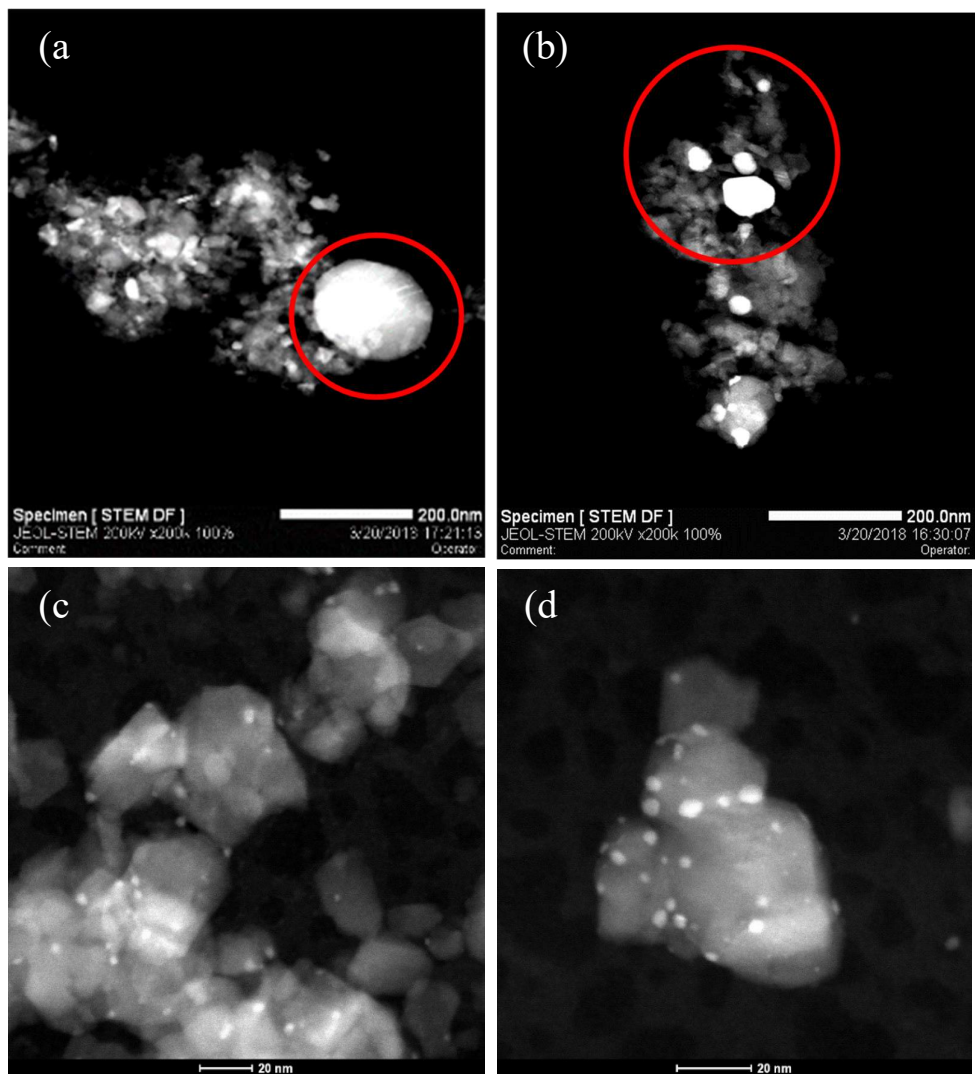


Figure 3.47. STEM-HAADF images of the catalysts after reaction: a) 10NiMgAl4, b) 10NiMgAl4\_Rh003, c) 10NiMgAl4\_Rh05, d) 10NiMgAl4\_Rh14 and the respective distributions of the metal particles (bottom).

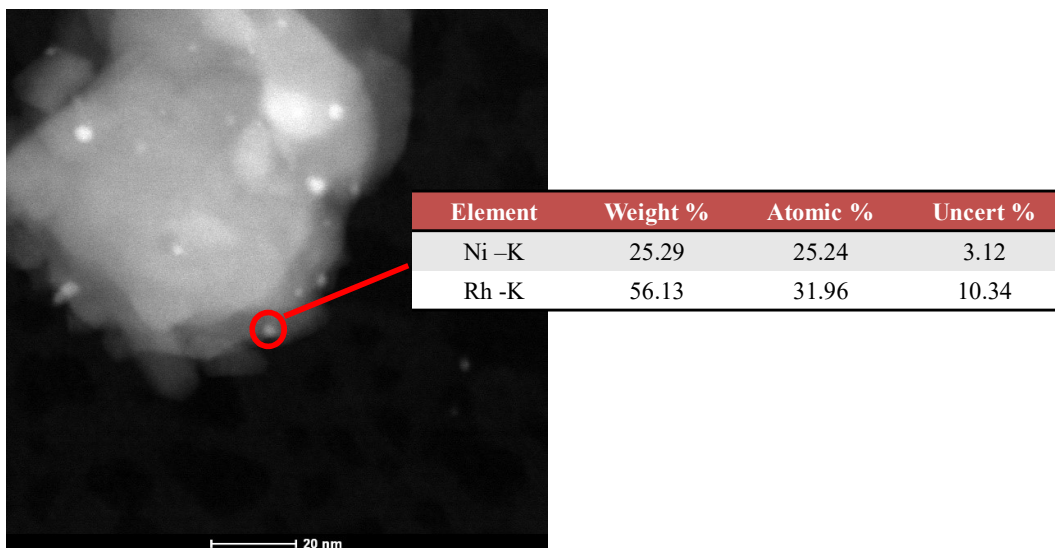


Figure 3.48. STEM-HAADF image and EDX compositional analysis of a metal particle for the 10NiMgAl4\_Rh14 catalyst after reaction

### 3.4.2 Preliminary conclusions

The activity and stability of the Ni-based catalysts are strictly related and directly proportional to the Rh-content in the formulation. The synergetic effect between this element and the reduced Ni particles is reflected in the improved reducibility of the catalyst and optimum dispersion of the active phase before reaction. The extensive formation of the Ni-Rh alloy at increasing Rh-contents determine the catalytic activity and the properties of the metallic nanoparticles. The improved dispersion of the bi-metallic nanoparticles increases the catalytic activity and stability leading to good performance even at the lowest reaction temperatures. The presence of an increasing amount of Rh leads to suppression of the carbon formed during reaction and avoid the sintering of the active phase and, consequently, the deactivation of the catalysts. Although the addition of the noble metal has a good effect even at low concentration (0.03 wt.%), only a higher concentration of Rh can assure a significant formation of the alloy on the surface, reaching a plateau in the promotion effects when the Rh-content exceeds 0.5 wt.%.

### 3.5.1 Substitution of Rhodium with Copper

The improved activity and stability of the bi-metallic catalysts, that have been deeply studied and discussed in the previous sections, will be further investigated in the following paragraph. Considering that the excellent results observed for the Ni-Rh catalysts are ascribable to the formation of an alloy between the metals, the substitution of Rh with a cheaper transition metal was investigated. Copper has the ability to form alloys with nickel (Fig. 3.49) and the bimetallic active phase had been claimed as active in SR of both ethanol and methanol [6,7]. The low cost of this element is an interesting feature that can improve the feasibility of a large-scale production of the catalyst for the valorisation of the CB.

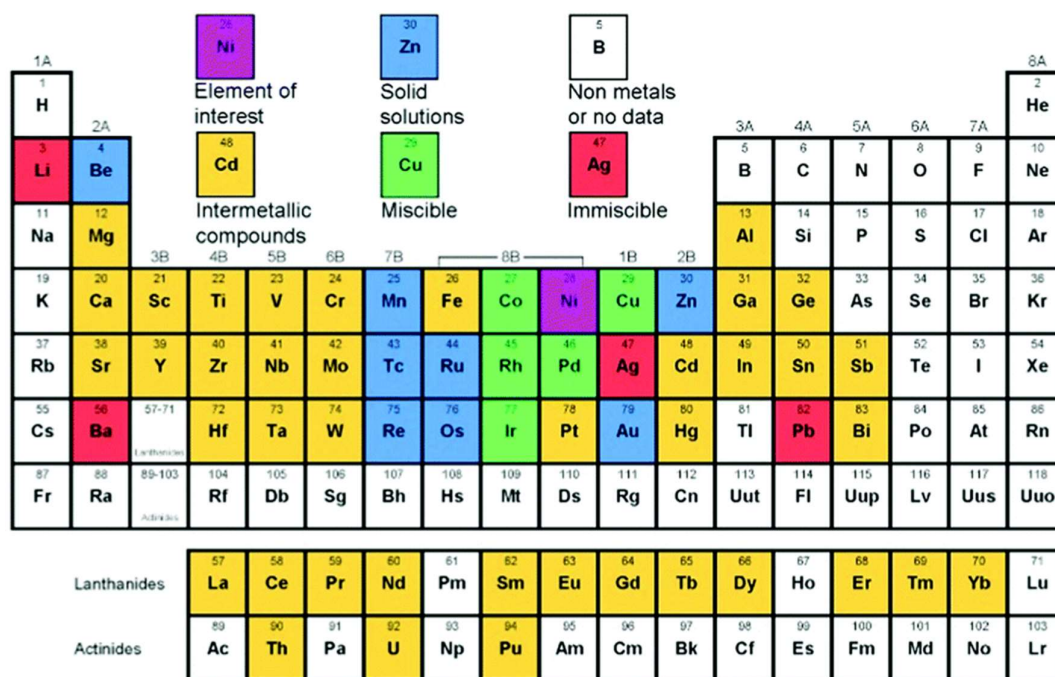


Figure 3.49. Binary Ni-containing alloys table as reported by Nash [8].

The influence of the Cu on the activity and stability of the 10NiMgAl<sub>4</sub> catalyst was investigated by synthesizing two Ni-Cu based catalysts with a Cu-content of 0.5 or 2.0 wt.% (10NiMgAl<sub>4</sub>\_Cu05 and 10NiMgAl<sub>4</sub>\_Cu2, respectively). The XRD analysis of the calcined samples (Fig. 3.50) did not show significant differences between the patterns. The Cu was probably present in the two samples as CuO and CuAl<sub>2</sub>O<sub>4</sub> but the overlapping of their characteristic peaks with those of the other oxides and spinel-type phases did impossible their identification.

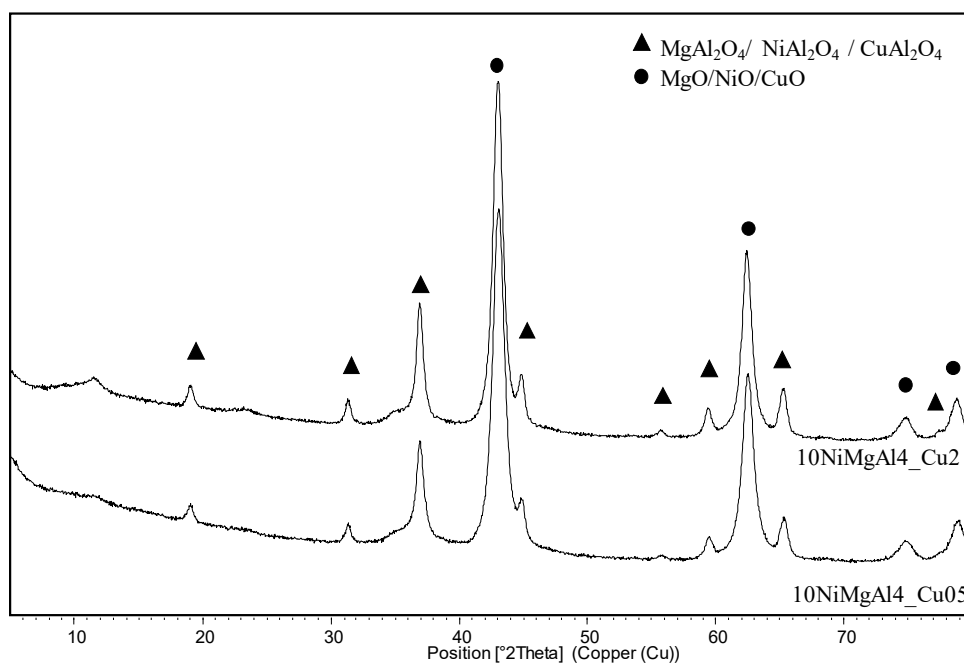


Figure 3.50. XRD patterns of the two Ni-Cu catalysts after calcination at 900°C for 6 h.

The increase of the Cu-content led to a significant decrease in the specific surface area of the catalysts accompanied by a small increase of the crystallite sizes for the two crystalline phases after calcination at 900 °C for 6 h (Tab. 3.4).

Table 3.4. Cu-content in the different catalysts, respective BET specific surface areas after calcination at 900°C for 6 h and crystallite sizes calculated through the Scherrer equation after calcination of a) MgO/NiO and b) Spinel phase.

Catalysts	[Cu] wt.%	SSA (m <sup>2</sup> /g)	D (nm)
10NiMgAl4	0.0	102	<sup>a</sup> 11, <sup>b</sup> 13
10NiMgAl4_Cu05	0.5	74	<sup>a</sup> 10, <sup>b</sup> 15
10NiMgAl4_Cu2	2.0	56	<sup>a</sup> 12, <sup>b</sup> 17

The addition of a 0.5 wt.% of Cu to the catalyst formulation brought to a good improvement of the CB conversion. The comparison between the CH<sub>4</sub> conversion of this catalyst with that previously detected for the un-promoted sample (Fig. 3.51) revealed the better performances of the Ni-Cu catalyst regardless of the reaction conditions. Impressive results were obtained at 800°C, where the presence of Cu led to an improvement higher than 100 % (in particular at the S/CH<sub>4</sub> ratio = 2), while the conversion values at 900 °C were comparable with those obtained with the Rh-promoted 10NiMgAl4\_Rh05 catalyst.

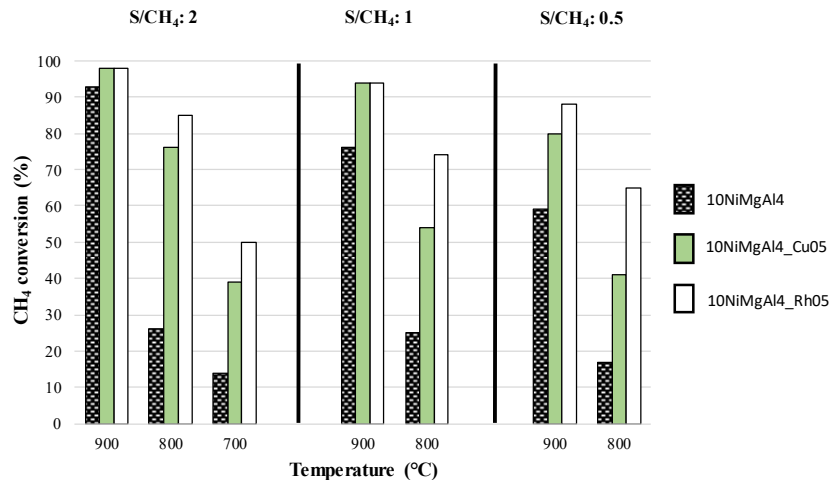


Figure 3.51. CH<sub>4</sub> conversion in the S/DR reaction for the Ni-Cu catalysts and the reference NiNiMgAl<sub>4</sub>\_Rh<sub>0.5</sub> one.

Although the effect of Cu was not comparable to the one obtained with the same amount of Rh in all the reaction conditions, especially for the lowest temperatures, the Cu promotion effect was clear also in terms of CO<sub>2</sub> conversion (Fig. 3.52).

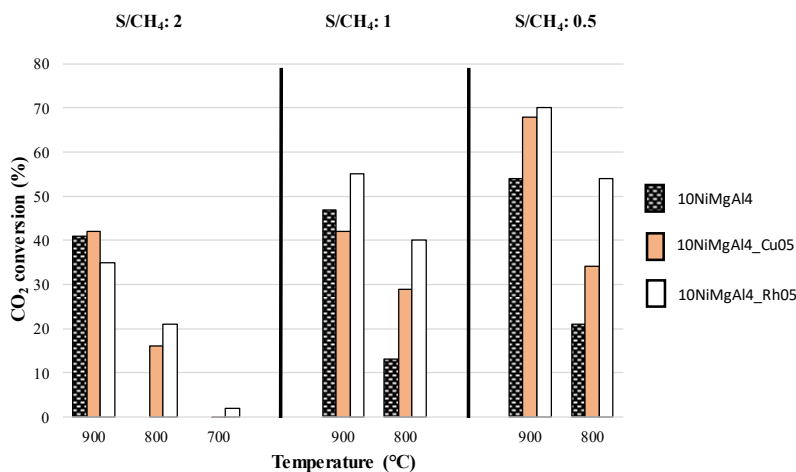


Figure 3.52. CO<sub>2</sub> conversion in the S/DR reaction for the Ni-Cu catalysts and the reference NiNiMgAl<sub>4</sub>\_Rh<sub>0.5</sub> one.

Although the trend was more variable, obvious improvements were obtained at low temperatures and S/CH<sub>4</sub> values, in which the increases of the catalytic activity were about +60 % (T = 800 °C and S/CH<sub>4</sub> = 0.5), +120 % (T = 800 °C and S/CH<sub>4</sub> = 1.0), with a small CO<sub>2</sub> conversion due to the DR reaction at 800 °C and with S/CH<sub>4</sub> = 2.0 (16 %). In line with the results obtained for the Rh-promoted catalysts, in which an increasing amount of noble metal enhanced the catalytic activity, a Cu-content of 2.0 wt.% was investigated to boost the catalyst performances. Surprisingly, the further addition of Cu had an

unexpected effect on the CB conversion, that was negatively affected with a dramatic decrease in terms of both CH<sub>4</sub> and CO<sub>2</sub> conversion values for all the reaction conditions.

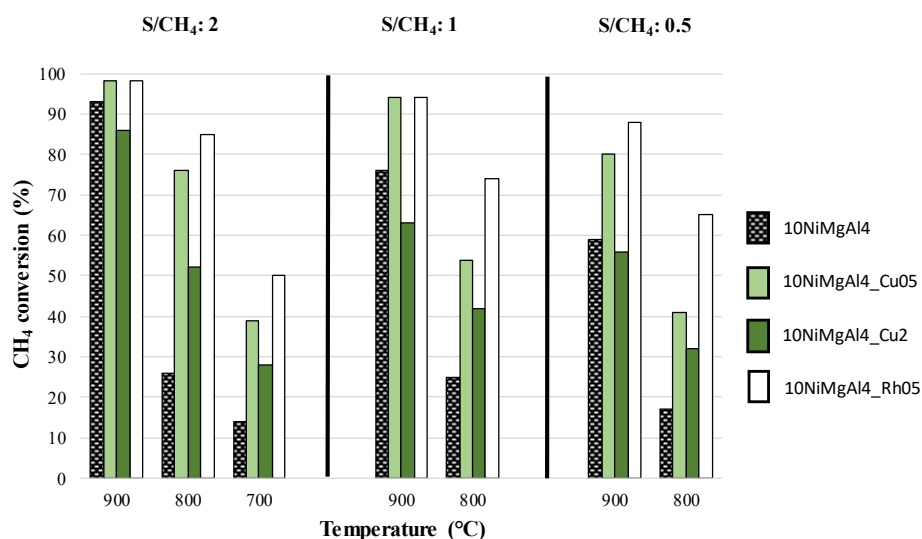


Figure 3.53. CH<sub>4</sub> conversion values for Ni-Cu catalysts and the unpromoted and 0.5 wt.% Rh-promoted catalysts.

The CH<sub>4</sub> conversion (Fig. 3.53) was particularly low at 900 °C for all the S/CH<sub>4</sub> ratios, where the 10NiMgAl<sub>4</sub>\_Cu<sub>2</sub> catalyst exhibited values below those detected for the unpromoted 10NiMgAl<sub>4</sub> sample.

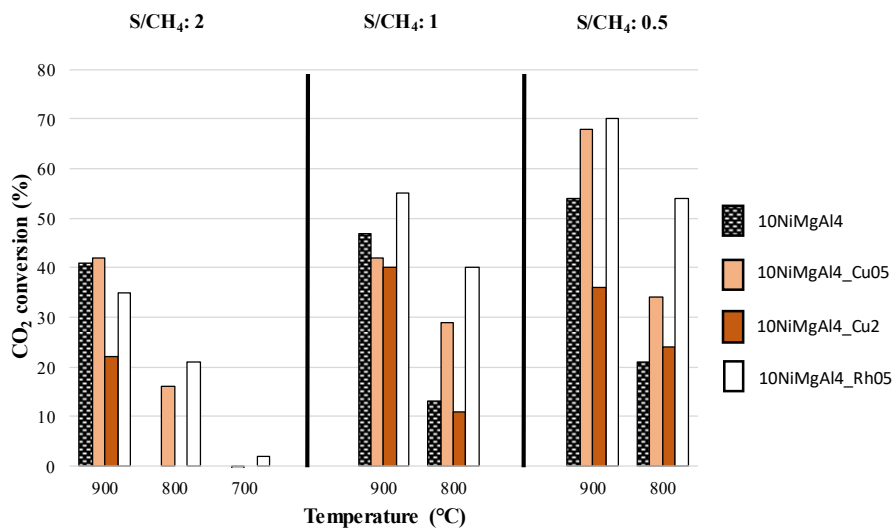


Figure 3.54. CO<sub>2</sub> conversion values for Ni-Cu catalysts and the unpromoted and 0.5 wt.% Rh-promoted catalysts.

The same behaviour was evidenced by the trend of the CO<sub>2</sub> conversions (Fig. 3.54), in which the activity of the 10NiMgAl<sub>4</sub>\_Cu<sub>2</sub> catalyst was always lower than that obtained with the un-promoted 10NiMgAl<sub>4</sub> catalyst. Moreover, the DR activity observed at 700 °C for the 10NiMgAl<sub>4</sub>\_Cu<sub>05</sub> catalyst totally disappeared and the calculated CO<sub>2</sub> conversion in this condition was negative, i.e. - 13% (value not reported in figure 3.54).

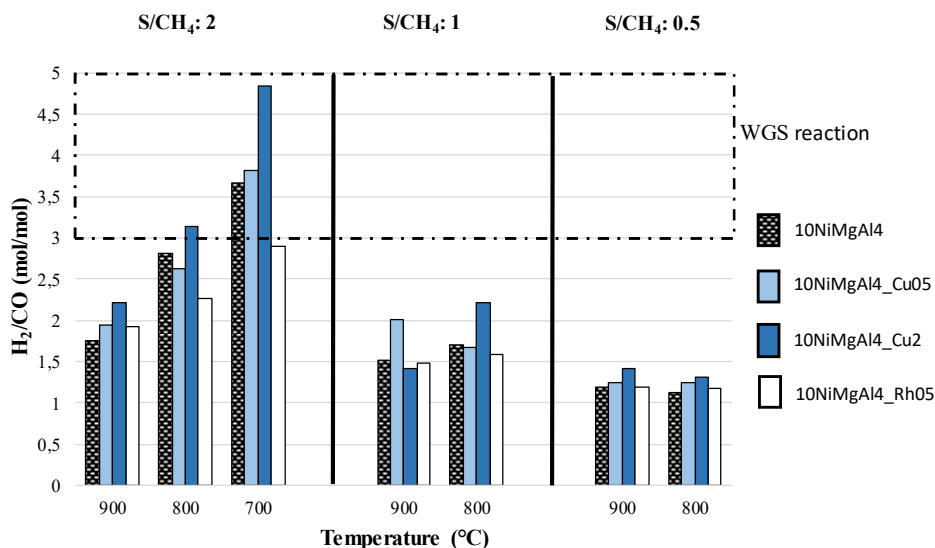


Figure 3.55. Comparison between the H<sub>2</sub>/CO molar ratio values in the outlet syngas observed for the Ni-Cu catalysts and the unpromoted and 0.5 wt.% Rh-promoted catalysts

From the H<sub>2</sub>/CO ratios of the outlet syngas (Fig. 3.55) it was possible to note that at 700 °C the ratios for the two Ni-Cu catalysts exceeded the value of 3, reaching a value near 5 for the 10NiMgAl<sub>4</sub>\_Cu<sub>2</sub> sample. This behaviour evidenced that a 2 wt.% of Cu favoured the WGS reaction, for which it is well known that Cu is an active phase [9,10], increasing the H<sub>2</sub>/CO ratio, but decreasing the CO<sub>2</sub> conversion and limiting the occurrence of the DR reaction in these conditions. The discrepancies observed in the catalytic activity can be explained by comparing the H<sub>2</sub>-TPR profiles of the Ni-Cu catalysts with those of the 10NiMgAl<sub>4</sub> and 10NiMgAl<sub>4</sub>\_Rh<sub>05</sub> samples (Fig. 3.56). The promotion by a 0.5 wt.% of Cu led to a strong increase of the intensity of the reduction peak without a significant lowering of its temperature (from 900 °C to 898 °C). At the same time, the symmetry of the profile increased with a shape comparable to that observed for the 10NiMgAl<sub>4</sub>\_Rh<sub>05</sub>

catalyst, that exhibited most active and well-dispersed metal particles on the catalyst surface.

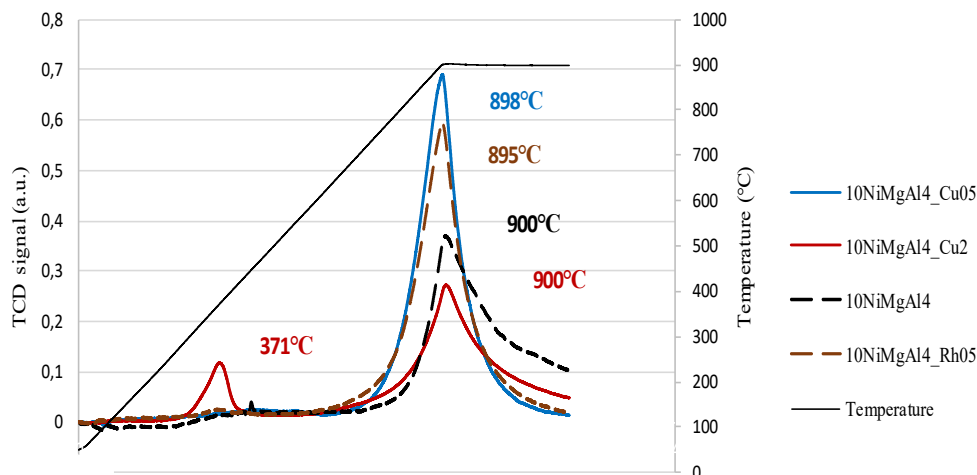


Figure 3.56. H<sub>2</sub>-TPR profiles of 10NiMgAl<sub>4</sub>\_Cu<sub>05</sub>, 10NiMgAl<sub>4</sub>\_Cu<sub>2</sub>, 10NiMgAl<sub>4</sub> and 10NiMgAl<sub>4</sub>\_Rh<sub>05</sub> catalysts.

A further addition of Cu lowered the catalyst reducibility, as the reduction peak at high temperature was broad and with an intensity lower than that registered for the unpromoted catalyst. In this case it was possible to observe a further broad reduction peak at about 371 °C, that can be attributed to the reduction of Cu<sup>2+</sup> ions weakly interacting with the support that can possibly cover the NiO particles, decreasing its reducibility. The benefits derived from the Cu promotion was thus visible only at low Cu-content and the relationship between the Ni-based catalysts reducibility and their activity in the S/DR reaction was confirmed. The stability of the catalysts was evaluated at the end of the catalytic tests, and the conversion values obtained (Fig. 3.57) showed losses of activity for both of the Ni-Cu catalysts, with a higher deactivation values in terms of CO<sub>2</sub> conversion.

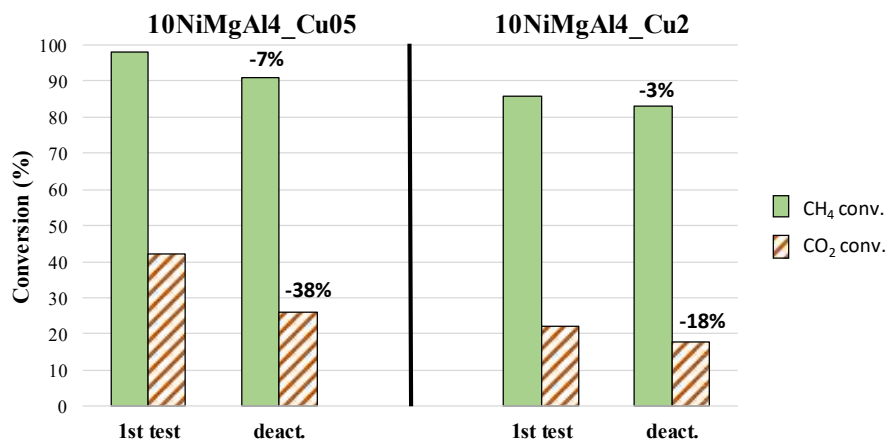


Figure 3.57. CH<sub>4</sub> and CO<sub>2</sub> conversion in the deactivation tests for the Ni-Cu catalysts.

The losses of specific surface area for the two Ni-Cu catalysts during reaction were negligible compared to that observed for the 10NiMgAl<sub>4</sub>\_Rh05 catalyst (Tab. 3.5), pointing out that the losses of activity were mainly related to the worst properties of the Ni-Cu alloy formed. It is noteworthy that the catalysts deactivation was again related to sintering phenomena occurring with time-on-stream.

Table 3.5. BET specific surface area of the catalysts before and after S/DR reaction.

Catalysts	SSA (m <sup>2</sup> /g) after calcination	SSA (m <sup>2</sup> /g) after reaction
10NiMgAl <sub>4</sub> _Rh05	95	29
10NiMgAl <sub>4</sub> _Cu05	74	65
10NiMgAl <sub>4</sub> _Cu2	56	40

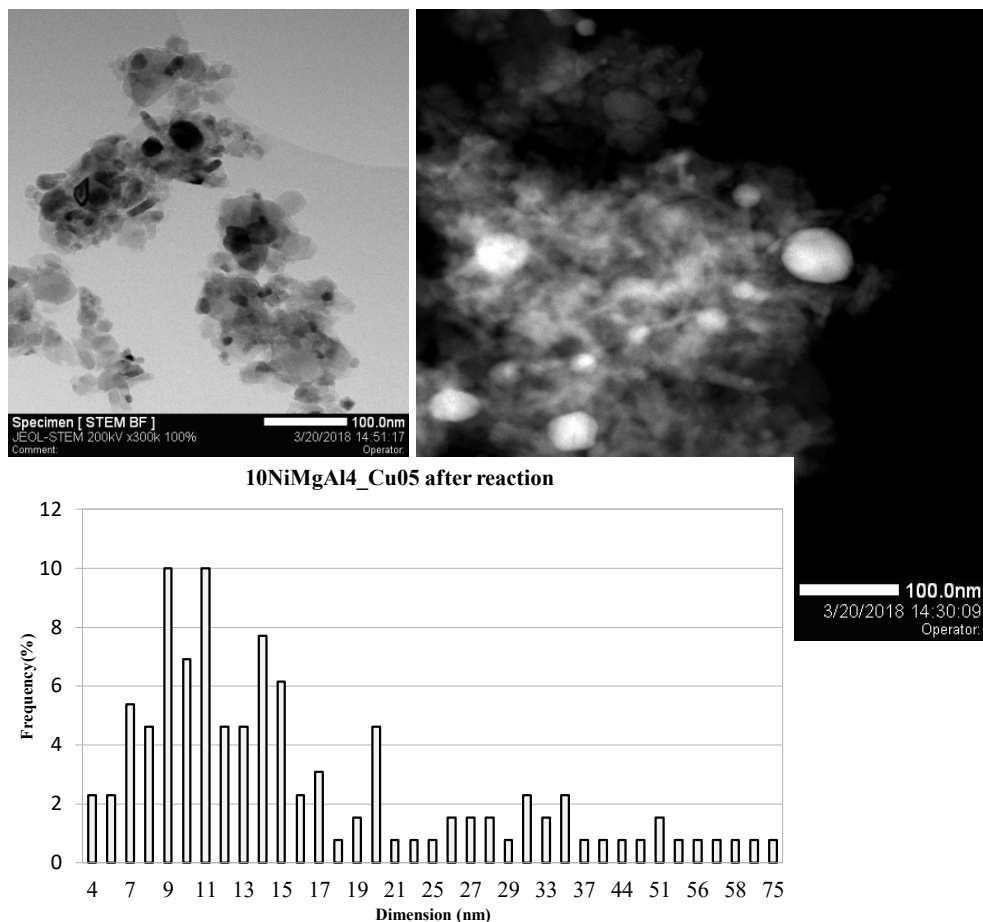


Figure 3.58. TEM, STEM-HAADF images and statistical distribution of the active phase after reaction for the 10NiMgAl4\_Cu05 catalyst.

The statistical distribution of the metal particles for the 10NiMgAl4\_Cu05 catalyst after reaction (Fig. 3.58) revealed a significant presence of particles with a diameter higher than 50 nm, together with a distribution of smaller nanoparticles with a diameter comprised in the 4-17 nm range. The average dimension was 18 nm, without any evidences of coke formation on the catalyst surface. The active phase distribution of the 10NiMgAl4\_Cu2 catalyst (Fig. 3.59) was broader, with an average diameter of 36 nm, and only a small content of particles in the 8-10 nm range. In this case the catalyst exhibited also a significant presence of large agglomerates, with a diameter up to 500 nm.

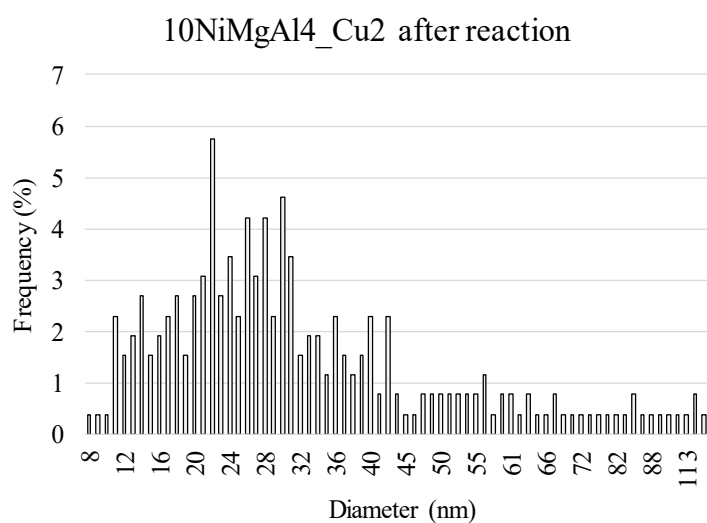
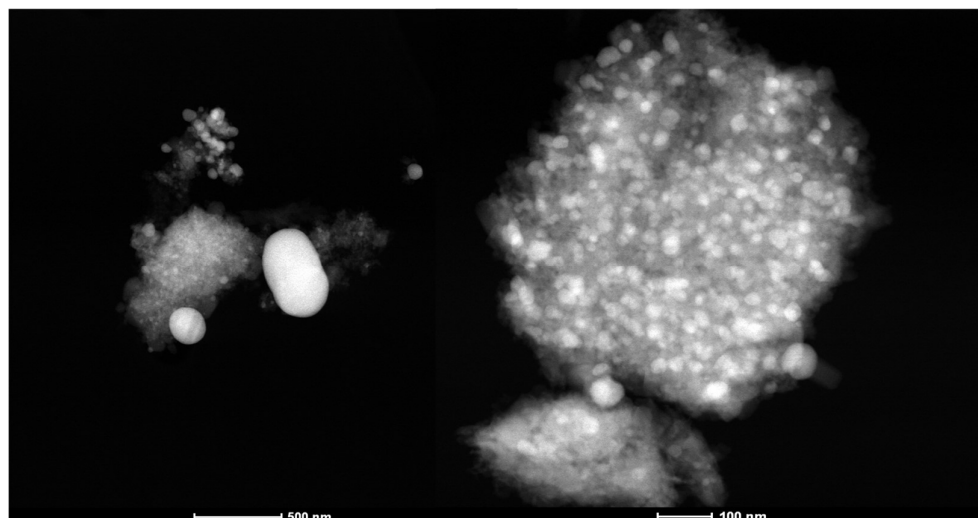


Figure 3.59. TEM, STEM-HAADF images and statistical distribution of the active phase after reaction for the 10NiMgAl4\_Cu2 catalyst.

From both EDX mapping and compositional analysis performed on the Cu-containing catalysts after reaction (Fig. 3.60), it was possible to confirm the formation of a Ni-Cu alloy, that formed the active phase in the catalysts. The trend of the metal ratio in the different particles was similar to that already observed for the Ni-Rh catalysts. Again, the Ni-amount increased with the particle size, while the Cu content was higher in the smaller nanoparticles (from 11 to 34 wt.% for particle sizes of 120 nm and 20 nm respectively).

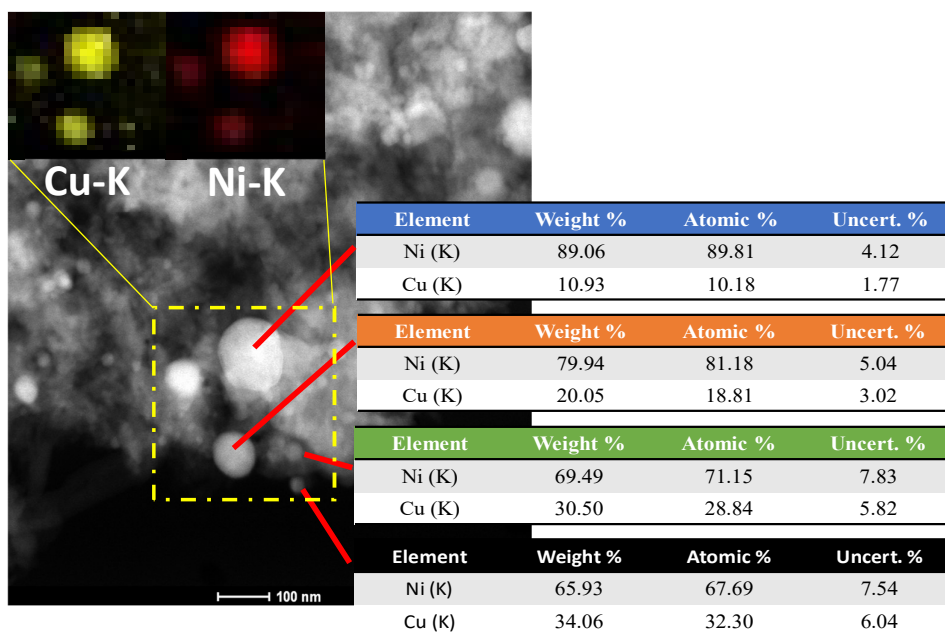


Figure 3.60. STEM-HAADF image, EDX maps (for Ni-K and Cu-K) and compositional analyses of different particles of the 10NiMgAl<sub>4</sub>\_Cu<sub>2</sub> catalyst after reaction.

Besides a higher tendency to agglomerate, the 10NiMgAl<sub>4</sub>\_Cu<sub>2</sub> catalyst suffered also the formation of carbon nanotubes on the surface, together with the presence of encapsulating carbon (Fig. 3.61) on the edge of the smallest nanoparticles, that probably contributed to the catalyst deactivation.

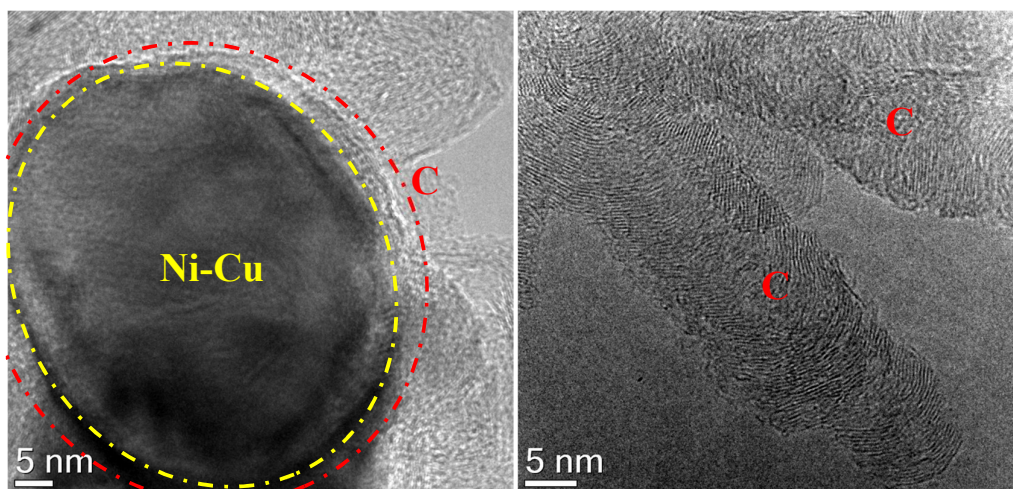


Figure 3.61. TEM images of the 10NiMgAl<sub>4</sub>\_Cu<sub>2</sub> catalyst after reaction. On the left: encapsulating carbon; on the right: carbon nanotubes on the catalyst surface.

### 3.5.2 Preliminary conclusions

The substitution of Cu leads to the formation of a Ni-Cu alloy on the surface of the catalysts during the reduction step. Even though not with the same extent of that observed with Rh, the presence of 0.5 wt.% of Cu, improves the catalyst activity and the dispersion of the active phase, increasing the catalyst reducibility and leading to more active nanoparticles. Divergently to that observed in the previous work, increasing the amount of Cu in the catalyst formulation, the active phase properties get worsened, the undesired WGS reaction being promoted and the catalyst becoming more prone to the phenomena that lead to its deactivation. This behaviour could be related to the fact that Cu, at high concentrations can suppress the activation of methane, possibly because of competitive adsorption of CH<sub>4</sub> and slow dissociation kinetics on Cu atoms [11]. Surface enrichment of copper due to low surface energy compared with nickel may also decrease the number of active Ni sites on the surface and affect activity for high copper loading. Although also in this case the alloy composition seems to drive the metal particles size, the sintering of the active phase occurs and becomes more obvious at high amounts of Cu in the catalyst formulation. This phenomenon is probably enhanced by the lower specific surface area exhibited by the two Ni-Cu catalyst after calcination, and by the high tendency of Copper to undergo sintering [12,13], that makes this specific alloy less stable at the high temperatures of reaction.

### 3.6.1 Ni-based catalysts obtained *via* surfactant-assisted-templating route

It is known that the specific surface area together with the porosity distribution of the catalyst play a determining role on its activity and stability during the time-on-stream. One of the key factors to achieve this result is the selection of appropriate preparation methods and compositions, which determine homogeneity at molecular level and specific textural/morphological properties. Several methods have been described for the preparation of mixed oxides catalysts, that range from the high temperature firing [14], high-energy milling [15] of a mixture of oxides or traditional sol/gel techniques [16]. The use of templating techniques for the synthesis of mixed oxides with specific porosity has opened new opportunities in the design of novel high-surface materials for catalytic applications, that show stable pore distributions also after calcination. With the aim to improve the textural, structural and chemical properties of the Ni-based catalysts used in the S/DR reaction, the synthesis of two catalysts by co-precipitation using a non-ionic surfactant was carried out, comparing the catalytic results with those obtained in the previous sections.

Two Ni-based catalysts were synthesized *via* surfactant-assisted-templating route, starting from the composition of the 10NiMgAl4 and 10NiMgAl4\_Rh003 catalysts and were named as follows:

10NiMgAl4\_PF (Ni: 10 wt.%, M<sup>2+</sup>/M<sup>3+</sup>: 4)

10NiMgAl4\_Rh003\_PF (Ni: 10 wt.%, Rh: 0.03 wt.%, M<sup>2+</sup>/M<sup>3+</sup>: 4)

The samples before and after calcination were characterized using XRD and ATR analyses to verify the crystal structure and the complete removal of the surfactant by washing the precipitated solid. The XRD patterns of the samples before and after calcination (Fig. 3.62) showed the formation of a HT phase by co-precipitation; after calcination at 900 °C for 6 h, the precursor evolved to a mixture of oxides, mainly MgO/NiO and a spinel phase containing Ni, Mg and Al, all with low crystallinity.

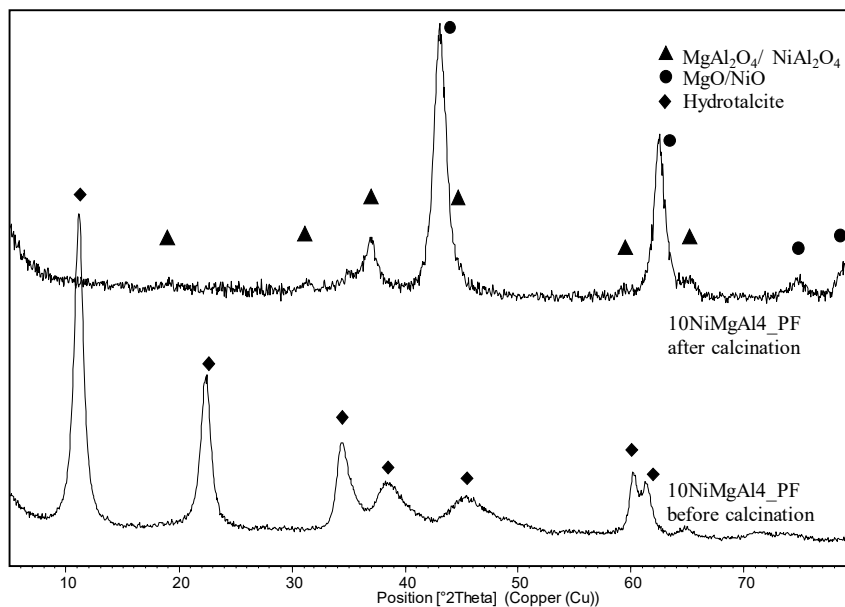


Figure 3.62. XRD patterns of the 10NiMgAl4\_PF catalyst before (dried) and after calcination.

The FT-ATR analyses performed on the fresh and calcined samples (Fig. 3.63) revealed the complete removal of the non-ionic surfactant used in the synthesis, without any evidence in the spectra of both calcined and dried precursors of the characteristic bands of the dried surfactant (black line)

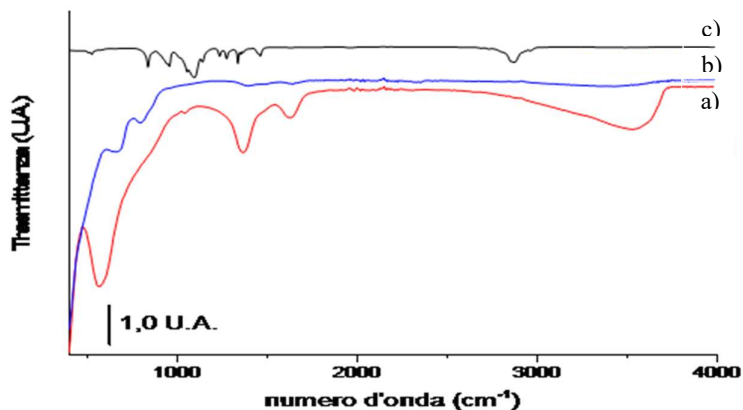


Figure 3.63. ATR spectra of: a) 10NiMgAl4\_PF HT precursor after drying; b) after calcination at 900 °C for 6 h; c) non-ionic surfactant used in the synthesis.

From the BJH analyses conducted on the 10NiMgAl4\_PF sample before and after calcination, it was possible to investigate its texture and properties. As shown in Figure

3.64 the new catalyst showed that the use of the surfactant gave rise to an important change in the pore size distribution compared to that of the reference 10NiMgAl4 catalyst.

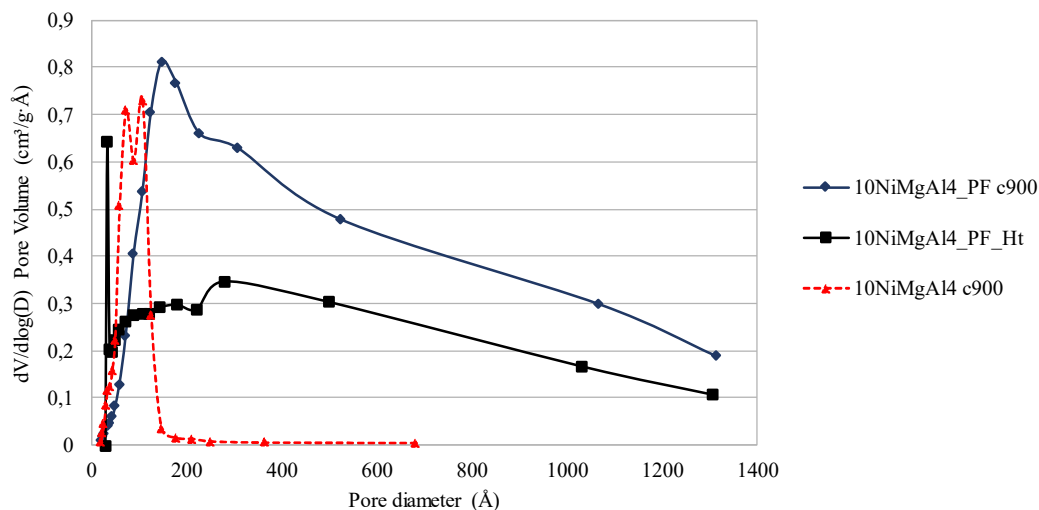


Figure 3.64. Pore size distribution of the 10NiMgAl4\_PF HT sample dried (Ht) or calcined (c900) and of the reference 10NiMgAl4 catalyst.

The different types of synthesis shifted the pore size distribution to higher sizes for both precursor (dried) and calcined catalyst. In addition, the significant presence of macropores ( $d > 500 \text{ \AA}$ ) remained unchanged after calcination, although an increase in the pore volume was observed due to the partial collapse of the meso- and micro- pores during the calcination. Notwithstanding the presence of a high amount of large pores, their total volume was approximatively 3 times higher than that observed for the 10NiMgAl4 catalyst. This feature assured a specific surface area value higher than that observed for the reference 10NiMgAl4 while only a small decrease of the crystallite sizes of the spinel phase was observed for the 10NiMgAl4\_PF c900 catalyst. (Tab. 3.6).

Table 3.6. Specific surface area and pore volume for dried and calcined samples and crystallite sizes calculated through the Scherrer equation after calcination of a) MgO/NiO and b) Spinel phase.

Sample	SSA (m <sup>2</sup> /g)	Pore volume (cm <sup>3</sup> /g)	Average pore size (Å)	D (nm)
10NiMgAl4 c900	102	0.28	71	<sup>a</sup> 11, <sup>b</sup> 13
10NiMgAl4_PF c900	123	0.75	243	<sup>a</sup> 11, <sup>b</sup> 11
10NiMgAl4_PF HT	88	0.47	114	7

This result may be attributed to a high amount of stable meso- and macro-porosities in the 10NiMgAl<sub>4</sub>\_PF sample, that improved the specific area of the catalyst and was little influenced by the calcination. The SEM images of the solids (Fig. 3.65) showed that the morphology of the 10NiMgAl<sub>4</sub>\_PF sample was “foamy” and practically unchanged after calcination, while the calcined reference 10NiMgAl<sub>4</sub> catalyst revealed a homogenous flat surface.

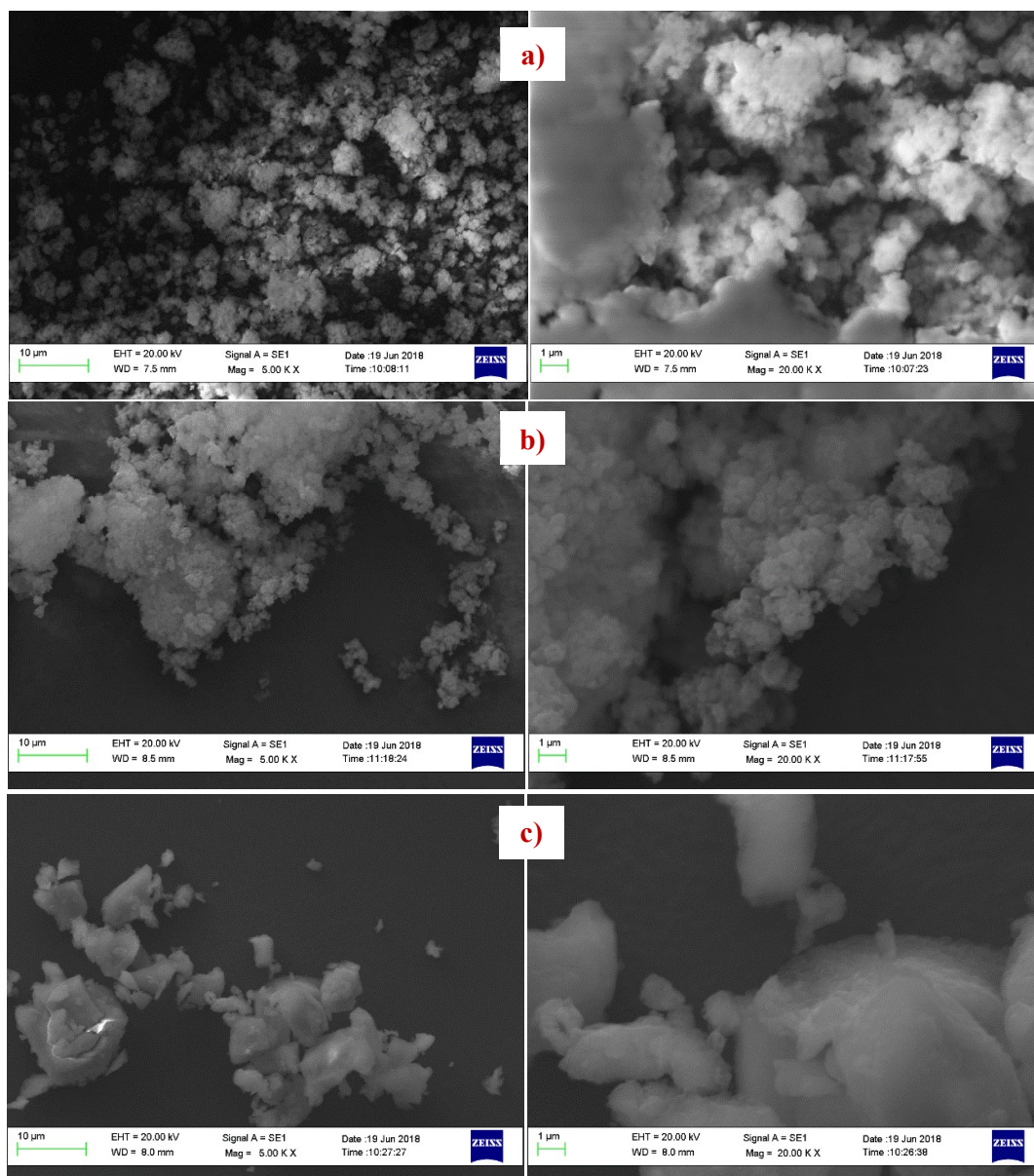


Figure 3.65. SEM images of: a) dried 10NiMgAl<sub>4</sub>\_PF HT precursor, b) calcined 10NiMgAl<sub>4</sub>\_PF c900 sample; and c) reference 10NiMgAl<sub>4</sub> catalyst after calcination.

The TEM observations of the catalyst after reduction (Fig. 3.66) confirmed that a different morphology was present also at nanoscale. The reduced 10NiMgAl4\_PF catalyst showed a high number of nanoparticles well distributed on the surface, together with the presence of nanorod-structures (never observed before) with a length up to 100 nm, widely distributed on the sample. The statistical distribution of the Ni<sup>0</sup> particles was centred around 9 nm (average diameter) and comprised between 4-18 nm. The dispersion of the active phase was more homogeneous than that reported before for the 10NiMgAl4 catalyst, that exhibited a larger average diameter of 16 nm.

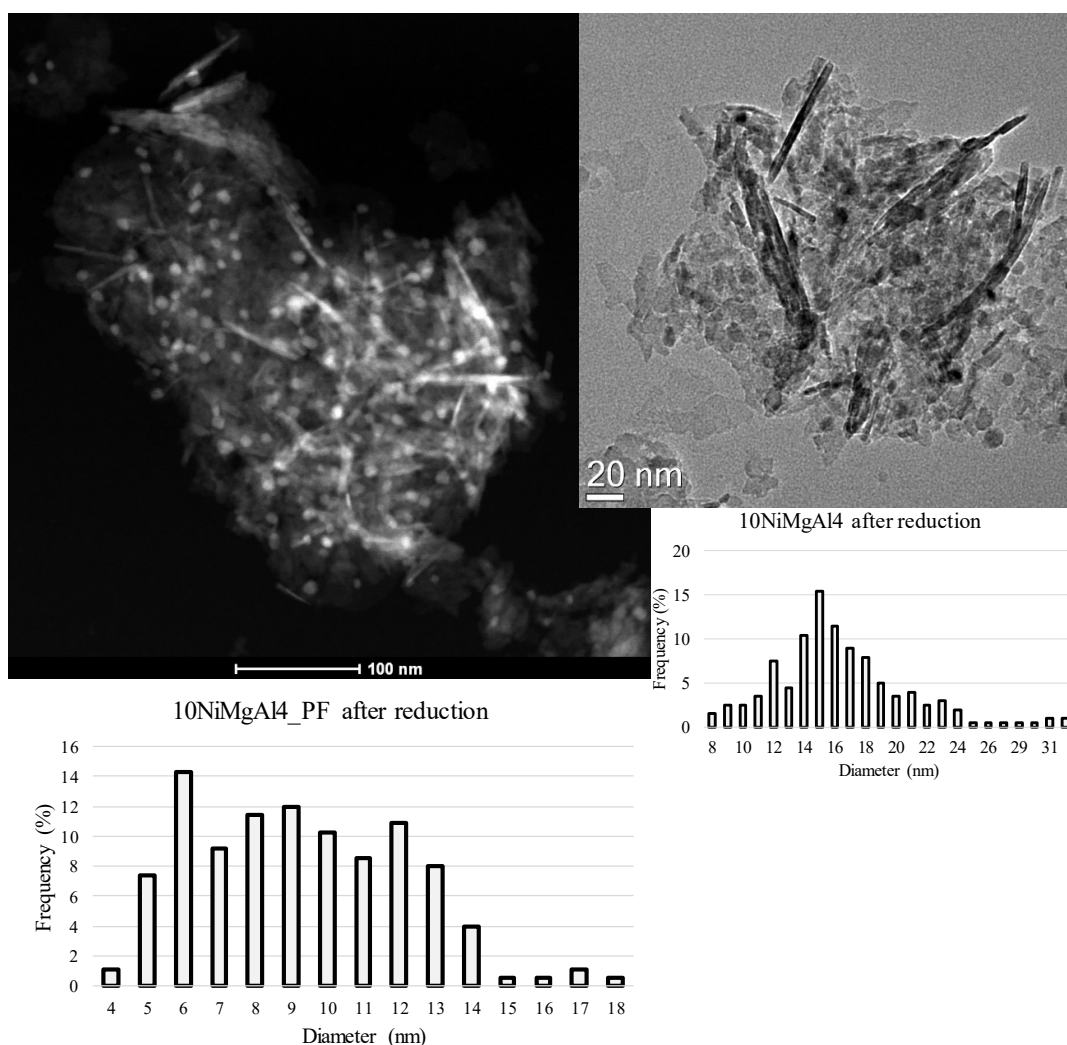


Figure 3.66. TEM and STEM-HAADF images of the calcined 10NiMgAl4\_PF sample after reduction and metal particles distribution. On the right, the active phase distribution of the 10NiMgAl4 catalyst after reduction.

The improvement obtained in terms of active phase dispersion and textural properties positively reflected on the catalytic performance of the catalyst (Fig. 3.67), that showed high CB conversion values, with impressive enhancements especially in terms of CH<sub>4</sub> conversion, in comparison to those obtained for the 10NiMgAl<sub>4</sub> catalyst. The CH<sub>4</sub> conversion values improved more than 100 % at 800 and 700 °C, regardless of the S/CH<sub>4</sub> value in the fed stream. Although the enhancements were lower in terms of CO<sub>2</sub> conversion values, best results were obtained at 800 °C where the catalyst exhibited the presence of the DR reaction even at S/CH<sub>4</sub> = 2 (v/v). The deactivation tests revealed that the stability of the catalyst was improved only in terms of CH<sub>4</sub> conversion value, that showed a low loss of activity ( $\approx$  3 %), while a higher deactivation was observed for the CO<sub>2</sub> conversion value (-59%).

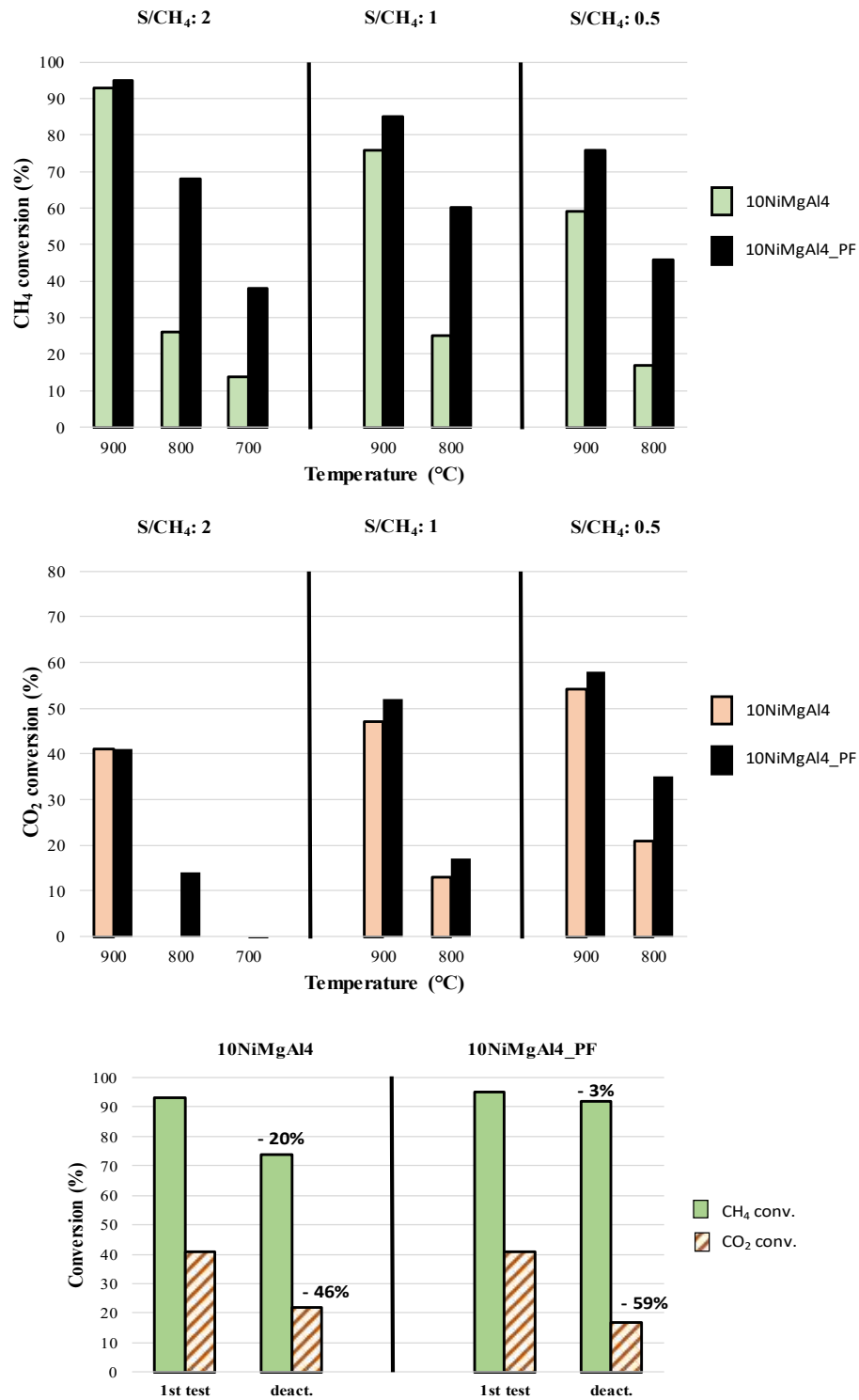


Figure 3.67. CH<sub>4</sub> and CO<sub>2</sub> conversion values for the 10NiMgAl<sub>4</sub> and 10NiMgAl<sub>4</sub>\_PF catalyst. At the bottom, the results obtained in the deactivation tests.

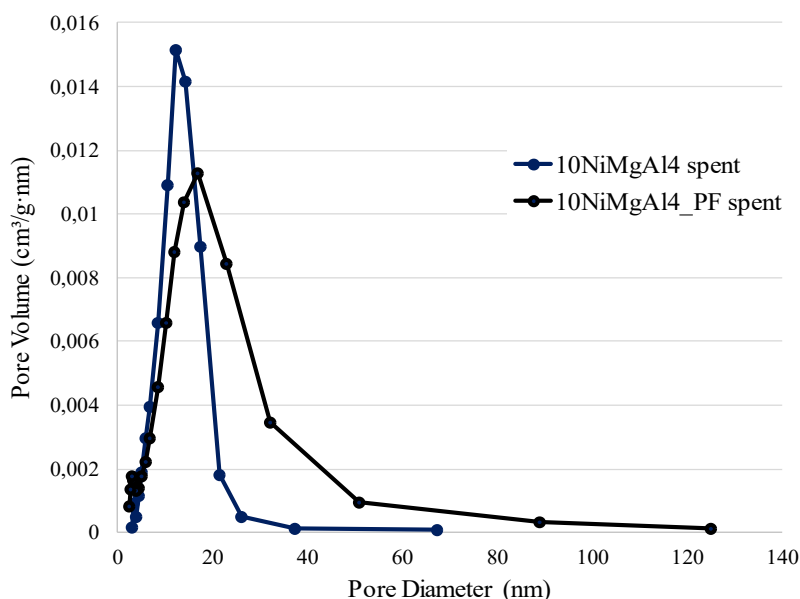


Figure 3.68. Pore size distribution for the 10NiMgAl4 and 10NiMgAl4\_PF catalysts after reaction.

The distribution of the pores after reaction for both 10NiMgAl4\_PF and 10NiMgAl4 catalysts (Fig. 3.68) was affected by the time-on-stream. A significant loss of the specific surface area was detected, comparable to that determined for the 10NiMgAl4 spent catalyst (Table 3.7). The higher value of the specific area for the 10NiMgAl4\_PF spent catalyst was accompanied by a larger pore size and a smaller crystallite sizes, pointing out its enhanced stability in the harsh S/DR reaction conditions.

Table 3.7. Results obtained from the BJH pore analysis of the two catalysts after calcination or reaction and crystallite sizes calculated through the Scherrer equation of a) MgO/NiO and b) Spinel phase after reaction.

Catalysts	Calcined			Spent			
	SSA (m <sup>2</sup> /g)	Pore volume (cm <sup>3</sup> /g)	Average pore size (Å)	SSA (m <sup>2</sup> /g)	Pore volume (cm <sup>3</sup> /g)	Average pore size (Å)	D (nm)
10NiMgAl4	102	0.28	71	38	0.16	128	<sup>a</sup> 26, <sup>b</sup> 32
10NiMgAl4_PF	123	0.75	243	46	0.30	188	<sup>a</sup> 18, <sup>b</sup> 20

With the aim to further improve the catalytic performance of the catalyst, a small amount of Rh (0.03 wt.%) was added in the catalyst formulation. Its presence did not significantly change the textural properties of the catalyst, and the 10NiMgAl4\_Rh003\_PF sample showed the same wide pore size distribution observed before. From the H<sub>2</sub>-TPR analysis it was found that also in this case, the presence of Rh increased the reducibility of the

catalyst, but unlike to that previously reported, the formation of the Ni-Rh alloy (confirmed by EDX analyses) did not tighten the statistical distribution of the metal particles to a lower average diameter (Fig. 3.69).

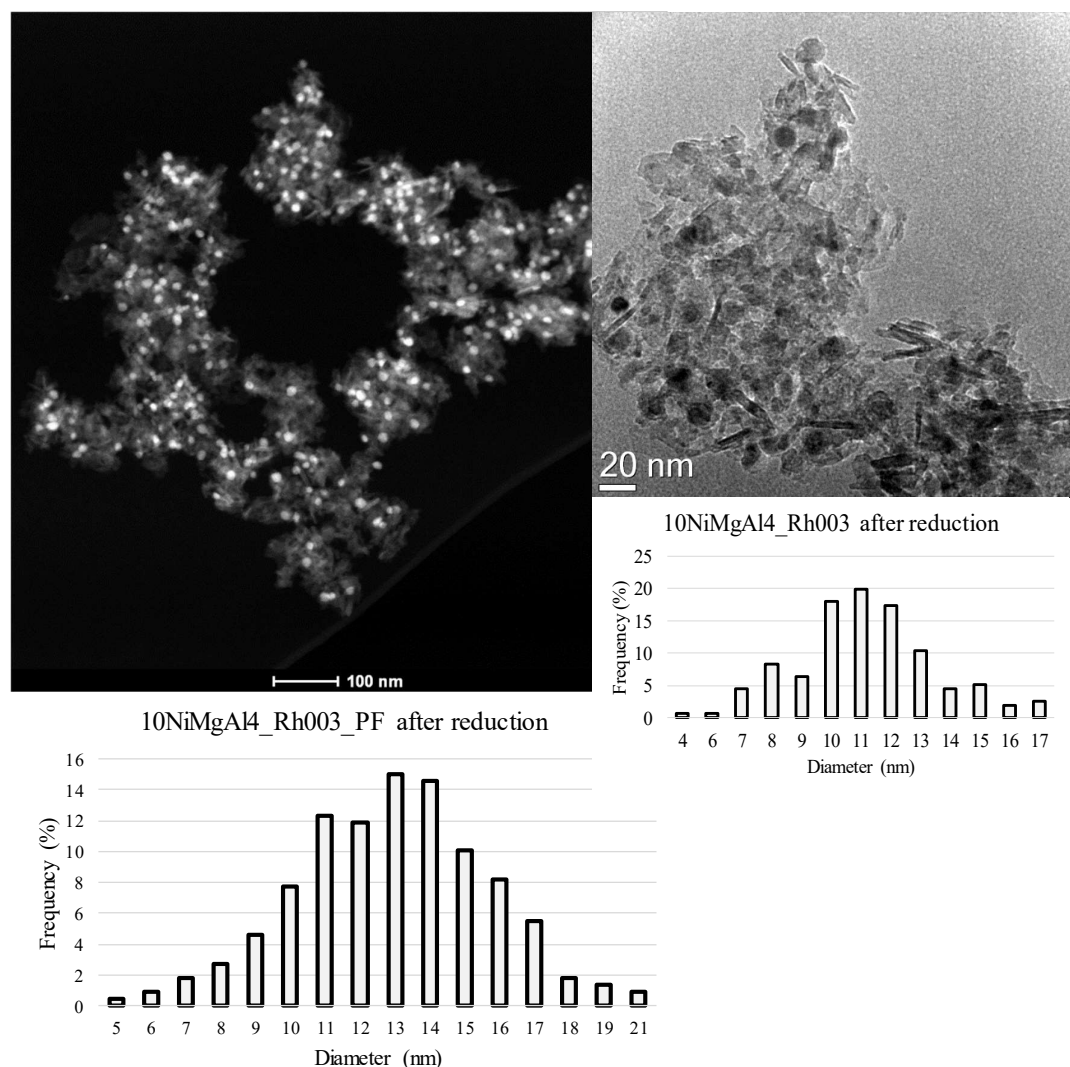


Figure 3.69. TEM and STEM-HAADF images of 10NiMgAl4\_Rh003\_PF after reduction and its metal particle distribution. On the right, the active phase distribution of the 10NiMgAl4\_Rh003 catalyst after reduction.

The dispersion of the active phase after reduction was centred around a value of 13 nm, and the particle diameters comprised in the range 5-21 nm, showing a worsening of the distribution if compared to that previously observed for the reduced 10NiMgAl4\_Rh003 catalyst. Also in this case, the presence of nanorods was detected, confirming the relationship between the formation of these structures and the characteristic porosities of the catalyst. The results obtained from the catalytic tests are presented in figure 3.70, in which the values obtained are compared to those observed for the 10NiMgAl4\_Rh05

catalyst. Notwithstanding the slight decrease in the active phase dispersion, the performances of the catalyst were further improved by the presence of Rh in terms of both CH<sub>4</sub> and CO<sub>2</sub> conversion values in all the reaction condition tested.

The activity obtained was higher than that exhibited by the catalyst with the same Rh-amount obtained by more traditional co-precipitation (10NiMgAl<sub>4</sub>\_Rh003, not reported in this paragraph). In this case, an important boost of the CO<sub>2</sub> conversion was observed especially at low temperature and S/CH<sub>4</sub> ratio value, such as demonstrated by the impressive enhancement obtained at 800 °C, with a S/CH<sub>4</sub> = 1 value, attributable to the presence of Rh in the catalyst formulation. In many conditions, the performances were comparable or slightly lower to those of the 10NiMgAl<sub>4</sub>\_Rh05 catalyst, showing the improvement of the catalyst properties attributable to the new synthesis method.

On the contrary, the H<sub>2</sub>/CO ratio values of the outlet stream were not significantly affected by both the synthesis method and the presence of Rh, resulting in very similar results to those obtained for the catalysts tested before. In conclusion, as in the case of the 10NiMgAl<sub>4</sub>\_Rh05 catalyst, the 10NiMgAl<sub>4</sub>\_Rh003\_PF sample did not show any significant deactivation during the time-on-stream, evidencing that the different textural properties of the catalyst boosted the catalytic performances. The presence in the catalyst structure of macro-pores together with a higher amount of meso-porosities, may enhance the diffusion of the reagents to the active phase, improving its stability in the S/DR conditions.

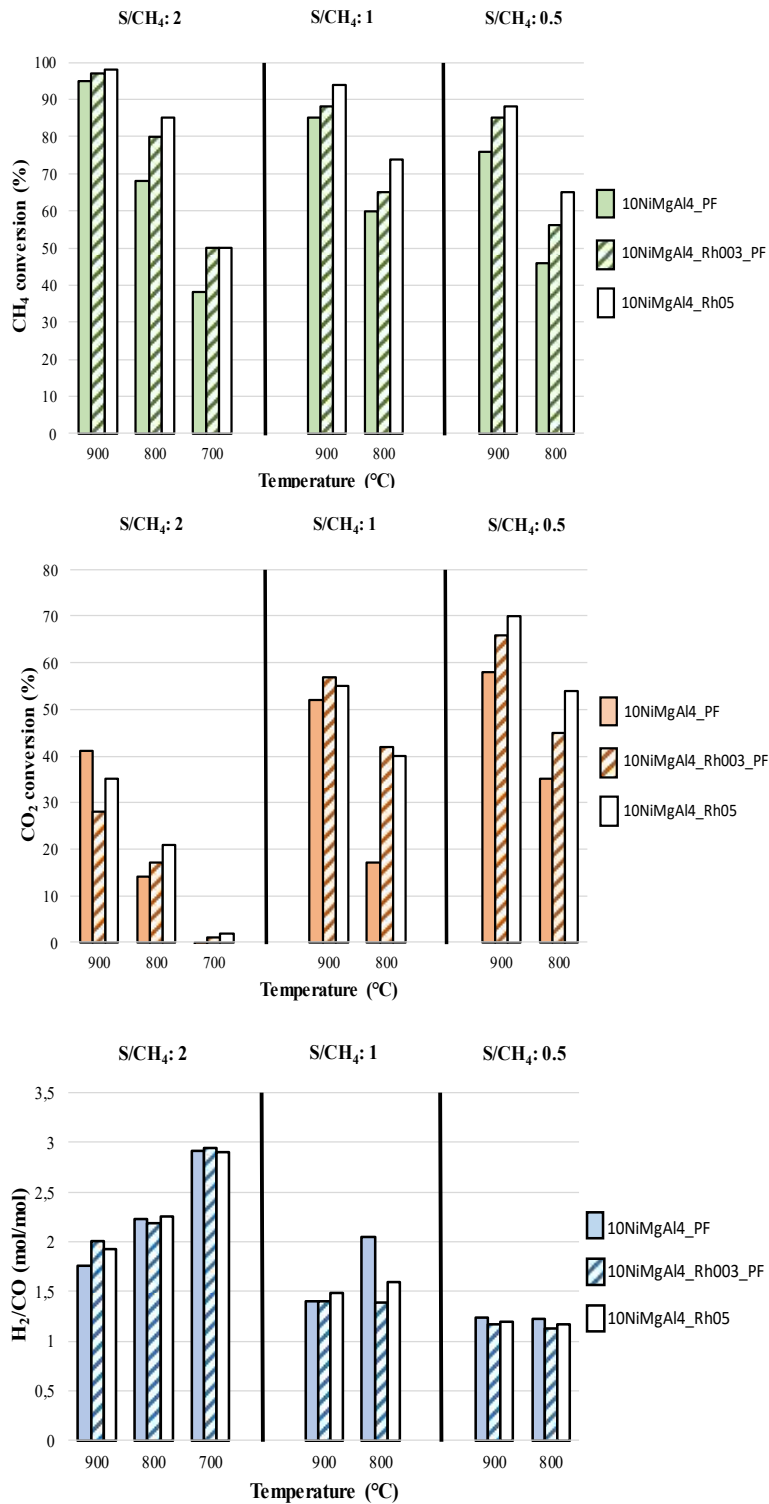


Figure 3.70. Catalytic activity obtained for the 10NiMgAl<sub>4</sub>\_PF, 10NiMgAl<sub>4</sub>\_Rh003\_PF and 10NiMgAl<sub>4</sub>\_Rh05 catalysts in terms of CH<sub>4</sub> and CO<sub>2</sub> conversion values and H<sub>2</sub>/CO molar ratio in the outlet syngas.

### 3.6.2 Preliminary conclusions

The co-precipitation *via* surfactant-assisted-templating route was successfully carried out obtaining catalysts with improved textural and morphological properties. The presence of the non-ionic surfactant, removed during the washing of the HT precursor, led to a solid that exhibited a high surface area together with an improved amount of meso- and macropores. These typical textures favoured the CB conversion, especially in terms of CH<sub>4</sub> conversion, improving the dispersion of the active phase and the stability of the catalyst. The formation of the Ni-Rh alloy during the catalyst reduction, further improved the CO<sub>2</sub> conversion in the S/DR conditions, in agreement with the results previously obtained. In addition, at the same reaction conditions, the specific properties of the new support increased the promotion effect of Rh in the reaction, allowing to decrease its amount in the formulation, lowering the cost associated to a large-scale production of this catalyst type.

### 3.7.1 Increase of the H<sub>2</sub> production from clean biogas by the water gas shift (WGS) reaction.

In the international energetic scenery, the H<sub>2</sub> market plays a key role. Considering the huge amount of H<sub>2</sub> consumed in the industrial applications, alone or together with different amounts of CO to form different synthesis gas formulations, it appears obvious that the optimization of the existing processes is fundamental from both the economic and environmental point of view.

Starting from the SR outlet stream, that currently represents the main way to produce H<sub>2</sub>, the role of the WGS reaction remains crucial. It allows to tune the H<sub>2</sub>/CO ratio or to improve the production of pure H<sub>2</sub> as a function of the catalyst formulation and reaction conditions. One possible application of the CB reforming is the production of H<sub>2</sub> for the chemical or energetic markets (i.e. to feed Solid Oxide Fuel Cells or SOFC). Starting from this premise, the present chapter will be focused on the application of the WGS reaction to the outlet stream of the S/DR reactor operating in the conditions favourable to pure H<sub>2</sub> production (T = 900 °C and S/CH<sub>4</sub> = 2 v/v). The aim is to evaluate the feasibility of the overall process, optimizing the reaction conditions and the amount of steam needed to valorise the outlet stream, having the following molar composition, expressed as dry gas:

CO: 28.7%, CH<sub>4</sub>: 0.6%, CO<sub>2</sub>: 11.7%, H<sub>2</sub>: 59.0%

This stream is processed in a WGS reactor reacting with steam to increase the H<sub>2</sub>/CO ratio of the outlet syngas:



Based on the calculation of the unreacted steam in the S/DR reactor, the Steam to Dry Gas ratio (S/DG) of the feed to the WGS reactor is 0.29 (v/v) as shown in the schematic representation of the integrated process (Fig. 3.71).

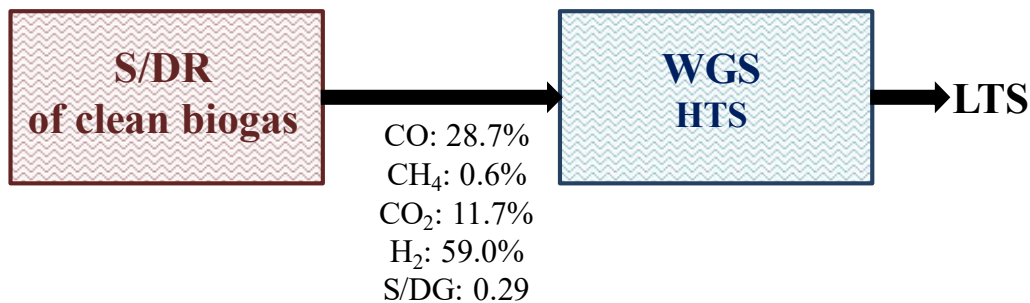


Figure 3.71. Schematic representation of the integrated S/DR-WGS process.

At first, the WGS process was tested at high temperature (High Temperature Shift or HTS), using a Cu/Zn/Al/Ga catalyst recently patented by our research group [17]. The catalyst was obtained by calcination of a HT precursor (550 °C for 6 h) synthesized by co-precipitation, followed by reduction in the plant. The XRD patterns of the calcined sample (Fig. 3.72) showed that the final catalyst (ZAC041Ga50) was composed by a ZnO-CuO mixed oxide and a Zn-Al spinel phase containing also Cu. The presence of a small amount of Ga in the formulation improved the properties of the catalyst, increasing the dispersion of the Cu<sup>0</sup> nanoparticles and stabilizing the active phase through the formation of a CuGa<sub>2</sub>O<sub>4</sub> phase, that strongly smoothed the catalyst deactivation [18].

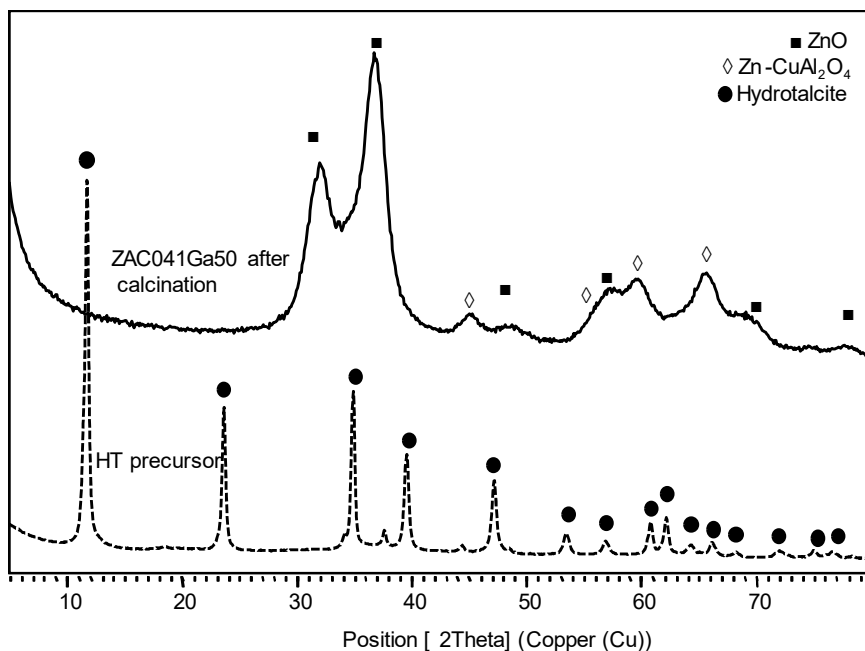


Figure 3.72. XRD patterns of the ZAC041Ga50 catalyst before and after calcination at 550 °C for 6 h.

Before the catalytic tests, the compositions of the outlet WGS stream at the thermodynamic equilibrium were calculated as a function of the operating temperature, comparing the results to those obtainable by the HTS reaction on a H<sub>2</sub>-rich stream typically produced by the SR of natural gas, having the following molar composition:

CO: 16.8%, CH<sub>4</sub>: 4.1%, CO<sub>2</sub>: 4.1%, H<sub>2</sub>: 75.0%, S/DG: 0.55 v/v

As it is possible to observe in Table 3.8 the outlet concentrations of the exit stream were greatly influenced by the composition of the reactant feed.

Table 3.8. Outlet concentration of the HTS-WGS stream at the thermodynamic equilibrium as a function of the feed composition and reaction temperature.

Feed type	Outlet concentrations (molar percentages) at increasing temperature			
		350°C	400°C	450°C
<b>S/DR of clean biogas.</b> S/DG: 0.29 v/v H <sub>2</sub> /CO: 2.06 v/v	H <sub>2</sub>	64.2	63.4	62.6
	CO	<b>9.3</b>	<b>11.7</b>	<b>14.2</b>
	CO <sub>2</sub>	25.9	24.3	22.6
	CH <sub>4</sub>	0.5	0.5	0.6
	H <sub>2</sub> /CO	<b>6.9</b>	<b>5.4</b>	<b>4.4</b>
<b>SR of natural gas.</b> S/DG: 0.55 v/v H <sub>2</sub> /CO: 4.46 v/v	H <sub>2</sub>	78.2	78.0	77.7
	CO	<b>1.8</b>	<b>2.8</b>	<b>4.0</b>
	CO <sub>2</sub>	16.4	15.6	14.6
	CH <sub>4</sub>	3.6	3.6	3.7
	H <sub>2</sub> /CO	<b>43.4</b>	<b>27.7</b>	<b>19.3</b>

The CO conversion at the thermodynamic equilibrium decreased with the temperature, increasing the CO content in the WGS outlet stream. The upgrading of the stream produced from the S/DR of CB is more difficult and produces, in these conditions, less H<sub>2</sub> than the values obtained by the WGS reaction of the H<sub>2</sub>-rich stream produced in the industrial SR processes. The catalytic tests were carried out at a pressure of 15 bar, with a S/DG = 0.29 v/v, increasing the weight hourly space velocity (WHSV) values and the reaction temperature. The deactivation of the catalyst was evaluated repeating the test at 350 °C (WHSV = 8200 ml/(h·g<sub>cat</sub>)) at the end of the experiment cycles.

The catalytic results obtained for the ZAC041Ga50 sample in these conditions (Fig. 3.73) confirmed the trend observed in the calculations of the thermodynamic equilibria discussed above. The CO conversion value decreased increasing the reaction temperature. It is improved by the lower WHSV values tested. The low equilibrium conversion values limited the H<sub>2</sub> production, and although the catalyst reached activities near to the equilibrium conversion values regardless of the reaction conditions, the productivity of the process was low, and the catalyst showed a deactivation in terms of loss of CO conversion of -36%, that evidenced its instability in these harsh reaction conditions.

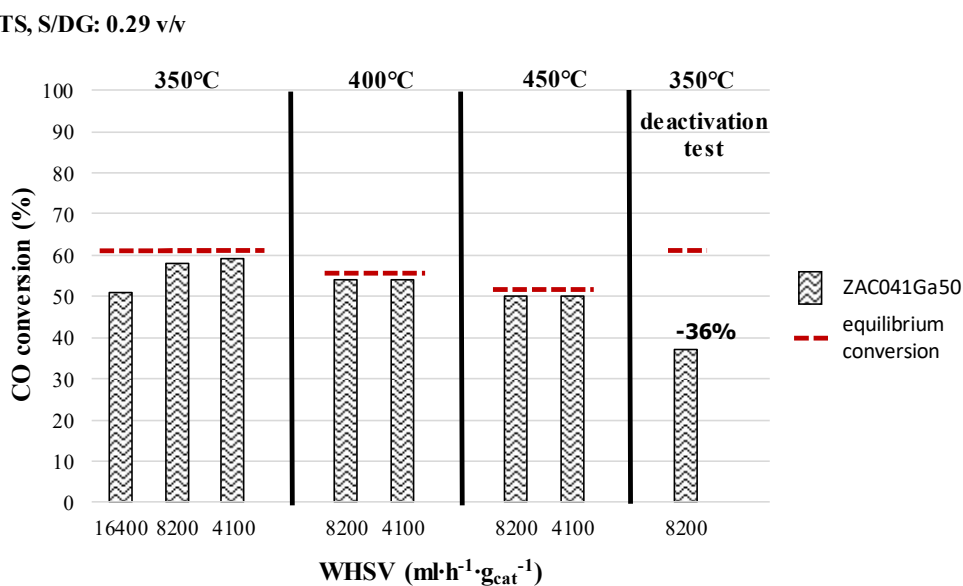


Figure 3.73. CO conversions at different temperatures as a function of the WHSV value for the ZAC041Ga50 catalyst in the HTS reaction (S/DG = 0.29)

One possible solution to overcome the thermodynamic limitations of the process, is the addition of a further amount of steam between the S/DR and the WGS process (Fig. 3.74). If the S/DG is increased to a value of 0.55 v/v, the equilibrium conversion values at the different temperatures increase, leading to a higher H<sub>2</sub>/CO molar ratio in the outlet WGS stream, with an enhancement of the H<sub>2</sub> production (Tab. 3.9).

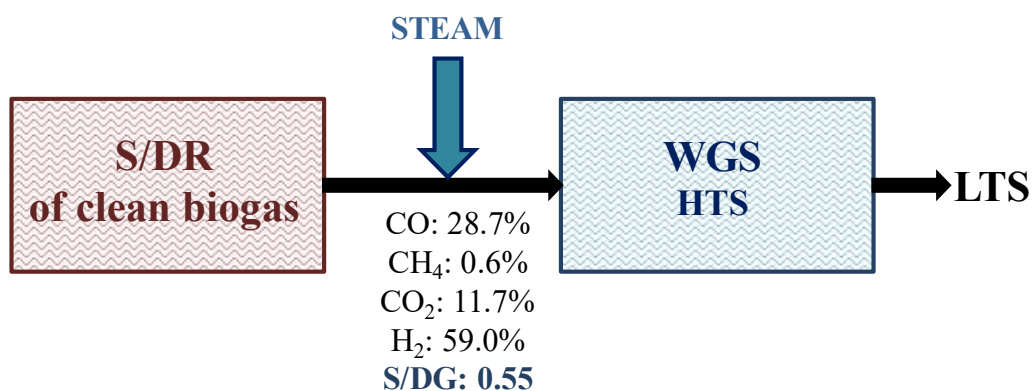


Figure 3.74. Schematic representation of the integrated S/DR-WGS process, with a further addition of steam between the two reactors.

Table 3.9. Outlet concentrations as a function of the temperature for the HTS streams at the thermodynamic equilibrium for different S/DG values and reaction temperatures.

Feed type		Outlet concentrations (mol.%) at increasing T		
		350°C	400°C	450°C
<b>S/DR of clean biogas.</b> <b>S/DG: 0.29 v/v</b> <b>H<sub>2</sub>/CO: 2.06 v/v</b>	H <sub>2</sub>	64.2	63.4	62.6
	CO	<b>9.3</b>	<b>11.7</b>	<b>14.2</b>
	CO <sub>2</sub>	25.9	24.3	22.6
	CH <sub>4</sub>	0.5	0.5	0.6
	H <sub>2</sub> /CO	<b>6.9</b>	<b>5.4</b>	<b>4.4</b>
<b>S/DR of clean biogas.</b> <b>S/DG: 0.55 v/v</b> <b>H<sub>2</sub>/CO: 2.06 v/v</b>	H <sub>2</sub>	66	65.3	64.6
	CO	<b>3.9</b>	<b>5.9</b>	<b>8.0</b>
	CO <sub>2</sub>	29.6	28.3	26.8
	CH <sub>4</sub>	0.5	0.5	0.5
	H <sub>2</sub> /CO	<b>16.9</b>	<b>11.1</b>	<b>8.1</b>

The catalytic tests carried out with the ZAC041Ga50 catalyst using a S/DG value of 0.55 v/v (Fig. 3.75), showed an improved activity of the catalyst, that reached CO conversion values near to the equilibrium values, influenced by the WHSV only at 350 °C, with CO conversion values comprised between 72 and 82 %.

HTS, S/DG: 0.55 v/v

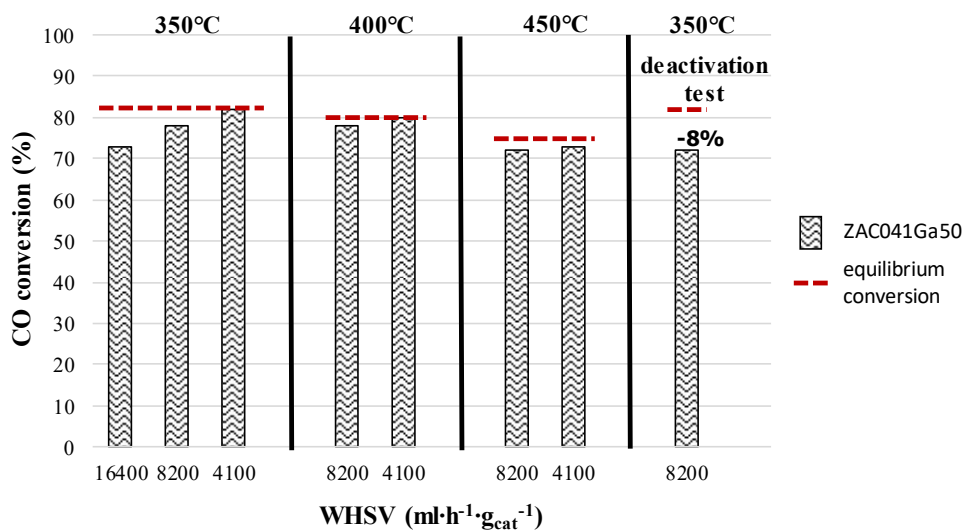


Figure 3.75. CO conversion at different temperatures as a function of the WHSV value for the ZAC041Ga50 catalyst in the HTS reaction (S/DG = 0.55)

Moreover, in these conditions, the deactivation of the catalyst decreased to about 8 %. The XRD pattern of spent catalysts (Fig. 3.76) showed a higher crystallinity, but the presence of Cu<sup>0</sup> was not detected evidencing a good dispersion of the active phase at the catalyst surface.

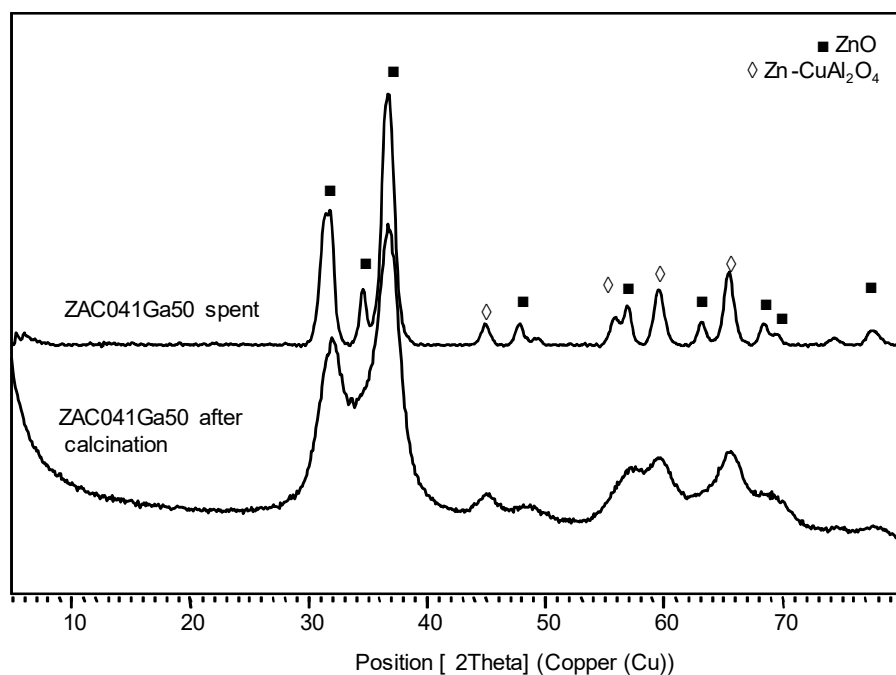


Figure 3.76. XRD patterns of the ZAC041Ga50 catalyst after calcination and reaction in HTS conditions.

In agreement with the results obtained by the XRD analysis, the specific surface area of the catalyst decreased after reaction to a value of 53 m<sup>2</sup>/g, while no evidences of coke formation were found, revealing that the deactivation observed was due to a slight sintering of the active phase during the reaction. A further process configuration is represented by the possibility to combine the two traditional WGS reactors (HTS and Low Temperature Shift or LTS) in one reactor operating in a medium temperature range (250-350 °C) (Medium Temperature Shift or MTS). The utilization of only one reactor operating in medium reaction conditions, leads to both economic and environmental benefits, decreasing the capital and operational costs (CAPEX and OPEX, respectively), with further advantages in the energy balance of the process.

Table 3.10 Comparison between the outlet concentrations at the thermodynamic equilibrium for HTS or MTS stream at different S/Dg values and reaction temperatures

Feed type		Outlet concentrations (molar percentages) at increasing temperatures		
HTS		350°C	400°C	450°C
<b>S/DR of clean biogas.</b> <b>S/DG: 0.55 v/v</b> <b>H<sub>2</sub>/CO: 2.06 v/v</b>	H <sub>2</sub>	66	65.3	64.6
	CO	<b>3.9</b>	<b>5.9</b>	<b>8.0</b>
	CO <sub>2</sub>	29.6	28.3	26.8
	CH <sub>4</sub>	0.5	0.5	0.5
	H <sub>2</sub> /CO	<b>16.9</b>	<b>11.1</b>	<b>8.1</b>
<b>SR of natural gas.</b> <b>S/DG: 0.55 v/v</b> <b>H<sub>2</sub>/CO: 4.46 v/v</b>	H <sub>2</sub>	78.2	78.0	77.7
	CO	<b>1.8</b>	<b>2.8</b>	<b>4.0</b>
	CO <sub>2</sub>	16.4	15.6	14.6
	CH <sub>4</sub>	3.6	3.6	3.7
	H <sub>2</sub> /CO	<b>43.4</b>	<b>27.7</b>	<b>19.3</b>
<b>MTS</b>		<b>250°C</b>	<b>350°C</b>	<b>400°C</b>
<b>S/DR of clean biogas.</b> <b>S/DG: 0.55 v/v</b> <b>H<sub>2</sub>/CO: 2.06 v/v</b>	H <sub>2</sub>	66.9	67.4	66.9
	CO	<b>1.2</b>	<b>2.2</b>	<b>3.8</b>
	CO <sub>2</sub>	31.4	29.9	28.8
	CH <sub>4</sub>	0.5	0.5	0.5
	H <sub>2</sub> /CO	<b>55.8</b>	<b>30.6</b>	<b>17.6</b>

The theoretical calculations of the outlet gas concentrations at the thermodynamic equilibrium for the MTS reaction ( $S/DG = 0.55$  v/v) showed that decreasing the reaction temperature it was theoretically possible to further improve the CO conversion and increase the  $H_2$  yield values of the plant, reaching a syngas composition like that obtained by feeding natural gas (Table 3.10).

Although the reaction was thermodynamically favoured in this temperature range, the rate of the WGS reaction decreased, making the catalyst activity of crucial importance for the process exploitation. For these reasons, the Cu-content in the catalyst was increased to a value of 20 wt.%. The catalyst used in the following tests was obtained by further addition of a small amount of Zr to a MTS catalyst with a 20 wt.% of Cu patented by our research group [19] composed by mixed oxide phases of Cu, Zn and Al, with a  $M^{2+}/M^{3+}$  molar ratio of 3, a Al/Zr molar ratio of 50 (ZAC23Zr50). As previously evidenced, the presence of a small amount of Zr enhanced the specific surface area of the catalyst, improving the dispersion of the active phase and the catalytic performances [18].

The catalytic tests were conducted in the temperature range of 250-350 °C, at a pressure of 15 bar and changing the WHSV value between 8,200 and 16,000 ml/(h·g<sub>cat</sub>). A constant S/DG ratio = 0.55 v/v was used, and the catalyst deactivation evaluated repeating the experimental conditions used in the second test ( $T = 250$  °C, WHSV = 16,000 ml/(h·g<sub>cat</sub>)) at the end of the catalytic cycle.

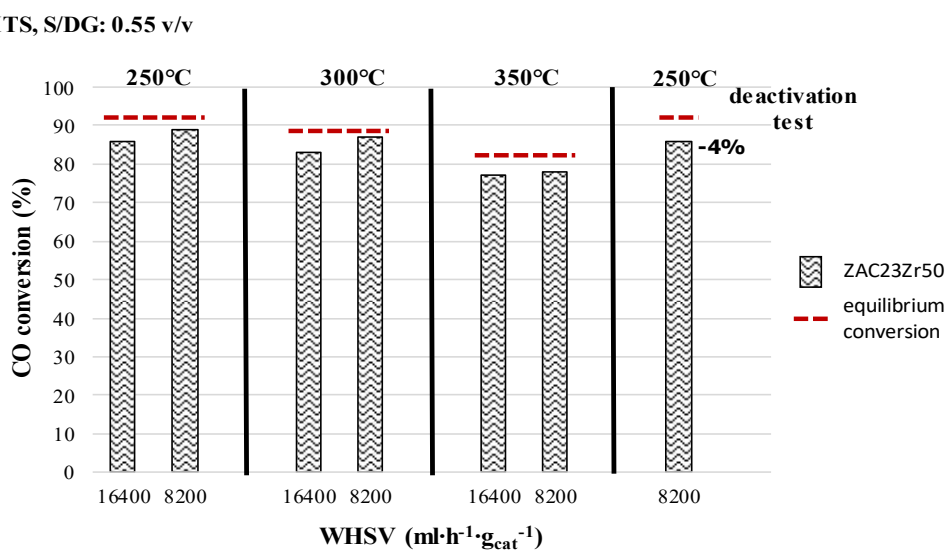
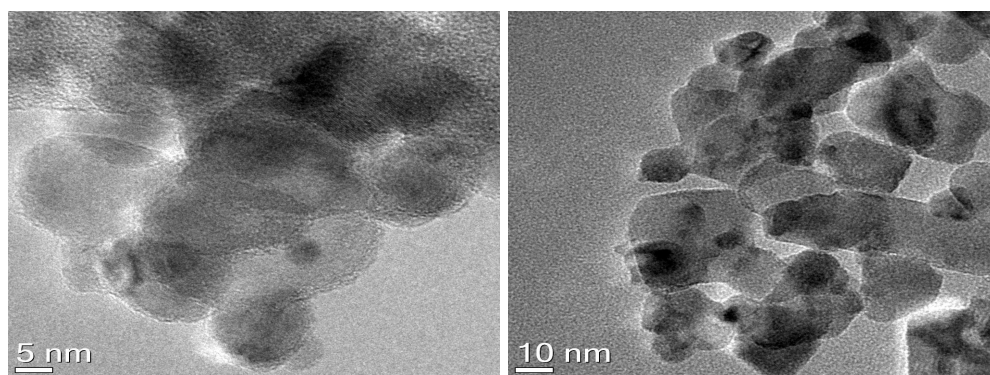


Figure 3.77. CO conversion for the ZAC23Zr50 catalyst at different temperatures as a function of the WHSV value in the MTS ( $S/DG = 0.55$ )

The ZAC23Zr50 catalyst showed excellent performances (Fig. 3.77), the mild reaction conditions improving the CO conversion values at all the temperatures tested. The best results were obtained at 250 and 300°C, in which the catalyst showed, for a WHSV value of 8,200 ml/(h·g<sub>cat</sub>), a CO conversion of about 90 %, close to the thermodynamic equilibrium value. The MTS reaction conditions together with an optimized catalyst formulation led to a small loss of catalytic activity with time-on-stream, about -4% in terms of CO conversion.

The good dispersion of the active phase on the catalyst surface was confirmed by the TEM observations on the ZAC23Zr50 spent catalyst (Fig. 3.78). The distribution of the Cu<sup>0</sup> particles was centred around an average size of 7 nm, and notwithstanding the high Cu-content (20 wt.%) in the formulation and its tendency to sinter, the formation of large agglomerates was not observed, confirming the good stability of the catalyst.



ZAC23Zr50 after reaction

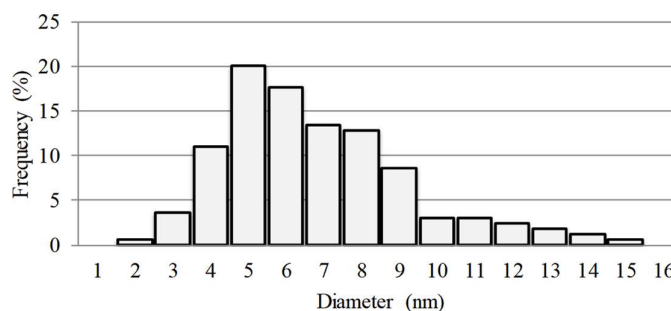


Figure 3.78. TEM images and distribution of the Cu<sup>0</sup> particles for the ZAC23Zr50 catalyst after reaction in the MTS conditions.

### 3.7.2 Preliminary conclusions.

The feasibility of the H<sub>2</sub> production from CB by the WGS reaction of the exit stream of the S/DR reactor was evaluated in three different process configurations. Carrying out the reaction on the feed such as obtained from the S/DR reactor in HTS conditions, was not possible to obtain good results in terms of CO conversion and H<sub>2</sub> productivity values due to the thermodynamic limits of the process. Moreover, the harsh reaction conditions lead to a catalyst deactivation that limits the exploitation of the process.

The addition of further amount of steam between the S/DR and the HTS reactor, increasing the S/DG ratio value to 0.55 v/v (traditionally used in the industrial process), decreased the catalyst deactivation and led to significant improvements of the results, enriching in H<sub>2</sub> the outlet syngas, although with an elevated residual CO concentration in the stream directed to the LTS reactor.

The use of one reactor that operates at medium temperature (i.e. with only one reactor) seemed to be the best configuration to obtain high H<sub>2</sub> yield in the plant. The MTS reaction conditions improved the catalyst activity and stability with time-on-stream, decreasing considerably the CO content in the outlet syngas. The compositions of the outlet streams made the produced H<sub>2</sub>-rich syngas suitable for many downstream applications either to produce chemicals or, after a CO<sub>2</sub>-removal step, for the feeding of SOFC to produce energy.

## References.

1. C. Li, P.C. Stair, *Catal. Today*, 33 (1997) 353-360
2. A. Al-Fatesh, S. K. Singh, S. G. Singh, G. S. Kanade, H. Atia, A. H. Fakeeha, A. A. Ibrahim, A. M. El-Toni, N. K. Labhasetwar, , *Int. J. Hydr. Energy*, 43 (2018) 12069-12080
3. F. Cavani, F. Trifirò, A. Vaccari, *Catal. Today*, 11 (1991) 173-302
4. Y. Zhan, J. Han, Z. Bao, B. Cao, Y. Li, J. Street, F. Yu, *Mol. Catal.*, 436 (2017) 248-258
5. V. Diez, C. Ferretti, P. Torresi, C.R. Apesteguia, J.I. Di Cosimo, *Catal. Today*, 173 (2017) 21-27
6. A. Carrero, J.A. Calles, A.J. Vizcaino, *Appl. Catal. A*, 327 (2007) 82-94
7. S.D. Angeli, G. Monteleone, A. Giaconia, A.A. Lemonidou, *Int. J. Hydrogen Energy*, 39 (2014) 1979-1997
8. P. Nash *Phase diagrams of binary nickel alloys*, ASM International, Ohio (US), 1991
9. C. Lucarelli, C. Molinari, R. Faure, G. Fornasari, D. Gary, N. Schiaroli, A. Vaccari, *Appl. Clay Sci.* 155 (2018) 103-110
10. O. Arbelàez, T.R. Reina, S. Ivanova, F. Bustamante, A.L. Villa, M.A. Centeno, J.A. Odriozola, *Appl. Catal. A*, 497 (2015) 1-9
11. T. Wu, Q. Zhang, W. Cai, P. Zhang, X. Song, Z. Sun, L. Gao, *Appl. Catal. A*, 503 (2015) 94-102
12. T. Rajkhowa, G.B. Marin, J.W. Thybaut, *J. Ind. Eng. Chem*, 54 (2017) 270-277
13. E. Vasiliadou, A. Lemonidou, *Appl. Catal.*, A, 396 (2011) 177-185
14. P. Fornasiero, R. Di Monte, G. Ranga Rao, J. Kaspar, S. Meriani, A. Trovarelli, M. Graziani, *J. Catal.*, 151 (1995) 168-177
15. A. Trovarelli, F. Zamar, J. Llorca, C. de Leitenburg, G. Dolcetti, J. Kiss, *J. Catal.*, 69 (1997) 490-502
16. P. Fornasiero, G. Balducci, R. Di Monte, J. Kaspar, V. Sergo, G. Gubitosa, A. Ferrero, M. Graziani, *J. Catal.*, 164 (1996) 173-183
17. R. Faure, G. Fornasari, D. Gary, C. Lucarelli, N. Schiaroli, A. Vaccari, *Eur. Patent 325,4760 A1* (2017)
18. "Up-grade of catalysts for medium and high temperature water gas shift reaction", Ph.D. thesis of Chiara Molinari, University of Bologna, 2017
19. F. Basile, G. Brenna, R. Faure, G. Fornasari, D. Gary, A. Vaccari, *WO 203079323*.

## 4. Conclusions

In this Ph.D. thesis the valorisation of CB through the production of syngas directly exploitable in synthesis of fuels, chemicals or hydrogen was demonstrated. The DR and S/DR processes have been deeply investigated developing novel Ni-based catalysts with highest activity and stability. The production of syngas with a H<sub>2</sub>/CO ratio around 1 by DR evidenced relevant drawbacks such as the occurrence of strong carbon deposition at low reaction temperatures and fast catalyst deactivation. By the addition of a small amount of Rh to the Ni/Mg/Al catalyst, it was possible to increase the catalyst life, its reducibility, forming active sites able to enhance the CO<sub>2</sub> conversion and limit the catalyst deactivation, especially at high temperature (900°C).

Further improvements were obtained by adding steam to the inlet feed, performing the combined S/DR reaction. In this reaction conditions, the S/CH<sub>4</sub> molar ratio of the feed was able to drive the syngas composition of the outlet stream, increasing the H<sub>2</sub>/CO molar ratio to values directly exploitable in Fischer-Tropsch or Methanol synthesis. Although the presence of steam at high temperature decreased the carbon deposition and the sintering of active phase during the reaction, for the un-promoted catalyst a significant deactivation through the Ni<sup>0</sup> re-oxidation was observed. This latter effect was overcome by doping with a small amount of Rh.

By tuning the catalytic formulation, it was possible to enhance the catalyst properties in the S/DR process. The composition of the catalytic support had a strong influence on the performances as the increase of the Mg-content improved the interaction between the active phase and the support. The formation of a NiO-MgO solid solution after calcination together with the higher basicity of the support, enhanced the CO<sub>2</sub> conversion and the catalyst stability with the time-on-stream. The formation of the Ni-Rh alloy played a key role in the improvement of the active phase dispersion and size, leading to good CB conversion values even at low temperature (800°C). These features were proportional to the Rh-content in the catalytic formulation and the extensive formation of the binary alloy suppressed the carbon deposition, avoided the sintering of the active sites and, consequently, the catalyst deactivation. The substitution of Rh with a cheaper transition metal such Cu led to the formation of the Ni-Cu alloy, however the active phase was not stable as in case of the Rh-doping, with a worsening of the catalyst properties by increasing the amount of Cu present.

A further improvement of the catalyst activity was obtained by partially changing the synthesis method of the precursor. The use of a surfactant in the co-precipitation, improved the textural and morphological properties of the final catalyst increasing the CB conversion, especially at low temperature. The large amount of meso- and macropores of the support, together with its high specific surface area, allowed to decrease the amount of Rh in the formulation and the cost associated to its exploitation.

The possibility to favour the H<sub>2</sub> production from CB by the WGS reaction on the exit stream of the S/DR process was demonstrated. Through the use of a MTS reactor and a Zr-promoted Cu/Zn/Al catalyst, a H<sub>2</sub>-rich syngas suitable for many downstream applications was obtained, proving the wide range of products that is possible to obtain by CB upgrading in a combined S/DR process. It is noteworthy, that the overall process did not lead to a real conversion of the CO<sub>2</sub> present in the CB. According to the reaction reported below:



the CO<sub>2</sub> converted in the combined S/DR process is re-obtained in the WGS unit, with just one final CO<sub>2</sub>-removal step to obtain pure H<sub>2</sub>. On the contrary, to feed biomethane, a further step of CO<sub>2</sub>-removal would be required before the SR reactor, with an increase of the operative costs.

## Acknowledgements

The biggest thanks to the Prof. Angelo Vaccari, who believed in me during these years spent working together and taught me how to be a better researcher and (most importantly) a better human being.

Thanks to Carlo, who with his friendship and help, taught me how to live every day with a bigger smile upon my face, without forgetting the seriousness of the scientific research.

Thanks to Patricia and Fabrice, who in different periods of my life guided me on the right path and taught me what to be a hard-worker means.

Thanks to Grazia, who with her great friendship showed me the light in the darkest periods.

Thanks to my parents who made me the person I am and have taught me how to fight every adversity of the journey.

Thanks to the Music, which faithfully accompanied and helped me during the writing of this thesis.

Finally, a huge thanks full of love to the Chimica Industriale & Bologna family. During these years I was lucky enough to meet extraordinary friends, whose bond I am sure will last for life. You guys have been a treasure that I will always carry with me.